NASA CR-178, 118

NASA Contractor Report 178118

NASA-CR-178118
19860019446

WAKE SHAPE AND ITS EFFECTS ON AERODYNAMIC CHARACTERISTICS

Homayoun Emdad and C. Edward Lan

THE UNIVERSITY OF KANSAS CENTER FOR RESEARCH, INC.
Lawrence, Kansas

Grant NAG1-134
July 1986

NASA
National Aeronautics and
Space Administration
Langley Research Center
Hampton, Virginia 23665

ABSTRACT

In this study, the wake shape under symmetrical flight conditions and its effects on aerodynamic characteristics are examined. In addition, the effect of wake shape in sideslip and discrete vortices such as strake or forebody vortex on lateral characteristics is presented. The present numerical method for airplane configurations, which is based on discretization of the vortex sheet into vortex segments, verified the symmetrical and asymmetrical roll-up process of the trailing vortices. Also the effect of wing wake on tail planes is calculated. It is concluded that at high lift the assumption of flat wake for longitudinal and lateral-directional characteristics should be reexamined.

N86-28918 #

TABLE OF CONTENTS

LIST OF SYMBOLS

Symbol	Description	Usual Dimension
$\vec{a}$	$= (X_1 - X)\hat{i} + (Y_1 - Y)\hat{j} + (Z_1 - Z)\hat{k}$	
$\vec{a}'$	$= (X_1 - X)\hat{i} + \beta(Y_1 - Y)\hat{j} + \beta(Z_1 - Z)\hat{k}$	
b	Wing span	m (ft)
$\vec{b}$	$= (X_2 - X)\hat{i} + (Y_2 - Y)\hat{j} + (Z_2 - Z)\hat{k}$	
$\vec{b}'$	$= (X_2 - X)\hat{i} + \beta(Y_2 - Y)\hat{j} + \beta(Z_2 - Z)\hat{k}$	
c	Local chord	m (ft)
$\bar{c}$	Mean geometric chord	m (ft)
C_{D_i}	Induced drag coefficient	non-dimensional
C_L	Lift coefficient	non-dimensional
C_ℓ	Rolling moment coefficient	non-dimensional
C_m	Pitching moment coefficient	non-dimensional
C_n	Yawing moment coefficient	non-dimensional
c_R	Root chord	in (ft)
c_s	Sectional suction coeffecient	non-dimensional
C_y	Side force coefficient	non-dimensional
C_{ℓ_β}	Variation of rolling moment coefficient with sideglip angle	rad^{-1}
C_{n_β}	Variation of yawing moment coefficient with sideslip	rad^{-1}

LIST OF SYMBOLS, continued

Symbol	Description	Usual Dimension
C_{y_β}	Variation of side force coefficient with sideslip angle	rad^{-1}
D_{ij}	Induced normal velocity at point i due to a unit vortex density at j under symmetrical conditions	non-dimensional
D'_{ij}	Induced normal velocity at point i due to a unit vortex density at j under asymmetrical conditions	non-dimensional
$\vec{\ell}$	$= (X_2 - X_1)\hat{i} + (Y_2 - Y_1)\hat{j} + (Z_2 - Z_1)\hat{k}$	
$\vec{\ell}'$	$= (X_2 - X_1)\hat{i} + \beta(Y_2 - Y_1)\hat{j} + \beta(Z_2 - Z_1)\hat{k}$	
L	Number of segments into which a trailing vortex is divided	
M	Number of trailing vortex elements	
M_∞	Free-stream Mach number	non-dimensional
N	Number of bound vortex elements in a strip	
p	Perturbed roll rate	rad/sec
$\bar{p}$	$= pb/2U_\infty$	non-dimensional
$\bar{q}$	Dynamic pressure	N/m^2 (lbs/ft^2)
r	Perturbed yaw rate	rad/sec
$\bar{r}$	$= rb/2U_\infty$	
$\vec{R}$	$= X\hat{i} + Y\hat{j} + Z\hat{k}$	
$\vec{R}_1$	$= X'\hat{i} + Y'\hat{j} + Z'\hat{k}$	

LIST OF SYMBOLS, continued

Symbol	Description	Usual Dimension
S	Reference wing area	m^2 (ft^2)
$s_{\ell e}$	Length of the leading edge	m (ft)
u, v, w	Velocity components	m/sec (ft/sec)
U_∞	Free-stream velocity	m/sec (ft/sec)
$\vec{V}$	Induced velocity vector due to a vortex distribution	m/sec (ft/sec)
X, Y, Z	Wing rectangular coordinate system with X in the streamwise direction and Y to the right	m (ft)
X', Y', Z'	(X, Y, Z) coordinates of a point on a vortex element	m (ft)
Y_s	Y coordinates of edges of a wing spanwise section	m (ft)
Z_c	Camber ordinate	m (ft)
Greek Symbol		
α	Angle of attack	rad
$\beta = \sqrt{1 - M_\infty^2}$	Prandtl-Glauert transformation factor, or sideslip angle	
γ	Vortex density referred to free-stream velocity	non-dimensional
Γ	Concentrated vortex strength based on free-stream velocity	m (ft)
Γ_t	Total circulation of a strake vortex referred to free-stream velocity	m (ft)

LIST OF SYMBOLS, continued

Symbol	Description	Usual Dimension
$\bar{\Gamma}_t$	Circulation of a strake vortex per unit length of the leading edge referred to free-stream velocity	non-dimensional
Λ	Sweep angle of leading edge	rad
ϕ	Dihedral angle	degree
ρ	Fluid density	kg/m^3 (slug/ft^3)

Subscript	
1	The first end point of a vortex element or a wing section
2	The second end point of a vortex element or a wing section
c	Control point on lifting surfaces
CP	Control point on the wake vortex sheet
ℓe	Leading-edge
te	Trailing-edge

1. INTRODUCTION

In the past, considerable interest has been shown in computational methods of analyzing the roll-up characteristics of aircraft trailing vortices and their effect on tail surfaces. Although the general viscous flow problem is quite complicated and requires further research, it is possible to calculate the main effect of wake roll-up by a potential flow model. Considerable progress has been made in the latter.

The occurrence of a vortex sheet which trails from a finite aspect-ratio wing is a consequence of the nonuniform lift distribution on the wing sections. The roll-up of this sheet into discrete vortices, as a result of a convective motion, was recognized by Lanchester in 1907 (Reference 1).

Westwater (1935) modeled the continuous vortex sheet (assumed two-dimensional) trailing from a wing with an elliptical load distribution by discrete vortices, and computed the time development of the configuration by use of a complex potential. He assumed that the sheet extended to infinity upstream and downstream of the wing; and the effect of the wing itself was ignored. That is, no attempt was made to incorporate the effect of the solid body in the flow. This assumption is sufficiently valid if the spatial development of the sheet is slow enough for a quasi-two-dimensional situation to hold at any downstream location (Reference 2).

This two-dimensional time-dependent model of Westwater was further investigated by many others with the purpose of improving the numerical stability in the calculation. For example, Moore (1971) used a point vortex representation to study numerically the evolution of an initially plane vortex sheet by using a very accurate time integration procedure and two to four times the number of point vortices used by Westwater for vortex sheet representation. He found that the paths of vortices near the edges of the sheet were extremely contorted. This motion is convincingly shown to be due to propensity of close line vortices to rotate about each other (Reference 3).

Clement and Maull (1973) used a method similar to that used by Westwater to represent the rolling up of a trailing vortex sheet (Reference 4). The investigation was oriented towards determining the effect of span loading distribution on the roll-up characteristics of trailing vortices.

Hancock (1970) questioned the validity of applying these two-dimensional results to finite wings when the lift coefficient is large because of the significant effects of wing circulation (Reference 5). To improve the two-dimensional model, Butter and Hancock (Reference 6) replaced the wing by a single lifting-line bound vortex which represented the circulation distribution around the wing. The trailing vortex sheet was approximated by a number of discrete line vortices, and the downwash and sidewash velocities were calculated at midpoint of each vortex element. The induced velocity of each vortex element on itself was ignored because the self-induced velocity at any point is infinite. A similar approach was also employed by Hackett and Evans for high-lift wings (Reference 7).

In all these investigations, the wing circulation distribution was assumed unchanged during the wake roll-up process. In other words, the interaction between the wing loading and the wake roll-up was not accounted for. The latter can be important for a configuration with a canard, or an aft tail, or both, under high lift conditions. Numerical methods to determine these interaction effects are available and have been applied in the past mostly to calculating longitudinal loading on slender wings with edge-separated vortex flow (see, for example, References 8 and 9). The solution was calculated in an iterative manner by satisfying the flow tangency condition on the wing surface and the force-free condition on the free vortex sheets.

In the present three-dimensional study, in addition to longitudinal characteristics, the effect of wake shape in sideslip and discrete vortices (such as strake or forebody vortex) on lateral characteristics will be investigated. The computational method is similar to that of Reference 9 in that a lifting-surface method is used to represent the wing, not just a lifting line.

The wing boundary conditions are formulated by the Quasi-Vortex Lattice Method (QVLM) of Lan (Reference 10).

The trailing vortices in the wake region are represented by discrete free vortex segments which are aligned with the local velocity vector at their midpoint to satisfy the force-free condition as described in detail in Section 2.5.2. The flow tangency condition is satisfied on the wing including the trailing edge. Due to the nonlinear nature of interaction between the wake shape and wing loading, the problem is solved in an iterative manner.

Chapter 2 presents the theoretical method. In Chapter 3, numerical results are presented and discussed. Conclusions are made in Chapter 4.

2. THEORETICAL METHOD

2.1 PROBLEM DESCRIPTION

For a wing with a positive lift, the sectional loading decreases to zero toward the wing tips, producing a circulation variation around the wing. This circulation variation causes an inward deflection of the streamlines above the wing and an outward deflection below the wing. Then the streamlines that converge behind the wing are in different directions and form a surface of vorticity. This surface of vorticity tends to roll up farther downstream, forming two distinct vortices of opposite direction. The wing can be represented by a horseshoe vortex distribution which consists of bound vortices and trailing vortices to create pressure differences used to model wing aerodynamic characteristics. The wake region is modeled by force-free vortex sheets (continuations of wing trailing vortices), across which there is no pressure difference. In the present method, the code based on the QVLM (Reference 11) that incorporates the wing, fuselage, canard, and tail surfaces is modified to determine the wake shape in longitudinal and lateral directions and its effects on tail planes. It can also determine the effect of canard wake on wing and tail planes.

The following boundary conditions are imposed on the flow model:

a) The flow must be tangent to the wing camber surface.

b) The trailing-edge Kutta condition is to be satisfied.

c) The vortex segments in the wake region are force free.

In general this nonlinear problem has three sets of unknowns:

a) strength of the wing horseshoe vortices,

b) strength of the free vortices in the wake,

c) the location of wake vortices.

For simplicity and saving in computing time, the following assumptions are made;

a) The wake vortex strength is assumed equal to wing trailing vortex strength. Decay in vortex strength is not considered.

b) The vorticity organizes itself into two or more centers of vorticities behind the airplane. This initial roll-up of the trailed vorticities behind an airplane is a relatively rapid process and generally complete within a distance equal to several spans of the wing. For this reason and for practical purposes, the part played by viscosity in this initial organization is assumed small and the roll-up process may, to the first order of accuracy, be computed as an inviscid process (Reference 1).

2.2 GEOMETRY OF WING AND VORTEX WAKE SYSTEM

In the Quasi-Vortex Lattice Method (Reference 10), for the purpose of satisfying wing boundary condition, the continuous vortex distribution over the wing is replaced by a quasi-continuous one, being continuous chordwise but stepwise constant in the spanwise direction. Thus, the wing surface can be divided into a number of vortex strips with the associated trailing vortices (Figure 1). The chordwise location of bound elements is given by the cosine law and is illustrated in Figure 1 (Reference 10).

$$X_k = X_{\ell e} + \frac{c}{2}\left(1 - \cos[(2k - 1)\pi/2N]\right) \qquad (1)$$

$k = 1,2,\ldots,N$

where

$X_{\ell e}$: leading-edge X-coordinate

c : chord length

N : number of bound elements in a chordwise direction.

A wing may be divided into a number of spanwise sections. In each section, the spanwise locations of trailing elements are given by the following relation (Reference 10):

$$Y_j = Y_{s1} + \frac{Y_{s2} - Y_{s1}}{2}\left[1 - \cos\left(\frac{2j - 1}{2M}\right)\pi\right] \qquad (2)$$

$j = 1,2,\ldots,M$

where

M : number of legs of trailing vorticity, which is one larger than the number of spanwise strips of bound elements

Y_{s1}: Y coordinate of the inboard edge of a spanwise section

Y_{s2}: Y coordinate of the outboard edge of a spanwise section

The location of control points where the flow tangency condition is satisfied is also based on the cosine law, as illustrated in Figure 1. The control point locations are as follows:

$$X_{c_i} = X_{\ell e_j} + \frac{c_j}{2} \left(1 - \cos \frac{i\pi}{N}\right) \tag{3}$$

$$i = 1,\ldots,N$$

$$Y_{c_j} = Y_{s1} + \frac{Y_{s2} - Y_{s1}}{2} \left(1 - \cos\left(\frac{j\pi}{M}\right)\right) \tag{4}$$

$$j = 1,2,\ldots(M - 1)$$

where

$X_{\ell e_j}$: leading-edge X coordinate at Y_{c_j}
c_j : chord length at Y_{c_j}

The wake vortex system is made up of wing trailing vortices. Each trailed vortex from the trailing edge of the wing is divided into a number of segments up to two span lengths behind the wing (Figure 2) to form the initial location of the wake vortex system. Each segment is assumed to have a length equal to

$$\Delta X = .25c_R \tag{5}$$

These segments have the following characteristics:

a) All segments have equal lengths.

b) The length of each segment is preserved throughout the iteration process.

c) In the final converged position these segments are aligned in the direction of the local velocity vector.

The initial location of wake vortex segments are

$$X_i = X_{te} + i\Delta X \tag{6}$$

$$i = 1, \ldots, L$$

$$Y_i = Y_{te} \tag{7}$$

$$Z_i = Z_{te} \tag{8}$$

where

L: number of segments in each element.

2.3 INDUCED VELOCITY DUE TO WING

As described in Section 2.2, the wing surface is covered with a number of vortex strips with the associated trailing vortices. In any strip, consider a vortex element of γdX with a direction $\vec{\ell}$. The induced velocity due to all bound elements in the i^{th} strip at $\vec{R} = (X, Y, Z)$ is given by (see Appendix A)

$$\vec{V}_{i_1}(\vec{R}) = \frac{\beta^2}{4\pi} \int_{X_{\ell e}}^{X_{te}} \gamma(X')\left(\frac{\vec{a} \times \vec{\ell}}{|\vec{a}' \times \vec{\ell}'|^2} \left\{\frac{\vec{b}'}{|b'|} - \frac{\vec{a}'}{|a'|}\right\} \cdot \vec{\ell}'\right)dX' \tag{9}$$

and due to the associated trailing vortices by (Reference 10),

$$\vec{V}_{i_2}(\vec{R}) = \frac{\beta^2}{4\pi} \int_{X_{\ell e}}^{X_{te}} \gamma(X')\left(\int_{X'}^{\infty} \frac{(\vec{R}_1 - \vec{R}) \times d\vec{\ell}}{R^3_\beta}\right)dX' \tag{10}$$

where symbols $\vec{a}$, $\vec{b}$, etc., are position vectors of a vortex element relative to a field point, $\vec{R} = (X, Y, Z)$, and are defined in the list of Symbols and Appendix A.

If the integration variable X' in Equations (9) and (10) is replaced by θ, where $X' = X_{\ell e} + \frac{c(Y)}{2}(1 - \cos\theta)$, then Equations (9) and (10) can be reduced to

$$\vec{V}_{i_1}(\vec{R}) = \frac{\beta^2 c(Y)}{8\pi} \int_0^\pi \vec{G}_1(\theta)\gamma(\theta)\sin\theta d\theta \tag{11}$$

and

$$\vec{V}_{i_2}(\vec{R}) = \frac{\beta^2 c(Y)}{8\pi} \int_0^\pi \vec{G}_2(\theta)\gamma(\theta)\sin\theta d\theta \tag{12}$$

where

$$\vec{G}_1(\theta) = \frac{\vec{a} \times \vec{\ell}}{|\vec{a}' \times \vec{\ell}'|^2} \{\frac{\vec{b}'}{|\vec{b}'|} - \frac{\vec{a}'}{|\vec{a}'|}\} \cdot \vec{\ell}' \tag{13}$$

$$\vec{G}_2(\theta) = \int_{X'}^{\infty} \frac{(\vec{R}_1 - \vec{R}) \times d\vec{\ell}}{R^3{}_\beta} \tag{14}$$

$$c(Y) = X_{te} - X_{\ell e} \tag{15}$$

$$\gamma(\theta) = \gamma(X')$$

Let $\vec{G}'_2$ and $\vec{G}''_2$ be $\vec{G}_2$ for the left and right trailing vortices of a bound element, respectively. The total induced velocity due to the i^{th} strip of vortex distribution is then given by

$$\vec{V}_i(\vec{R}) = \frac{\beta^2 c(Y)}{8\pi} \int_0^\pi \vec{G}_1(\theta)\gamma(\theta)\sin\theta d\theta +$$

$$\frac{\beta^2 c(Y)}{8\pi} \int_0^\pi \vec{G}'_2(\theta)\gamma(\theta)\sin\theta d\theta +$$

$$\frac{\beta^2 c(Y)}{8\pi} \int_0^\pi \vec{G}''_2(\theta)\gamma(\theta)\sin\theta d\theta \tag{16}$$

where the first term is due to bound elements, the second due to the left leg of trailing vortices, and the third due to the right leg of trailing vortices. The above integrals are reduced to finite sums through the midpoint trapezoidal rule (Reference 10),

$$\vec{V}_i(\vec{R}) = \frac{\beta^2 c(Y)}{8N} \sum_{k=1}^{N} (\vec{G}_{1_k} + \vec{G}'_{2_k} + \vec{G}''_{2_k})\gamma_k \sin\theta_k \tag{17}$$

Note that the integration for $\vec{G}_2$ (Equation 14) can be directly performed. However, it can also be derived by using Equation (13). This is indicated in Equation (A.4) of Appendix A.

2.4 INDUCED VELOCITY DUE TO WAKE VORTEX SYSTEM

The wake vortex system, as described in Section 2.2, consists of M vortex elements, each of which is divided into a number of smaller vortex segments. Assume that the n^{th} element has L small segments. The induced velocity at a point (X, Y, Z), due to the m^{th} segment of the n^{th} element is given by (see Appendix A)

$$\vec{V}_{n_m}(\vec{R}) = \frac{\beta^2 \Gamma_n}{4\pi} \frac{\vec{a} \times \vec{\ell}}{|\vec{a}' \times \vec{\ell}'|^2} \left\{\frac{\vec{b}'}{|\vec{b}'|} - \frac{\vec{a}'}{|\vec{a}'|}\right\} \cdot \vec{\ell}' \tag{18}$$

where

$$\vec{R} = X\hat{i} + Y\hat{j} + Z\hat{k} \tag{19a}$$

$$\vec{a} = (X_m - X)\hat{i} + (Y_m - Y)\hat{j} + (Z_m - Z)\hat{k} \tag{19b}$$

$$\vec{b} = (X_{m+1} - X)\hat{i} + (Y_{m+1} - Y)\hat{j} + (Z_{m+1} - Z)\hat{k} \tag{19c}$$

$$\vec{\ell} = (X_{m+1} - X_m)\hat{i} + (Y_{m+1} - Y_m)\hat{j} + (Z_{m+1} - Z_m)\hat{k} \tag{19d}$$

$$\vec{a}' = (X_m - X)\hat{i} + \beta(Y_m - Y)\hat{j} + \beta(Z_m - Z)\hat{k} \tag{19e}$$

$$\vec{b}' = (X_{m+1} - X)\hat{i} + \beta(Y_{m+1} - Y)\hat{j} + \beta(Z_{m+1} - Z)\hat{k} \tag{19f}$$

$$\vec{\ell}' = (X_{m+1} - X_m)\hat{i} + \beta(Y_{m+1} - Y_m)\hat{j} + \beta(Z_{m+1} - Z_m)\hat{k} \tag{19g}$$

Γ_n: vortex strength of the n^{th} element.

The subscripts m and m+1 correspond to the end points of the m^{th} vortex segment.

Now, the induced velocity due to the n^{th} element can be written as

$$\vec{V}_n(\vec{R}) = \sum_{m=1}^{L} \vec{V}_{n_m}(\vec{R}) \tag{20}$$

Therefore, the induced velocity due to all elements is

$$\vec{V}(\vec{R}) = \sum_{n=1}^{M} \vec{V}_n(\vec{R}) \tag{21}$$

2.5 BOUNDARY CONDITIONS

As mentioned before, the boundary conditions that are imposed on the flow are

a) The flow must be tangential to the wing camber surface.

b) The trailing-edge Kutta condition is to be satisfied.

c) The vortex elements in the wake behind the trailing edge must be force free.

2.5.1 Formulation of Wing Boundary Condition

The bound elements and the corresponding control points of the wing surface are numbered from the leading edge to the trailing edge and from root to tip. Thus there are K = N(M - 1) bound elements and corresponding control points. The flow tangency condition can be written as (References 12 and 13)

$$[D_{ij}]\{\gamma_j\} = \{\cos\phi \frac{dZ_c}{dX} \cos\alpha - \cos\phi\sin\alpha\} \qquad (22)$$

$$[D'_{ij}]\{\gamma'_j\} = \{\beta\sin\phi + \bar{p}(\frac{Z}{b/2} \sin\phi + \frac{Y}{b/2} \cos\phi) - \bar{r} \sin\phi(\frac{X}{b/2})\} \qquad (23)$$

where

D_{ij} is the induced normal velocity under symmetrical flight conditions at the i^{th} control point of wing due to a unit horseshoe vortex density at j

γ_j is the vortex density of the j^{th} bound element

$\frac{dZ_c}{dX}$ is the camber slope of the i^{th} control point

ϕ is the dihedral angle

D'_{ij} is the induced normal velocity under antisymmetrical conditions at the i^{th} control point of wing due to a unit horseshoe vortex density at j

γ'_j is the vortex density of the j^{th} bound element under antisymmetrical conditions

β is the sideslip angle

$\bar{P} = \frac{Pb}{2U_\infty}$

$\bar{r} = \frac{rb}{2U_\infty}$

The right hand side of the first equation is the boundary condition for symmetrical loading at a given angle of attack.

2.5.2 Formulation of Vortex Force-Free Condition

Control points in the wake are chosen at midpoints of vortex strips (Figure 2). To satisfy the force-free condition, the vortex segment should be aligned in the direction of local velocity vector calculated at the control point. For this condition to be satisfied, a linear interpolation is used to find the induced velocity component at the midpoint of each vortex segment.

Consider the n^{th} and $(n + 1)^{th}$ vortex elements and their m^{th} vortex segments. The end point coordinates of the m^{th} vortex segments are given by $(X_{n,m}, Y_{n,m}, Z_{n,m})$, $(X_{n,m+1}, Y_{n,m+1}, Z_{n,m+1})$ and $(X_{n+1,m}, Y_{n+1,m}, Z_{n+1,m})$, $(X_{n+1,m+1}, Y_{n+1,m+1}, Z_{n+1,m+1})$. The control point locations are then

$$X_{CP} = \frac{1}{2}\left[\frac{(X_{n,m} + X_{n,m+1})}{2} + \frac{(X_{n+1,m} + X_{n+1,m+1})}{2}\right]$$

$$Y_{CP} = \frac{1}{2}\left[\frac{(Y_{n,m} + Y_{n,m+1})}{2} + \frac{(Y_{n+1,m} + Y_{n+1,m+1})}{2}\right] \qquad (24)$$

$$Z_{CP} = \frac{1}{2}\left[\frac{(Z_{n,m} + Z_{n,m+1})}{2} + \frac{(Z_{n+1,m} + Z_{n+1,m+1})}{2}\right]$$

Assume the velocity at the control point of a segment at a given iterative step is given by

$$\vec{V} = (u\hat{i} + v\hat{j} + w\hat{k}) \qquad (25)$$

where

$u = U_\infty \cos\alpha + u_1$

$v = v_1$, for symmetrical flight condition

$v = v_1 + U_\infty \sin\beta$, in sideslip

$w = U_\infty \sin\alpha + w_1$

u_1 is the induced backwash velocity

v_1 is the induced sidewash velocity

w_1 is the induced downwash velocity

U_∞ is the free-stream velocity.

Then, the new location of the (m + 1)th end point will be

$$X_{n,m+1} = X_{n,m} + \frac{u}{V}\Delta S \qquad (26a)$$

$$Y_{n,m+1} = Y_{n,m} + \frac{v}{V}\Delta S \qquad (26b)$$

$$Z_{n,m+1} = Z_{n,m} + \frac{w}{V} \Delta S \tag{26c}$$

where

$$V = \sqrt{u^2 + v^2 + w^2} \tag{27}$$

$$\Delta S = \sqrt{(X_{n,m+1} - X_{n,m})^2 + (Y_{n,m+1} - Y_{n,m})^2 + (Z_{n,m+1} - Z_{n,m})^2} \tag{28}$$

Before Equations (26) are used, it should be noted that the length of each segment is to be preserved. For numerical stability, Equations (26) will be modified as follows by including a relaxation parameter.

Consider the same m^{th} segment. If this segment moves "a" percent (of the initial location) only according to the velocity computed at its control point, then Equations (26) can be modified to be

$$\begin{aligned} \Delta Y &= \frac{av}{V} \Delta S + (1 - a)(Y_{n,m+1} - Y_{n,m}) \\ \Delta Z &= \frac{aw}{V} \Delta S + (1 - a)(Z_{n,m+1} - Z_{n,m}) \\ \Delta X &= \sqrt{\Delta S^2 - \Delta Y^2 - \Delta Z^2} \end{aligned} \tag{29}$$

where "a" represents a relaxation parameter.

It follows that

$$X_{n,m+1} = X_{n,m} + \Delta X \tag{30a}$$

$$Y_{n,m+1} = Y_{n,m} + \Delta Y \tag{30b}$$

$$Z_{n,m+1} = Z_{n,m} + \Delta Z \tag{30c}$$

2.6 SOLUTION PROCEDURES

The basic sets of unknowns of the problem are the bound vortex density of the wing, and the location of wake vortex elements. The problem is nonlinear because the locations of the vortex system are unknown a priori. Therefore, the problem will be solved by an iterative process described below.

i) The vortex lattice for the wing surface and the initial location for the wake elements are first prescribed.

ii) By satisfying the wing boundary conditions, the bound vortex density of the wing is obtained.

iii) The free elements of the wake vortex system are adjusted to be in the local velocity direction as described in Section 2.5.2.

iv) Steps (ii) through (iii) are repeated until a converged solution is obtained.

After the longitudinal wake shape is obtained, the flow is then perturbed by a sideslip angle if lateral characteristics are needed.

The following procedure is used to find the new asymmetric wake shape and aerodynamic forces and moments.

a) Initially, calculate γ_β (vortex density in sideslip) due to $\beta\sin\phi$ using the symmetrical wake shape.

b) Sum the antisymmetrical and symmetrical vortex densities to find a new wake shape under the β perturbation through the iterative process.

c) Calculate the new downwash on the wing with the new asymmetrical wake shape.

d) Subtract the downwash calculated on the wing, with the sum of antisymmetrical and symmetrical vortex densities from the downwash of symmetrical vortex density to get the influence of the new wake.

e) Add step (d) to $\beta \sin\phi$ to find new boundary conditions.

f) With the new boundary conditions, calculate new vortex density.

g) Calculate all aerodynamic forces and moments.

The initial locations of the free vortex elements are assumed to be in the wing plane. In the iteration process, the force-free condition is satisfied on the free elements from the root to tip in a row and row by row in the downstream direction. A similar approach with different control point locations was used by Butter and Hancock (Reference 6) with success.

2.7 DISCRETE FOREBODY AND STRAKE VORTICES

Experiments show that for slender bodies and lifting surfaces the flow always separates from the surface and rolls up into spiral vortex sheets. The effect of this separated-flow or vortex-flow phenomenon is quite important at subsonic speed because of its large contribution to the total aerodynamic characteristics.

The leading-edge and side-edge vortex systems induce additional velocities at the wing upper surface and produce an additional lift force which depends nonlinearly on the angle of attack.

In addition, when the leading-edge vortex system passes over an area downstream of the leading-edge tip, additional vortex lift is developed. This component of lift has been called the augmented vortex lift. Also for a straked wing, the strake vortex not only produces the augmented vortex lift but also induces downwash inboard and upwash outboard of the strake-wing juncture. To account for this effect, a discrete vortex starting from the juncture to downstream infinity is introduced. The strength of this vortex is calculated by equating the vortex lift to the Kutta-Joukowski force (Reference 11):

$$\frac{1}{2}\,\rho U_\infty{}^2 c_S c\,dY = \rho \Gamma w_{\ell e}\,d\ell \tag{31}$$

where

c_S is the sectional leading-edge suction coefficient

Γ is the equivalent circulation per unit length of the leading edge

$w_{\ell e}$ is the upwash at the leading edge

$d\ell$ is the length measured along the leading edge.

The total circulation, Γ_t, of vortex strength is given as follows (Reference 11)

$$\Gamma_t = \int_{\ell e} \frac{\Gamma}{U_\infty}\,d\ell = \frac{1}{2}\int_{\ell e} \frac{c_S c}{w/U_\infty\big|_{\ell e}}\,\frac{dY}{d\ell}\,d\ell \tag{32}$$

where the integration is performed along the leading edge and w is evaluated at the leading edge.

The average vortex strength, $\bar{\Gamma}_t$, per unit length of the leading edge is therefore

$$\bar{\Gamma}_t = \frac{\Gamma_t}{s_{\ell e}} \tag{33}$$

where $s_{\ell e}$ is the length of leading edge on which the vortex is produced.

Note that

a) $$\frac{1}{2}\int_a^b \frac{c_S c}{w/U_\infty|_{\ell e}}\, dY = \frac{1}{2}\left[\frac{1}{2}(b - a)\int_0^\pi \frac{c_S c}{w/U_\infty|_{\ell e}} \sin\phi d\phi\right]$$

$$\simeq \frac{1}{4}(b - a)\frac{\pi}{M}\sum_{i=1}^{M} \frac{c_S c}{w/U_\infty|_{\ell e}} \sin\phi_i \tag{34}$$

b) Since both c_S and $w_{\ell e}$ depend on $\bar{\Gamma}_t$, the circulation is determined iteratively.

A similar approach to that in Section 2.5.2 is used to find the position of the discrete vortex element from the wing junction to distance of two spans behind the wing trailing edge. Also the position of discrete vortex element for small sideslip perturbation can be calculated.

The main objective of finding the location of discrete vortex elements is to determine the location of this vortex relative to the vertical tail, and to determine its effect on directional stability. Additional discussion will be given in the next chapter.

3. NUMERICAL RESULTS AND DISCUSSIONS

The present numerical method, which is based on discretization of the vortex sheet into vortex segments, is used to verify the roll-up process of the trailing vortices. Also for any surface with a kinked leading edge, the trailing vortices from the kinked location is calculated and demonstrated clearly.

The following points should be considered in applications of the method:

a) The accuracy of the method for determining longitudinal and lateral-directional derivatives and wake shape in sideslip depends somewhat on the length of each free vortex segment and the number of trailing vortices. If the length of free vortex segment decreases, the method tends to be more accurate; but the computing time will be increased.

b) The complete trailing vortex system is calculated by the step-by-step process described in Chapter 2. Generally the roll-up is completed between the fifth and tenth iterations.

The longitudinal wake shape by the present method is compared with the numerical solution of Bloom and Jen, where they applied the artificial viscosity method of Kuwahara and Takami to a rectangular wing with aspect ratio of eight and the lift coefficient equal to one ($C_L = 1$; Reference 14). The results of the present method were calculated by using 15 spanwise vortex strips and each trailing element divided into twenty segments. The length of each free vortex segment was 25 percent of the root chord. It took approximately 10 iterations for the complete roll-up process. The predicted wake shape is plotted in Figure 3, which shows a good agreement between the two methods.

The longitudinal roll-up process of trailing vortices of a twin-jet fighter airplane, at two different angles of attack, from the wing trailing edge up to two spans behind the trailing edge, is calculated. The fuselage is represented by a body of revolution, and nacelles are not modeled. The results indicate that at low angles of attack, the roll-up process is slow because of small loading as well as weak interaction among trailing vortices (Figure 4). At high angles of attack, the loading is increased and the roll-up process is much faster as is shown in Figure 5. For $\alpha = 20$ degrees, the roll-up is completed within two spans behind the trailing edge. The rapid change in wake shape at $Y/(b/2) \approx 0.35$ in Figure 5(g) is due to change of dihedral angle in the tip section and discontinuity in the wing leading edge. This point will move inboard as the roll-up process is completed.

The aerodynamic characteristics of the twin-jet fighter airplane configuration are compared with the experimental data of Reference 15 and QVLM (Reference 11; inviscid, flat wake assumption, and with vortex breakdown) in Figure 6. The results are in good agreement up to an angle of attack of about 15 degrees. The disagreement with experimental data above 15 degrees is perhaps due to viscous effects.

The predicted longitudinal aerodynamic characteristics of tail plane by the present method is compared with the QVLM results in Figure 7. The results show some disagreement at high angles of attack. This is because, with roll-up, the wake tends to move away from the low tail at high angles of attack so that the induced downwash is reduced.

The effect of wake in sideslip for the twin-jet fighter airplane is calculated and the results are shown in Figure 8. It is seen that the wake is not symmetrical any more and moves in the direction of sideslip.

The predicted lateral-directional characteristics of the twin-jet airplane in sideslip are compared with the QVLM results (inviscid, flat wake, and with vortex breakdown) and experimental data of Reference 16 in Figure 9. The present method shows a small deviation from the QVLM results, which is due to the effect of wake roll-up on the vertical tail.

The longitudinal and lateral wake shape of a straked-wing configuration in sideslip is determined and the results are given in Figures 10-11. It appears that the strake vortex tends to move outboard and stay close to the tip vortex as it moves downstream.

The predicted longitudinal and lateral-directional aerodynamic characteristics of a straked-wing configuration in sideslip are compared with the QVLM results (inviscid, flat wake, and without vortex breakdown) and experimental data of Reference 17 in Figures 12-14. Significant changes in longitudinal aerodynamic characteristics due to tail plane and lateral-directional stability derivatives are observed as follows:

a) The longitudinal vortex wake of the straked-wing configuration is rolled up within a distance of less than one span behind the trailing edge. The presence of the strake vortex introduces some effect on the downwash field at the horizontal tail. For this reason, some changes in aerodynamic characteristics of the tail plane calculated by the present method relative to the QVLM results (inviscid, flat wake, and without vortex breakdown) are observed (Figure 12). The C_L and C_{D_i} results from QVLM and the present method for the complete configuration, show good agreement with experimental data (without horizontal tail) of Reference 17 at low angles of attack. At high angles of attack, because of inviscid assumption, the above methods failed to predict the aerodynamic characteristics accurately (Figure 13(a)). Due to change of downwash field of the tail plane by the roll-up wake, the predicted pitching moment coefficient (C_m) by the present method is slightly better than the QVLM prediction (inviscid, flat wake assumption, and without vortex breakdown) as shown in Figure 13(b).

b) The predicted C_m is more negative than the data show. The calculated results indicate that this is mostly due to the contribution of augmented vortex lift. Since the latter is assumed to be uniformly distributed along the wing-strake junction, further research on its distribution is needed to improve the modeling.

c) Due to the presence of asymmetrical vortex wake roll-up of straked wing in sideslip, the flow pattern around the vertical tail changes and introduces a side force which causes significant changes in directional stability derivative (C_{n_β}) and also C_{Y_β} derivative of the airplane. Therefore for airplanes with high wing loadings, the assumption of flat wake in calculating the lateral-directional derivatives should be reexamined (Figure 14).

Figures 15 and 16 show the position of discrete strake vortices for the straked-wing configuration at the vertical tail location. No numerical or experimental data are available for comparison.

4. CONCLUSIONS

A theoretical method has been developed for predicting the wake shapes in symmetrical flight conditions and with sideslip, including their effect on tail planes. The present method has been shown to work satisfactorily for most configurations without encountering any numerical instability in the solution. The results indicate that for a wing with high lift, the assumption of flat wake is inaccurate; and the effect of vortex wake roll-up on longitudinal and lateral-directional aerodynamic characteristics of airplanes needs to be examined. Note that in the present method the effect of fuselage vortex wake roll-up was not accounted for.

5. REFERENCES

1. Coleman, Donaldson; and Bilanin, Alan J.: Vortex Wakes of Conventional Aircraft. AGARDograph No. 204, May 1975.
2. Clements, R. R.: Flow Representation, Including Separated Regions, Using Discrete Vortices. AGARD-LS-86, 1977.
3. Moore, D. W.: The Discrete Vortex Approximation of a Finite Vortex Sheet. Cal. Inst. Tech. Rep., AFOSR-1804-69, 1971.
4. Clements, R. R.; and Maull, D. J.: The Rolling-Up of a Trailing Vortex Sheet. Aero. J. Royal Aero. Soc., 77, 46, 1973.
5. Hancock, G. J.: On the Rolling-Up of a Trailing Vortex Sheet. The Aeronautical Journal, Vol. 74, No. 717, pp. 749-752, September 1970.
6. Butter, D. J.; and Hancock, G. J.: A Numerical Method for Calculating the Trailing Vortex System behind a Swept Wing at Low Speed. Aero. J. Royal Aero. Soc., 75, 584, 1971.
7. Hackett, J. E.; and Evans, M. R.: Vortex Wakes Behind High-Lift Wings. Journal of Aircraft, Vol. 8, May 1971, p. 334.
8. Mook, D. T.; and Maddox, S. A.: Extension of a Vortex-Lattice Method to Include the Effect of Leading-Edge Separation. Journal of Aircraft, Vol. 11, pp. 127-128, Feb. 1974.
9. Mehrotra, Sudhir C.; and Lan, C. E.: A Theoretical Investigation of the Aerodynamics of Low-Aspect-Ratio Wings with Partial Leading-Edge Separation. NASA CR 145304, Jan. 1978.

10. Lan, C. E.: A Quasi-Vortex-Lattice Method in Thin Wing Theory. Journal of Aircraft, Vol. 11, No. 9, pp. 518-527, Sept. 1974.

11. Lan, C. E.: VORSTAB: A Computer Program for Calculating Lateral-Directional Stability Derivatives with Vortex Flow Effect. NASA CR 172501, Jan. 1985.

12. Lan, C. E.; and Chang, J. F.: Calculation of Vortex Lift Effect for Cambered Wings by the Suction Analogy, NASA CR-3449, July 1981.

13. Lan, C. E.; and Hsu, C. H.: Effects of Vortex Breakdown on Longitudinal and Lateral-Directional Aerodynamics of Slender Wings, AIAA Paper 82-1385, August 1982.

14. Bloom, A. M.; and Jen, H.: Roll-Up of Aircraft Trailing Vortices Using Artificial Viscosity. Journal of Aircraft, Vol. 11, No. 11, pp. 714-716, Nov. 1974.

15. Chambers, J. R.; and Anglin, E. L.: Analysis of Lateral-Directional Stability Characteristics of a Twin-Jet Fighter Airplane at High Angles of Attack. NASA TN D-5361, Aug. 1969.

16. Grafton, Sue B.; and Libbey, C. E.: Dynamic Stability Derivatives of a Twin-Jet Fighter Model for Angles of Attack from 10 to 110 Degrees. NASA TN D-6091, Jan. 1971.

17. Lamar, J. E.; and Frink, N. T.: Experimental and Analytical Study of the Longitudinal Aerodynamic Characteristics of Analytically and Empirically Designed Strake Wing Configurations at Subcritical Speeds. NASA TP-1803, June 1981.

APPENDIX A: EVALUATION OF INDUCED VELOCITY DUE TO A HORSESHOE VORTEX AND LINE VORTEX SEGMENT

The velocity field induced by a line vortex element of strength Γ is given by (Reference 10)

$$\vec{V}(\vec{R}) = \frac{\beta^2 \Gamma}{4\pi} \int_{\ell} \frac{(\vec{R}_1 - \vec{R}) \times d\ell}{R_\beta^3} \tag{A.1}$$

where

$$\beta = \sqrt{1 - M^2}$$

$$\vec{R} = X\hat{i} + Y\hat{j} + Z\hat{k}$$

$$\vec{R}_1 = X'\hat{i} + Y'\hat{j} + Z'\hat{k}$$

$$R^2_\beta = (X - X')^2 + \beta^2(Y - Y')^2 + \beta^2(Z - Z')^2$$

where (X', Y', Z') is the point on the vortex element.

The horseshoe vortex consists of a bound element and two trailing vortices (Figure 17). The induced velocity due to the bound element with end points (X_1, Y_1, Z_1) and (X_2, Y_2, Z_2), as indicated in Figure 17, is obtained by substituting $\vec{R}_1 - \vec{R} = \vec{a} + \tau\vec{\ell}$, with τ representing a fraction of the vortex element, into Equation (A.1) as follows:

$$\vec{V}(\vec{R}) = \frac{\beta^2 \Gamma}{4\pi} \vec{a} \times \vec{\ell} \int_0^1 \frac{d\tau}{(A\tau^2 + B\tau + C)^{3/2}}$$

$$= \frac{\beta^2 \Gamma}{4\pi} \vec{a} \times \vec{\ell} \, \{\frac{2B}{(B^2 - 4AC)C^{1/2}}$$

$$\frac{2(2A + B)}{(B^2 - 4AC)(A + B + C)^{1/2}}\} \text{ , } B^2 - 4AC \pm 0 \qquad \text{(A.2)}$$

where

$$A = |\vec{\ell}'|^2, \quad B = 2\vec{a}' \cdot \vec{\ell}', \quad C = |a'|^2 .$$

Further it can be shown that (Reference 10)

$$B^2 - 4AC = -4|\vec{a}' \times \vec{\ell}'|^2$$

$$2A + B = 2\vec{b}' \cdot \vec{\ell}'$$

$$A + B + C = |\vec{b}'|^2$$

where

$$\vec{a} = (X_1 - X)\hat{i} + (Y_1 - Y)\hat{j} + (Z_1 - Z)\hat{k}$$

$$\vec{b} = (X_2 - X)\hat{i} + (Y_2 - Y)\hat{j} + (Z_2 - Z)\hat{k}$$

$$\vec{\ell} = (X_2 - X_1)\hat{i} + (Y_2 - Y_1)\hat{j} + (Z_2 - Z_1)\hat{k}$$

$$\vec{a}' = (X_1 - X)\hat{i} + \beta(Y_1 - Y)\hat{j} + \beta(Z_1 - Z)\hat{k}$$

$$\vec{b}' = (X_2 - X)\hat{i} + \beta(Y_2 - Y)\hat{j} + \beta(Z_2 - Z)\hat{k}$$

$$\vec{\ell}' = (X_2 - X_1)\hat{i} + \beta(Y_2 - Y)\hat{j} + \beta(Z_2 - Z_1)\hat{k}$$

On rearranging, Equation (A.2) becomes

$$\vec{V}(\vec{R}) = \frac{\beta^2\Gamma}{4\pi} \frac{\vec{a} \times \vec{\ell}}{|a' \times \vec{\ell}'|^2} \{\frac{\vec{b}'}{|\vec{b}'|} - \frac{\vec{a}'}{|\vec{a}'|}\} \cdot \vec{\ell}' \qquad \text{(A.3)}$$

For the right trailing vortex element, Equation (A.3) becomes (if the trailing legs go to infinity)

$$\vec{V}_2(\vec{R}) = \frac{\beta^2\Gamma}{4\pi} \frac{\vec{a}_2 \times \hat{i}}{|\vec{a}'_2 \times \hat{i}|^2} \{1 - \frac{\vec{a}'_2 \cdot \hat{i}}{|\vec{a}'_2|}\} = \frac{\beta^2\Gamma}{4\pi} \vec{G}''_2 \qquad (A.4)$$

where

$$\vec{a}_2 = (x_2 - X)\hat{i} + (Y_2 - Y)\hat{j} + (Z_2 - Z)\hat{k}$$

$$\vec{a}'_2 = (X_2 - X)\hat{i} + \beta(Y_2 - Y)\hat{j} + \beta(Z_2 - Z)\hat{K}$$

For the left trailing vortex of a bound element, Equation (A.4) is still applicable except that a negative sign is needed and the subscript "2" in $\vec{a}$ and $\vec{a}'$ is replaced with "1".

Note that for the induced velocity of free vortex segments, Equation (A.3) is also applicable.

APPENDIX B: GEOMETRY DATA FOR EXAMPLE CONFIGURATIONS

Three different configurations used in this study are as follows:

1. Rectangular wing (Reference 14)
2. Twin-jet fighter airplane (Reference 16)
3. Straked wing (Reference 17)

The geometry of the above configurations is presented as follows:

a) For the rectangular wing, see Figure 18.
b) For the twin-jet fighter airplane, see Table I.
c) For the straked wing configuration, refer to Figure 19 and Table II.

TABLE I

Twin-Jet Fighter Airplane Geometry (Taken from Ref. 16)

DIMENSIONAL CHARACTERISTICS OF AIRPLANE

Overall length	57.59 ft (17.55 m)
Wing:	
Span	38.41 ft (11.71 m)
Area (including leading-edge extension)	538.34 ft^2 (50.01 m^2)
Root chord	282.00 in. (716.28 cm)
Tip chord	47.00 in. (119.38 cm)
Mean aerodynamic chord, $\bar{c}$	192.50 in. (488.95 cm)
Leading edge of $\bar{c}$ rearward of leading edge of root chord	110.76 in. (281.33 cm)
Aspect ratio	2.82
Taper ratio	0.167
Sweepback of 25-percent chord	45.00°
Dihedral (inboard 69.5 percent b/2)	0°
Dihedral (outboard 69.5 percent b/2)	12.00°
Incidence	1.00°
Airfoil section:	
Root	NACA 0006.4-64 (modified)
Tip	NACA 0003.0-64 (modified)
Aileron:	
Area (one side) rearward of hinge line	13.08 ft^2 (1.22 m^2)
Span (one aileron) (from 44.5 to 67.0 percent b/2)	4.35 ft (1.33 m) (22.5 percent b/2)
Inboard end chord (base line 103.24 in. (262.23 cm))	37.81 in. (96.04 cm) (21.3 percent $\bar{c}$)
Outboard end chord (base line 155.44 in. (394.82 cm))	34.38 in. (87.33 cm) (27.6 percent $\bar{c}$)
Spoilers:	
Area (one side)	5.44 ft^2 (0.50 m^2)
Span (from 45.3 to 67.0 percent b/2)	4.19 ft (1.28 m)
Inboard end chord	1.39 ft (0.42 m)
Outboard end chord	1.04 ft (0.32 m)
Horizontal tail:	
Area (in chord plane)	94.70 ft^2 (8.80 m^2)
Movable area	77.40 ft^2 (7.19 m^2)
Span	17.705 ft (5.40 m)
Mean aerodynamic chord of horizontal tail	6.143 ft (1.87 m)
Aspect ratio	3.30

TABLE I

Twin-Jet Fighter Airplane Geometry (Taken from Ref. 16)

DIMENSIONAL CHARACTERISTICS OF AIRPLANE – Concluded

Taper ratio	0.20
Sweepback of 25-percent chord	35.50°
Dihedral	-23.00°
Root chord (at airplane center line)	107.00 in. (271.78 cm)
Tip chord (theoretical)	21.40 in. (54.36 cm)
Airfoil section:	
Root (airplane center line)	NACA 0003.7-64 (modified)
Tip (theoretical)	NACA 0003.0-64 (modified)
Hinge-line location, percent $\bar{c}_h$	41.00
Vertical tail:	
Area	67.50 ft^2 (6.27 m^2)
Span	6.38 ft (1.94 m)
Taper ratio	0.227
Root chord	207.15 in. (526.16 cm)
Tip chord	47.10 in. (119.63 cm)
Sweepback of 25-percent chord	58.30°
Airfoil section:	
Root	NACA 0004.0-64 (modified)
Tip	NACA 0002.5-64 (modified)
Rudder:	
Area (rearward of hinge line)	11.07 ft^2 (1.03 m^2)
Hinge-line location, percent of water-line chords	80.00

TABLE II

Strake-Wing Geometry (Taken from Ref. 17)

AD 19 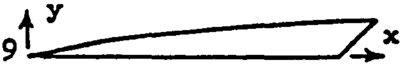			
x		y	
cm	in.	cm.	in.
0.000	0.000	0.000	0.000
0.455	0.179	0.229	0.090
1.115	0.439	0.457	0.180
1.935	0.762	0.686	0.270
2.893	1.139	0.914	0.360
3.980	1.567	1.143	0.450
5.189	2.043	1.374	0.541
7.968	3.137	1.831	0.721
11.247	4.428	2.289	0.901
15.085	5.939	2.746	1.081
19.558	7.700	3.203	1.261
24.491	9.642	3.660	1.441
30.170	11.878	4.120	1.622
38.892	15.312	4.577	1.802

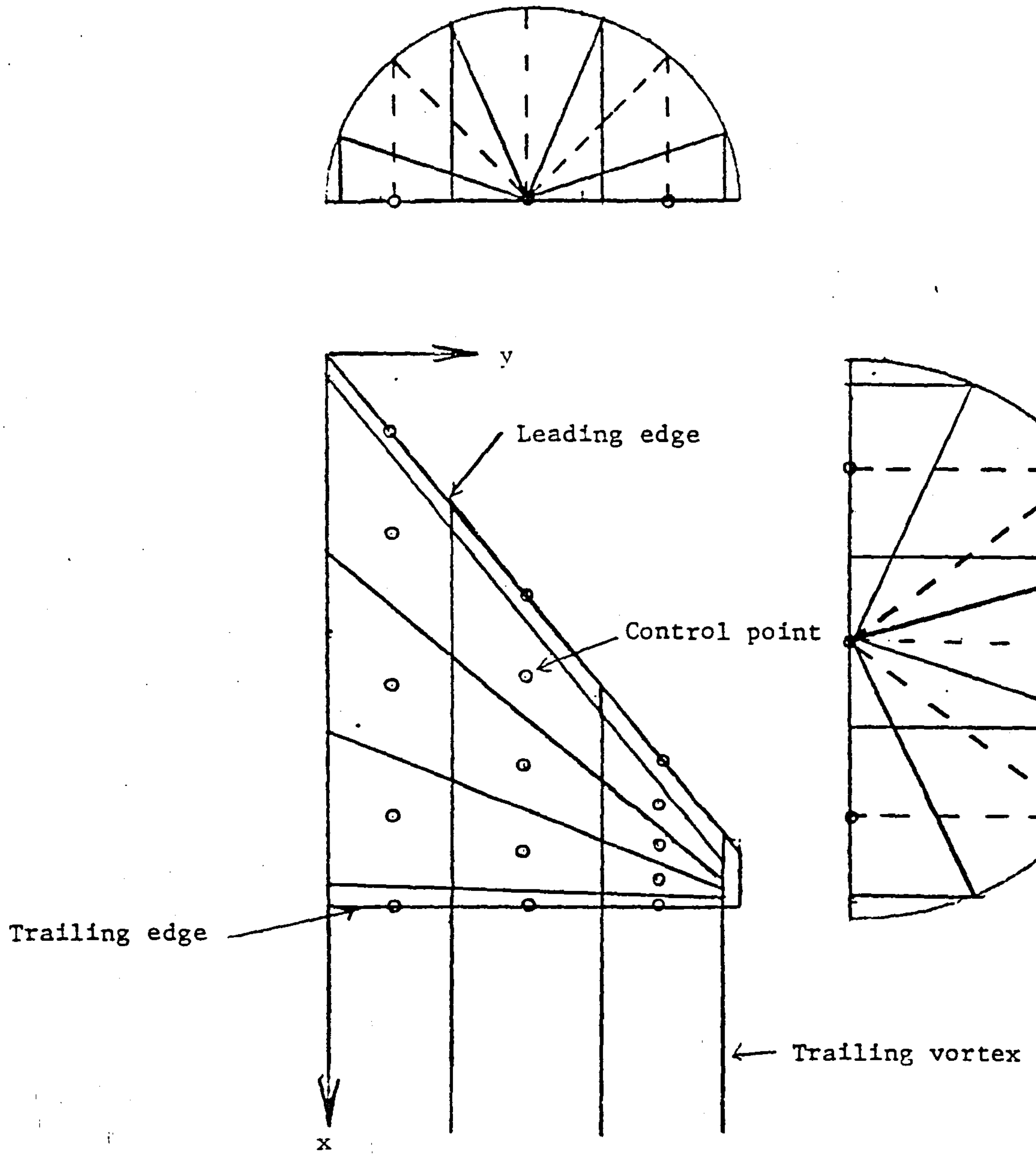

Wing Geometry

Fig. 1

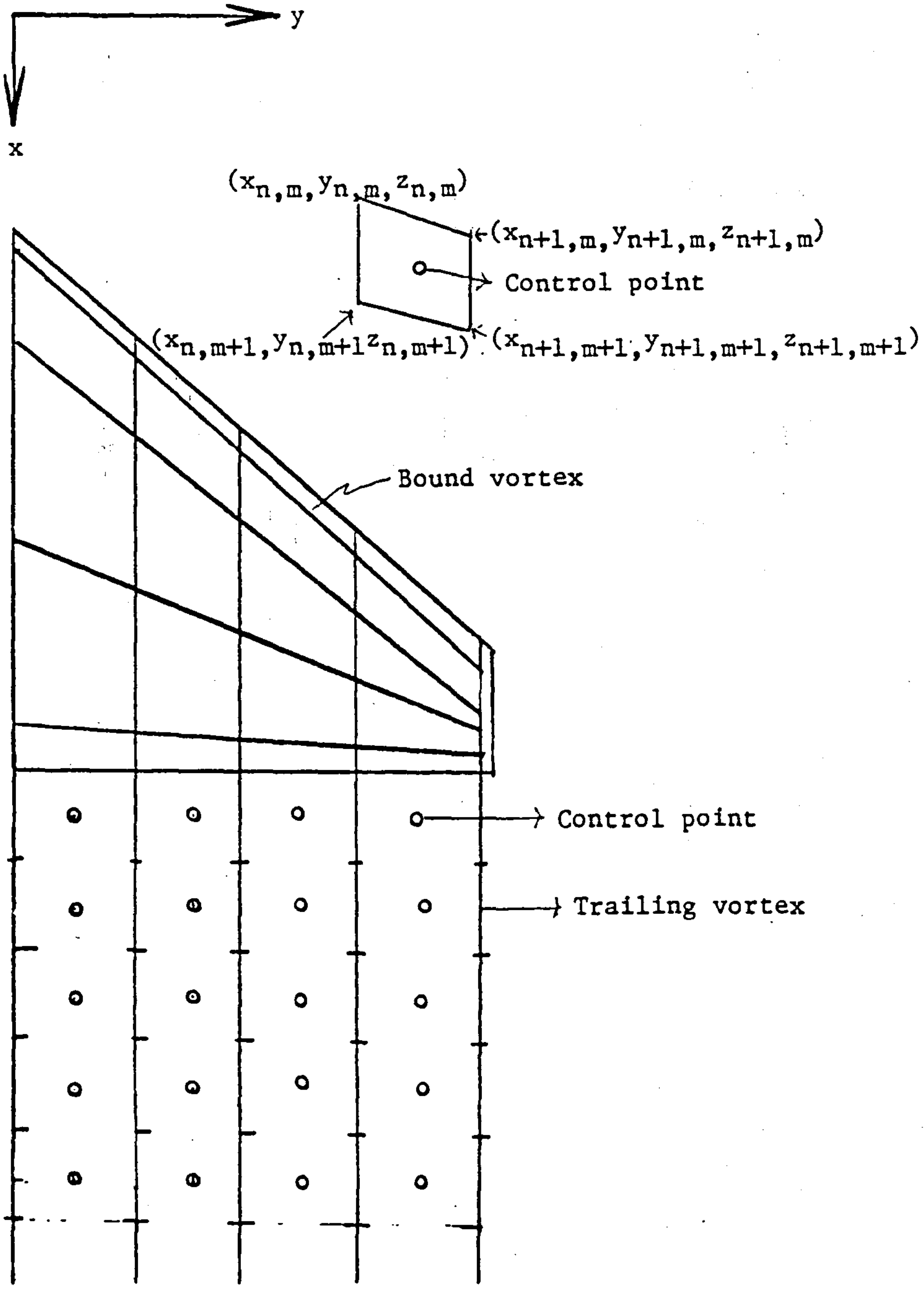

Wake Geometry

Fig. 2

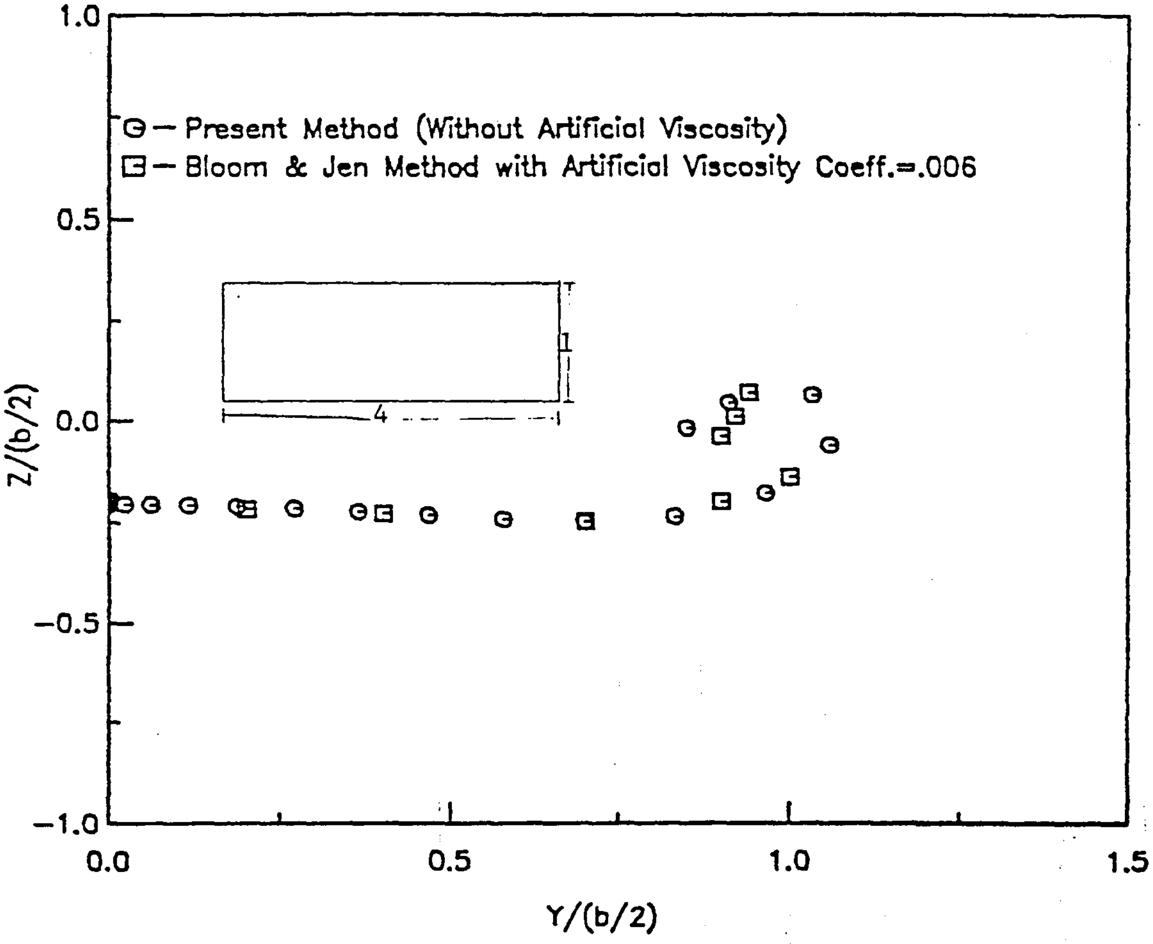

Wake Shape of the Rectangular Wing in Level Flight at 15 Chord Lengths Behind T.E

Fig. 3

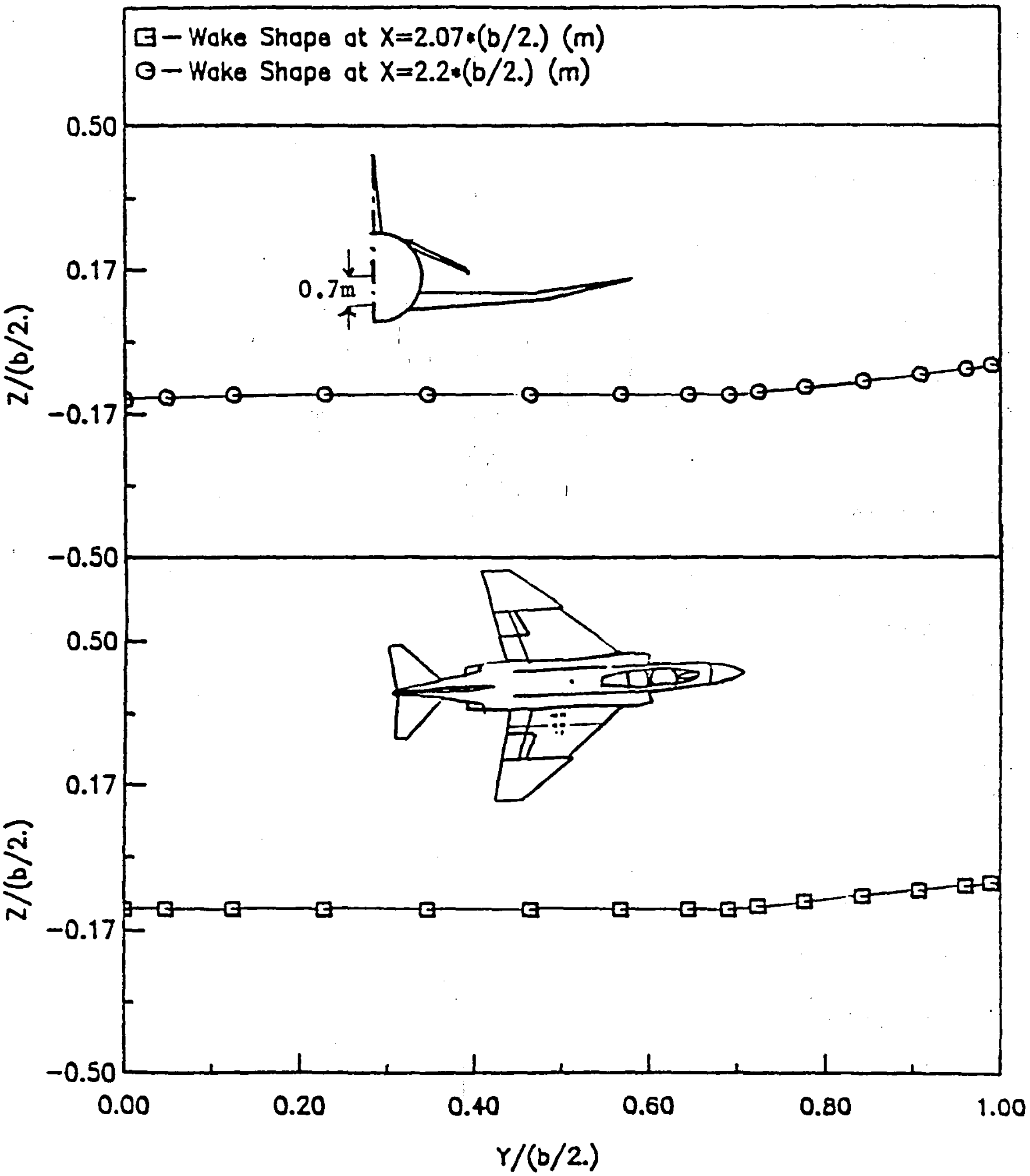

Fig. 4(a) The Wake Shape of a Wing-Body-Tail Configuration at Alpha = 0.5 deg.

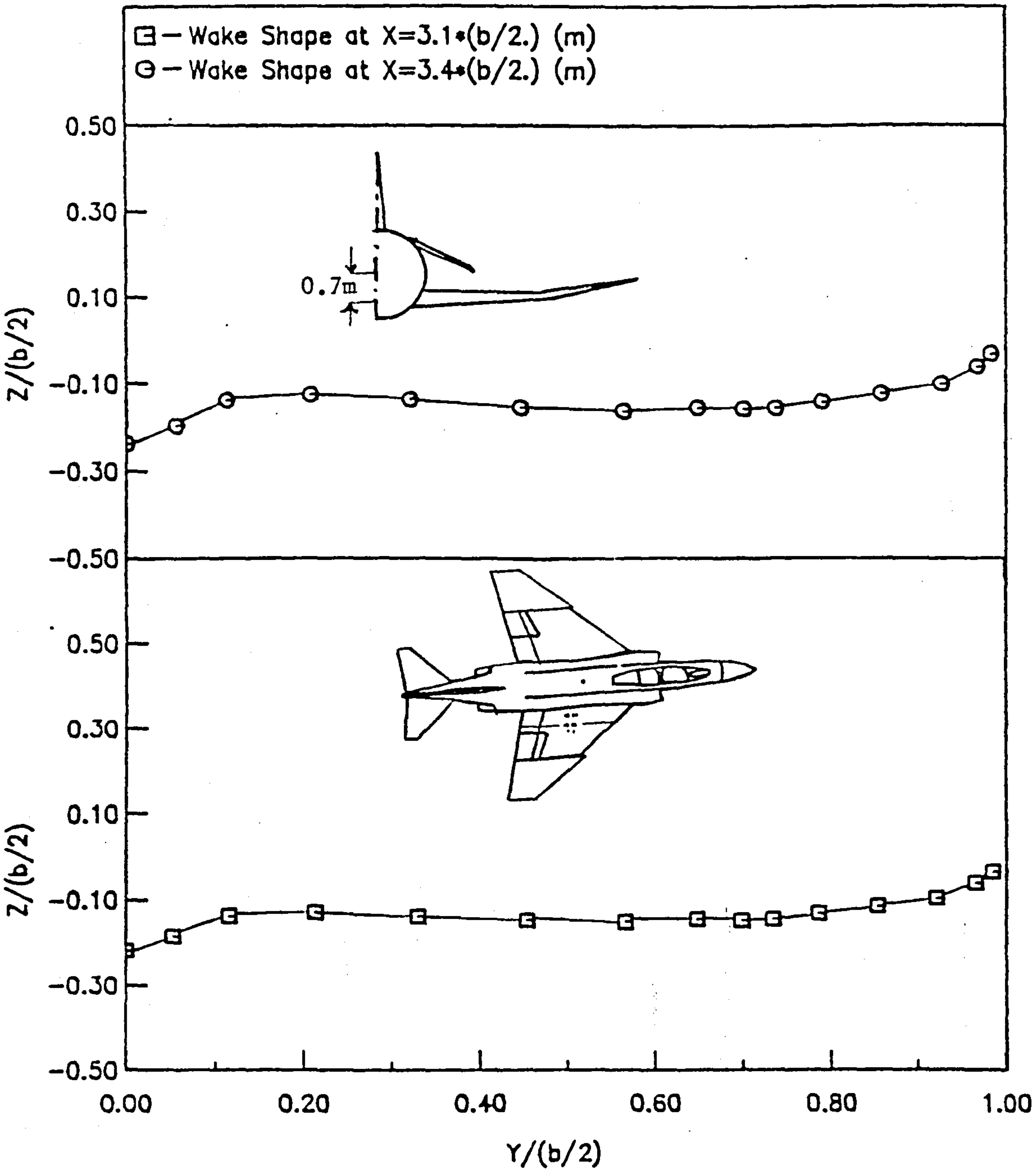

Fig. 4(b) The Wake Shape of a Wing-Body-Tail Configuration at Alpha = 0.5 deg.

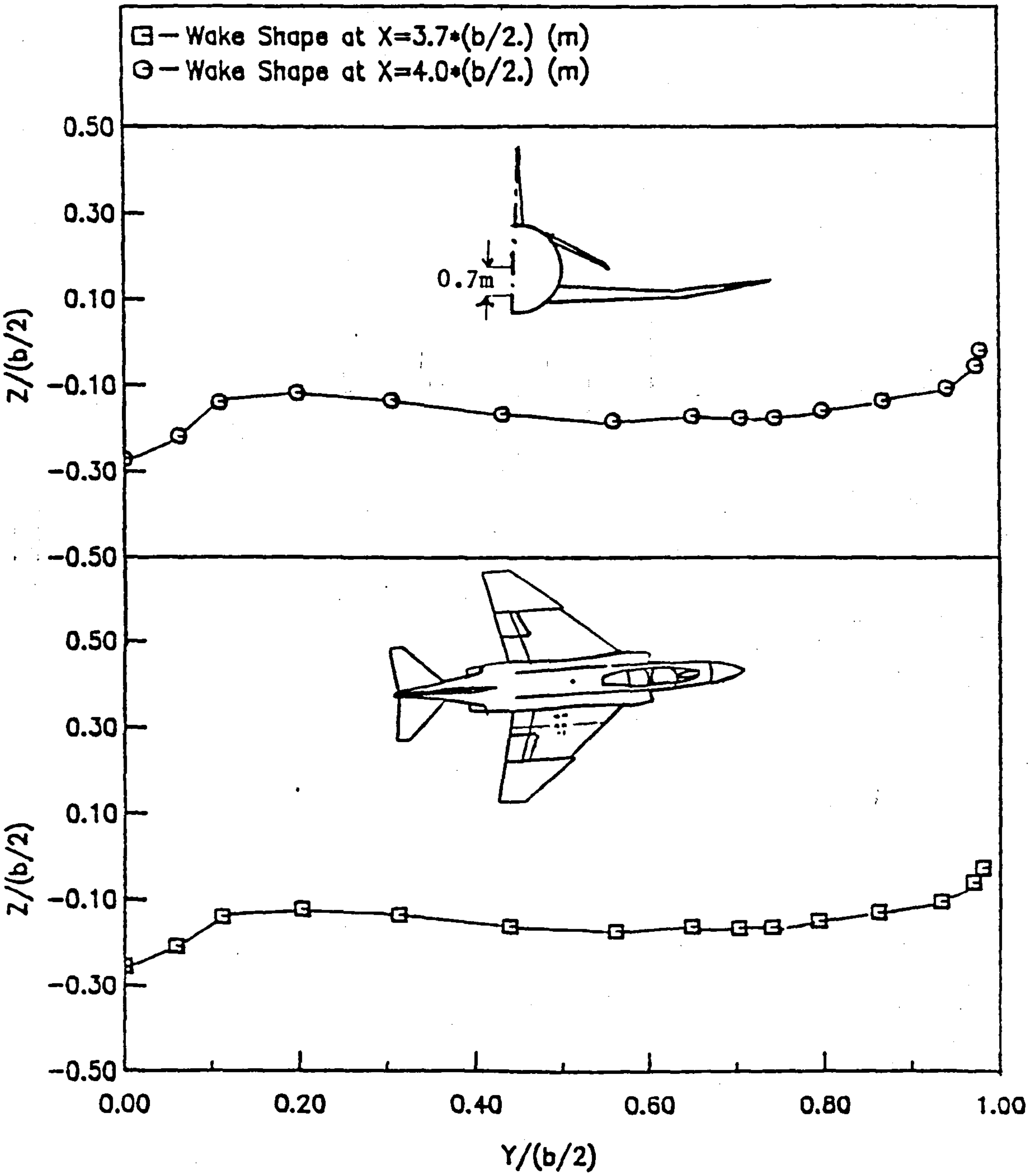

Fig. 4(c) The Wake Shape of a Wing-Body-Tail Configuration at Alpha = 0.5 deg.

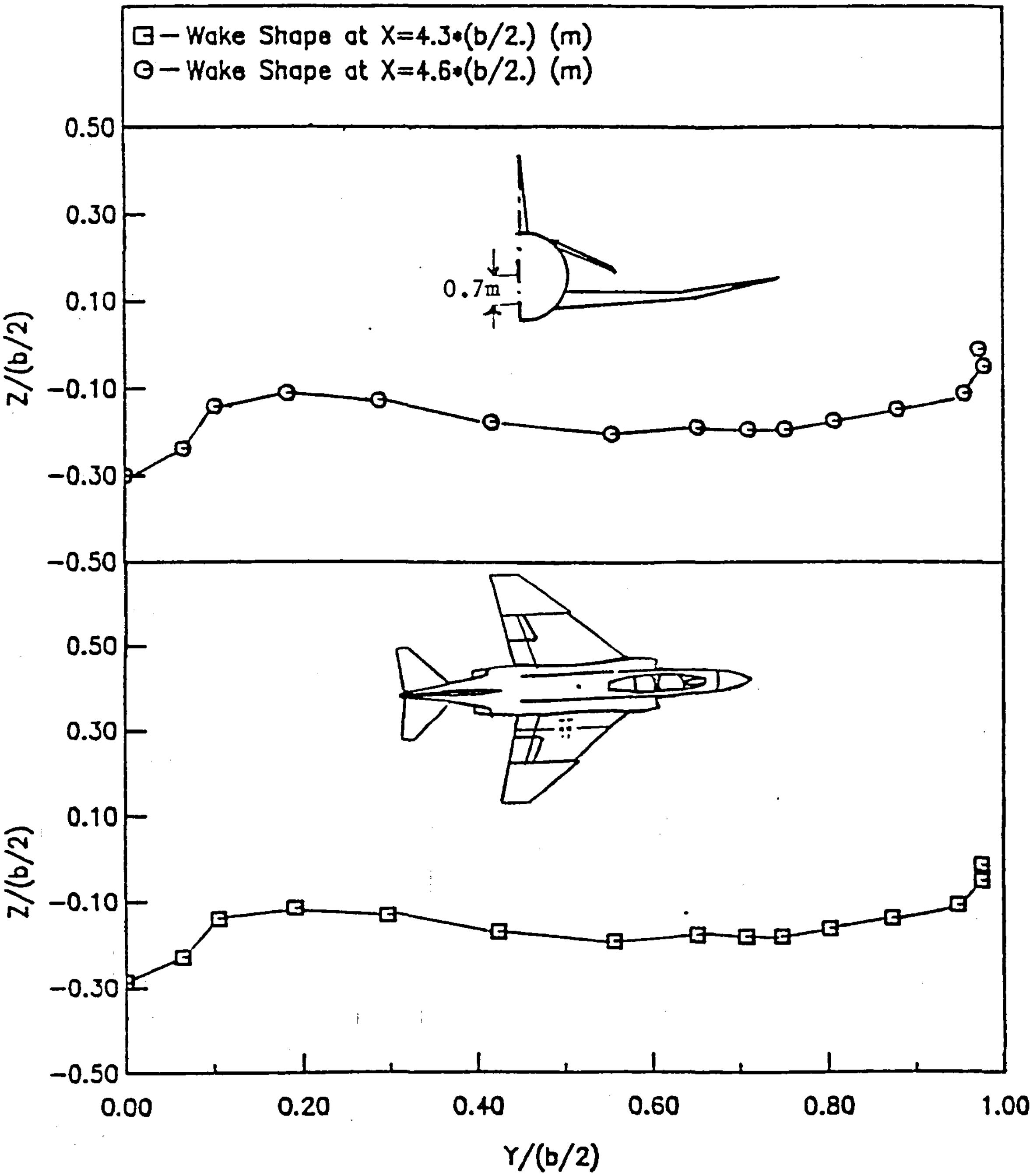

Fig. 4(d) The Wake Shape of a Wing-Body-Tail Configuration at Alpha = 0.5 deg.

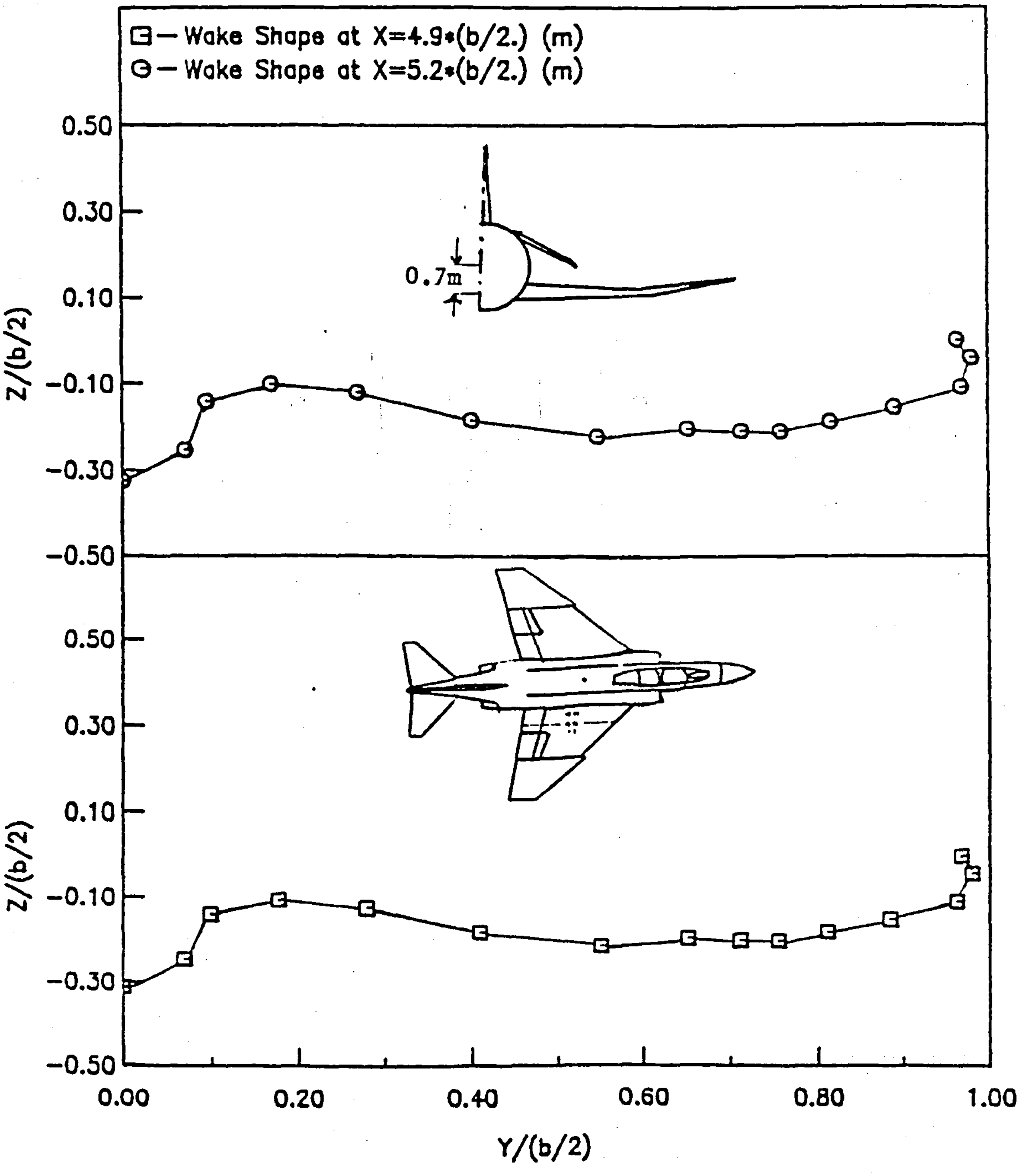

Fig. 4(e) The Wake Shape of a Wing-Body-Tail Configuration at Alpha = 0.5 deg.

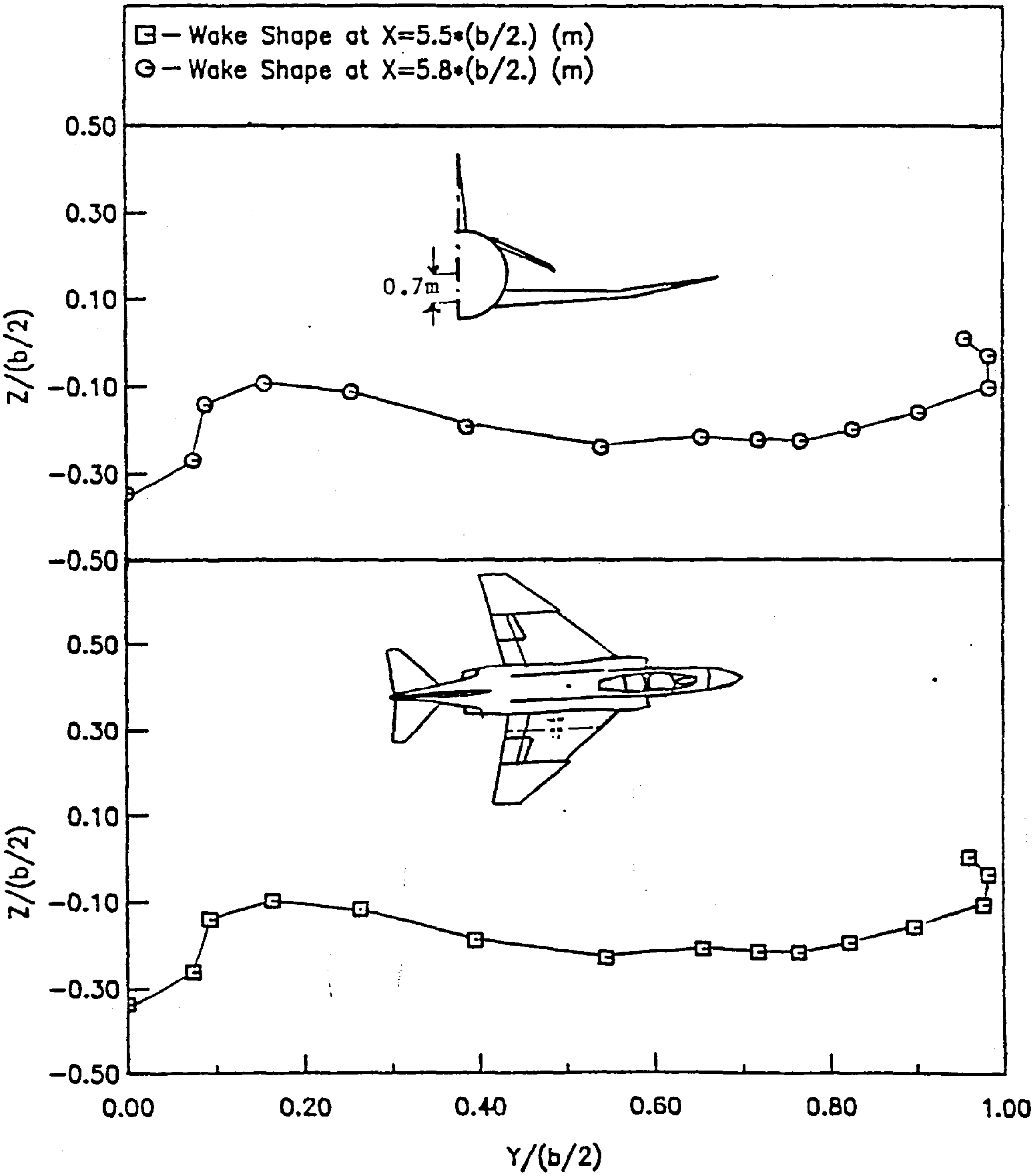

Fig. 4(f) The Wake Shape of a Wing-Body-Tail Configuration at Alpha = 0.5 deg.

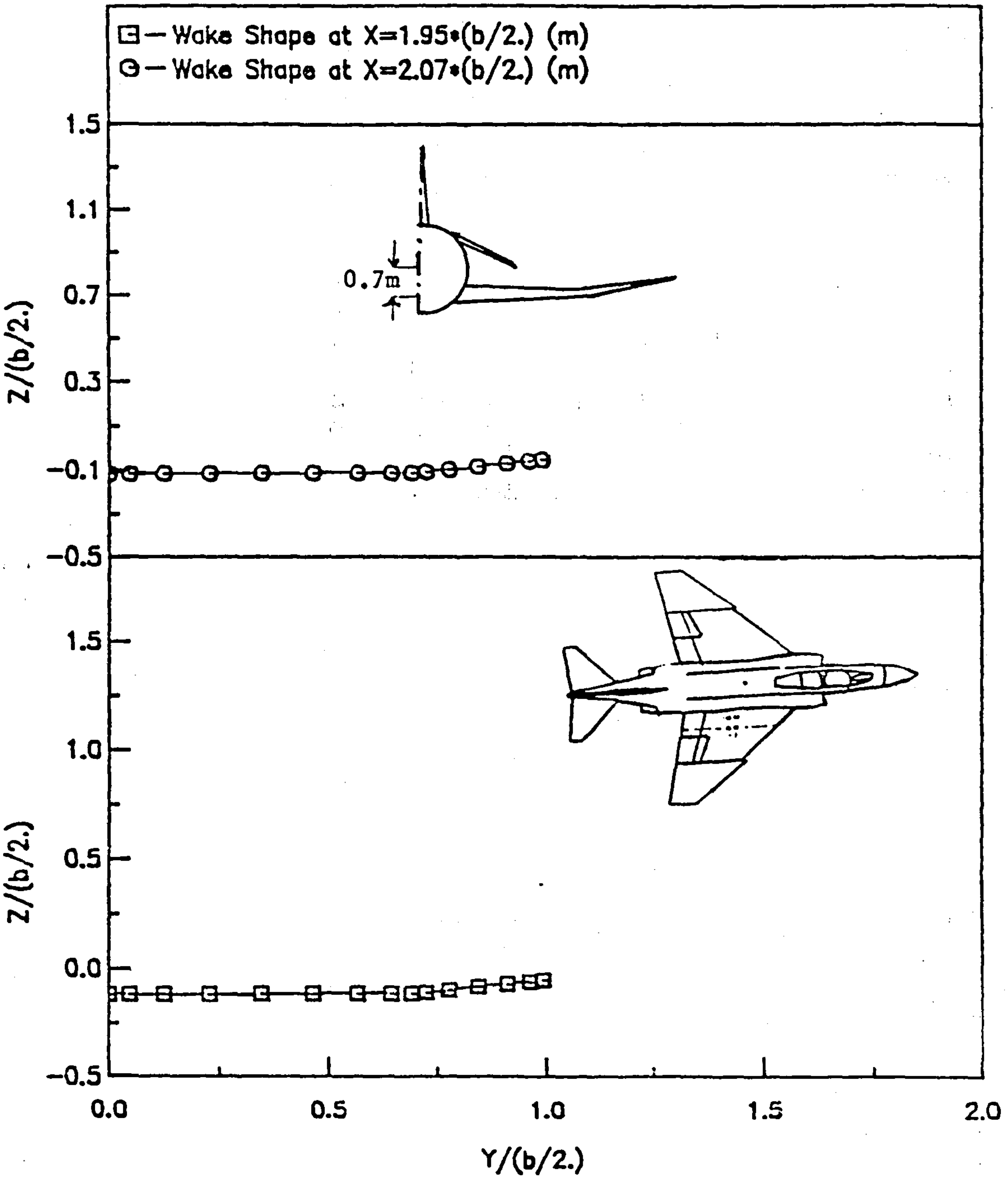

Fig. 5(a) The Wake Shape of a Wing-Body-Tail Configuration at Alpha = 20.0 deg.

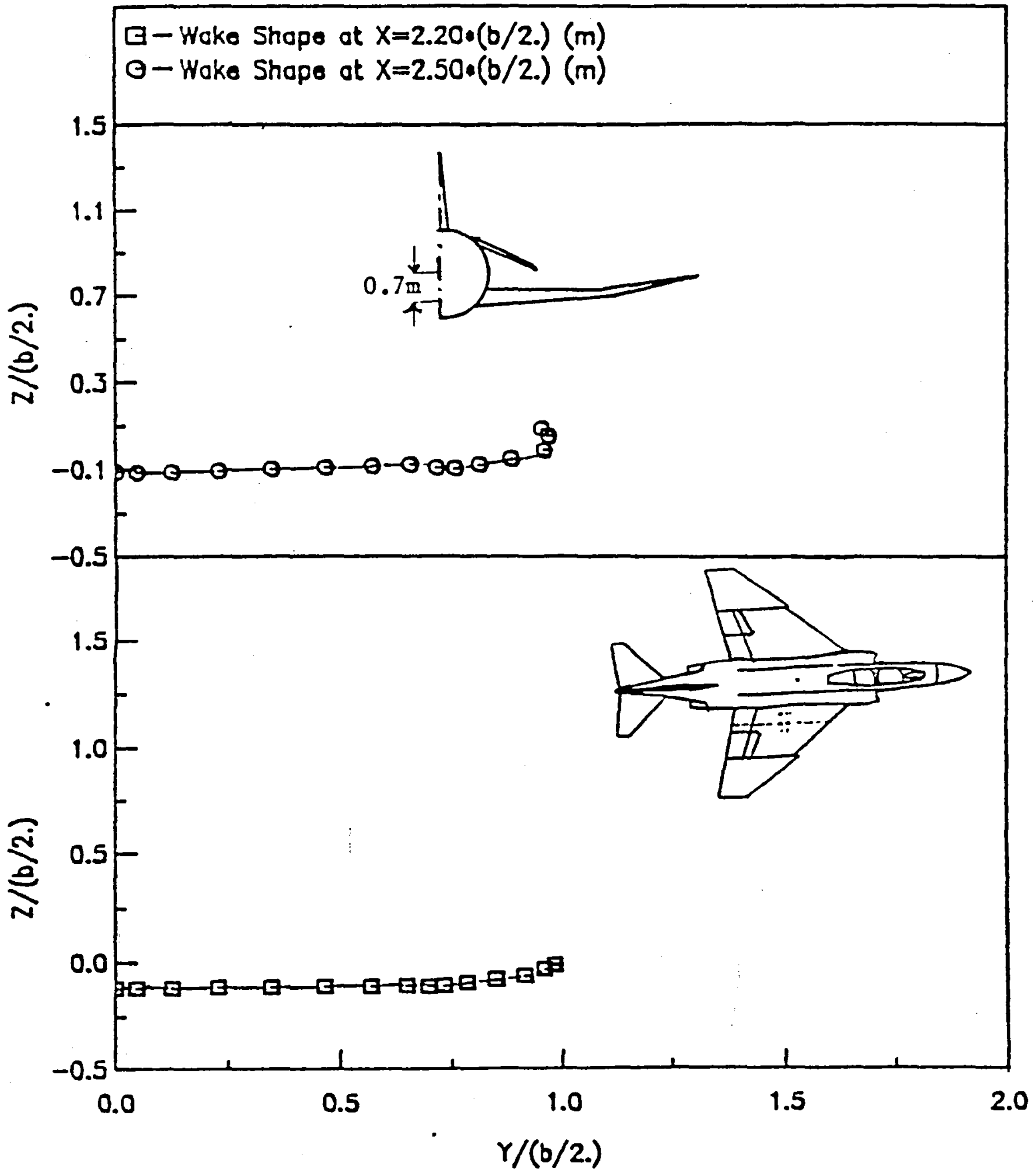

Fig. 5(b) The Wake Shape of a Wing-Body-Tail Configuration at Alpha = 20.0 deg.

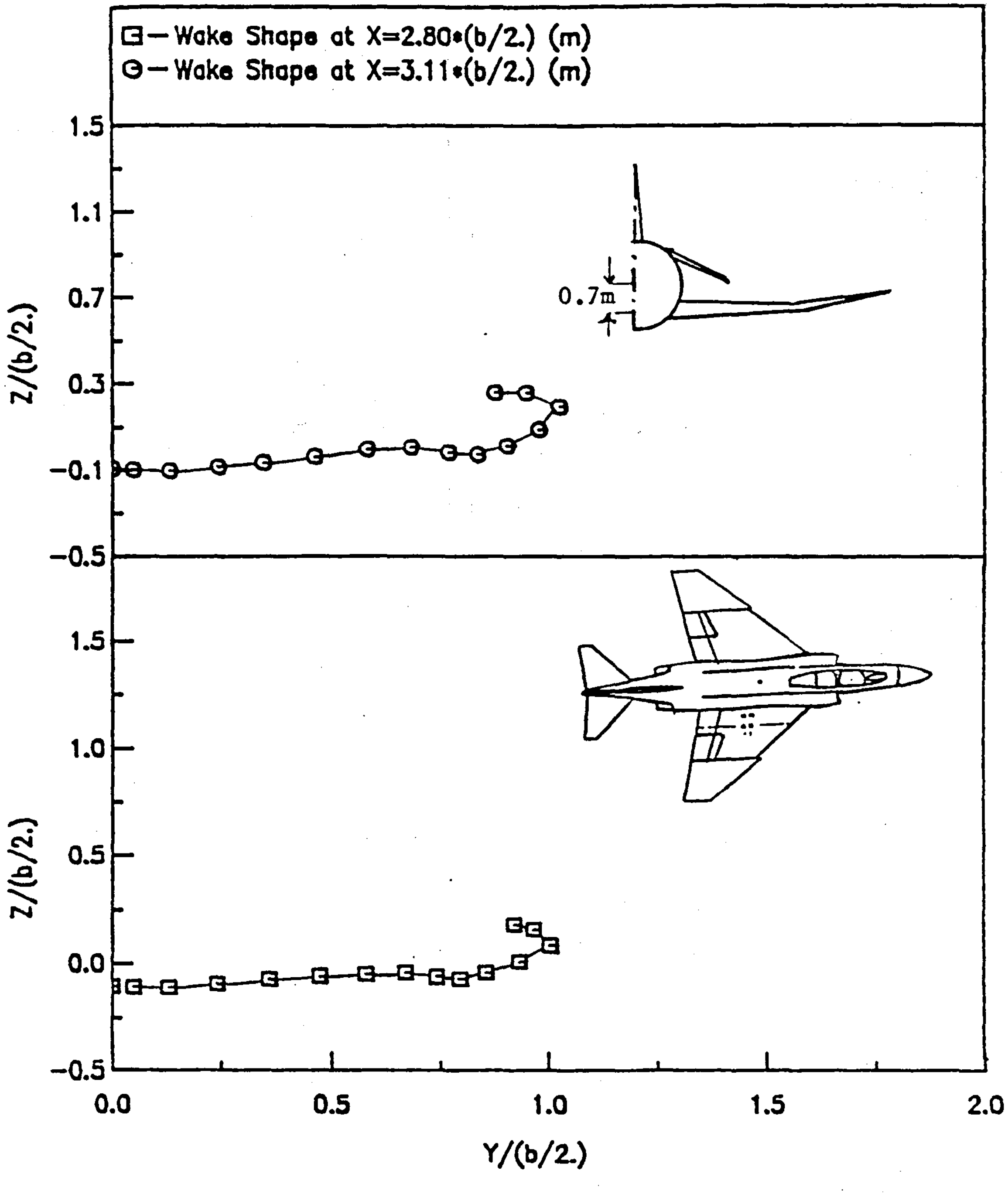

Fig. 5(c) The Wake Shape of a Wing-Body-Tail Configuration at Alpha = 20.0 deg.

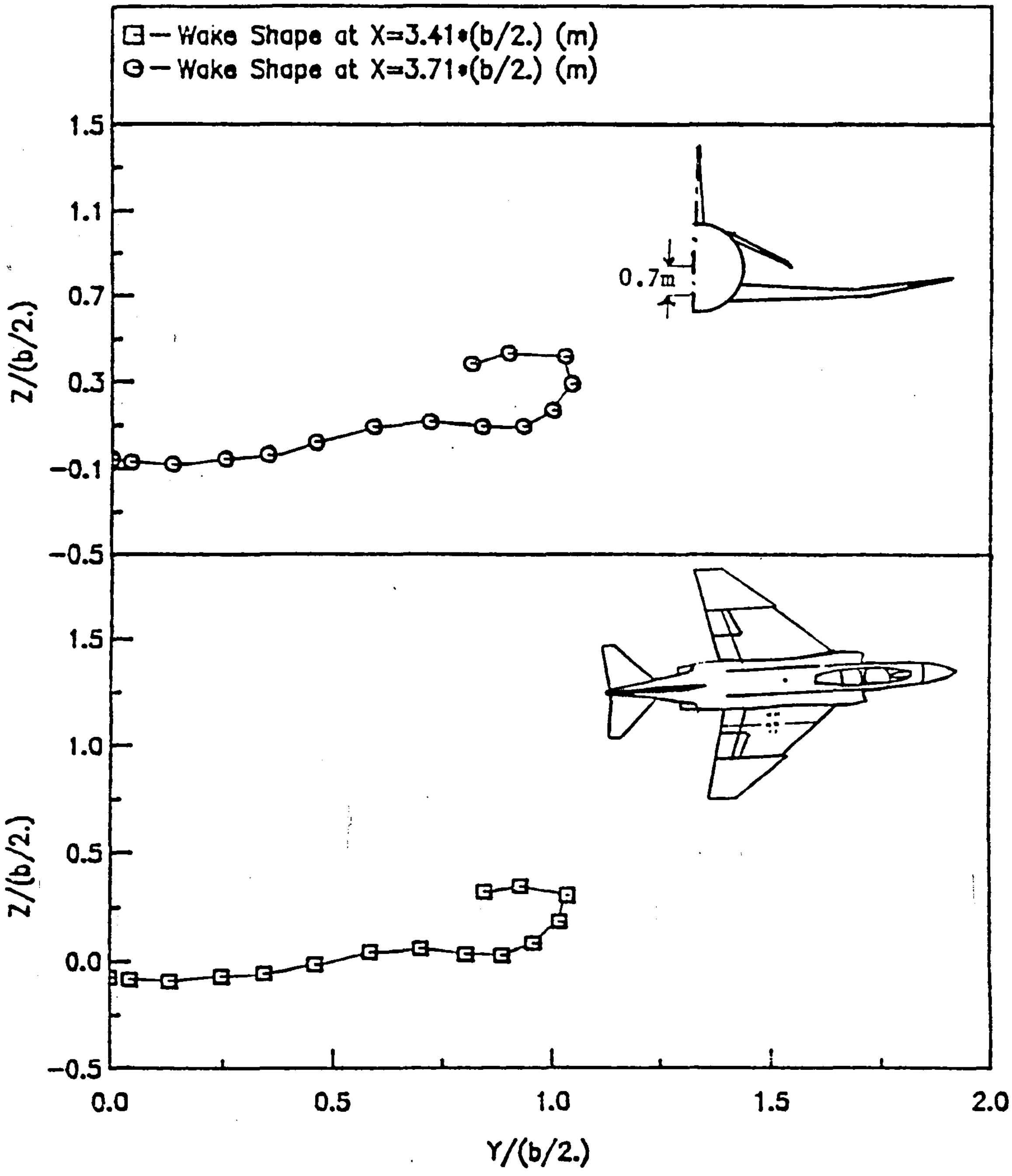

Fig. 5(d) The Wake Shape of a Wing-Body-Tail Configuration at Alpha = 20.0 deg.

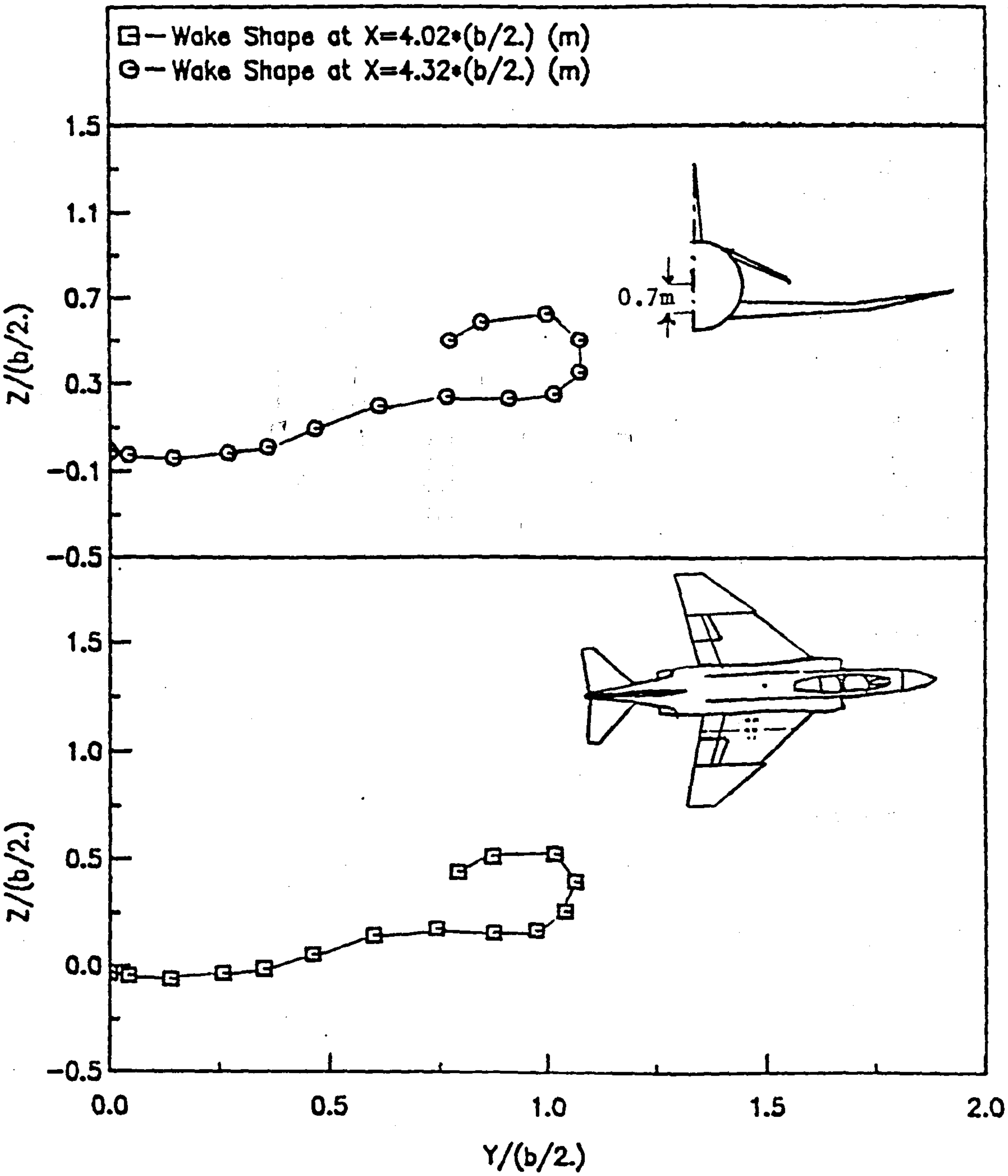

Fig. 5(e) The Wake Shape of a Wing-Body-Tail Configuration at Alpha = 20.0 deg.

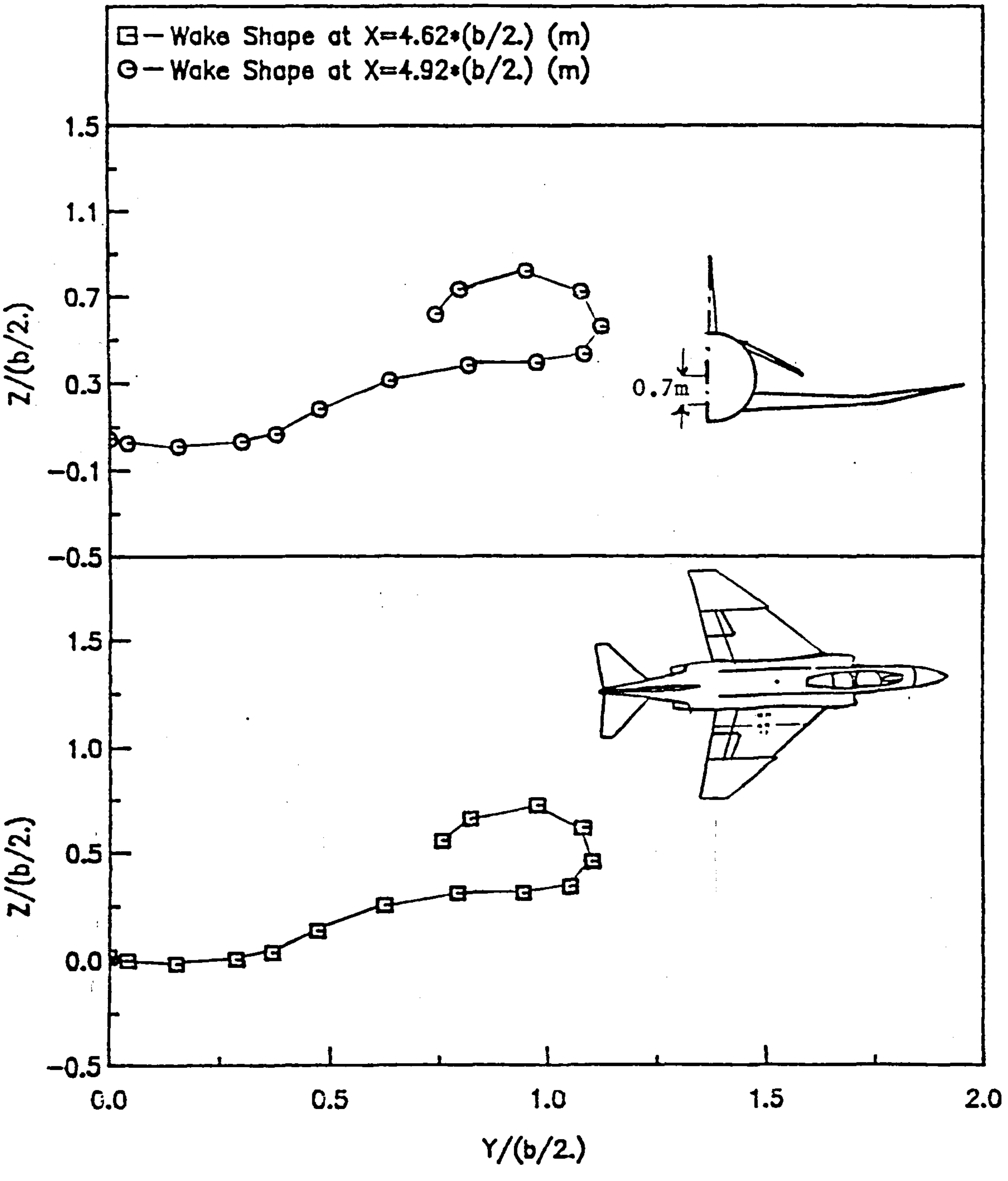

Fig. 5(f) The Wake Shape of a Wing-Body-Tail Configuration at Alpha = 20.0 deg.

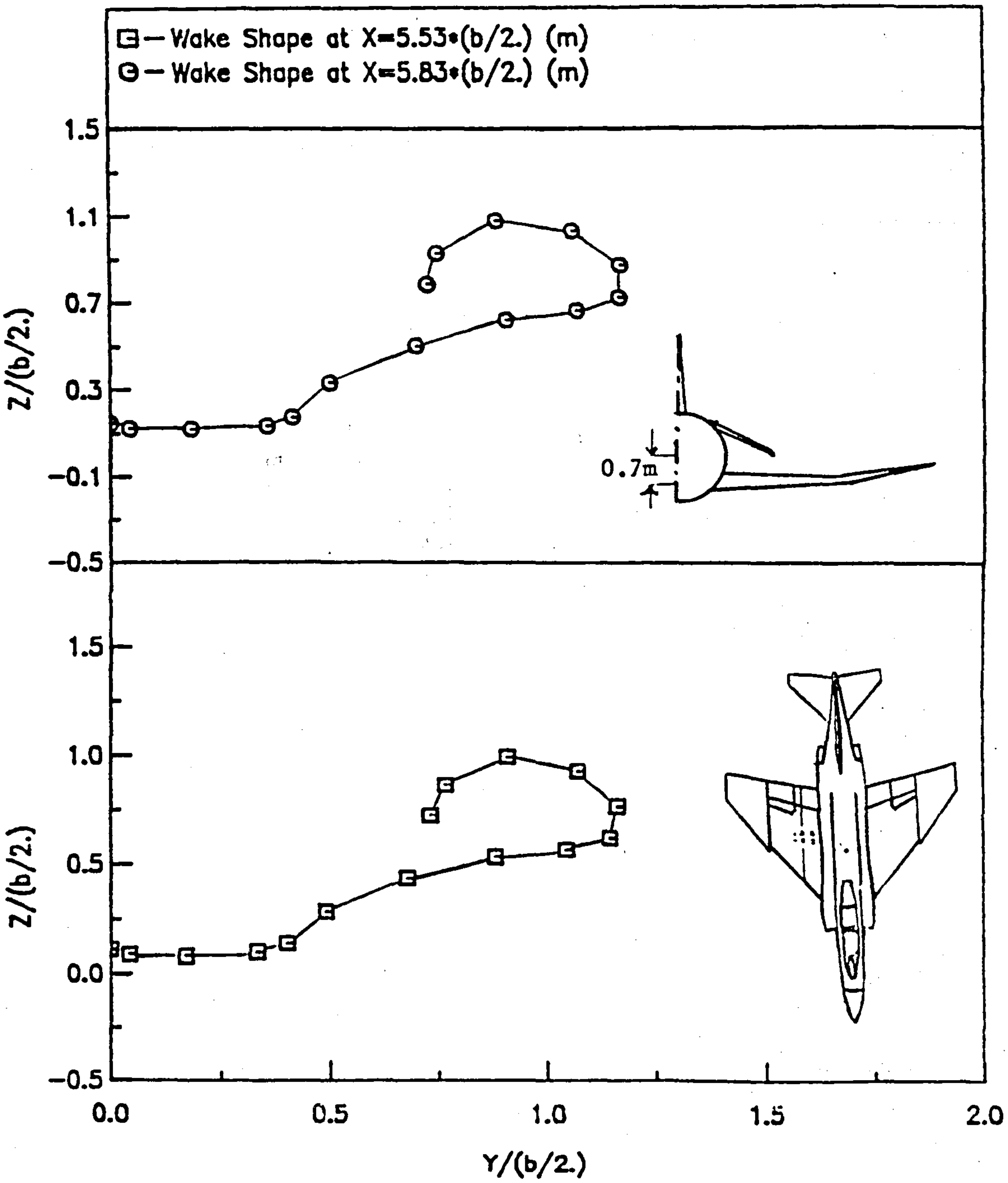

Fig. 5(g) The Wake Shape of a Wing-Body-Tail Configuration at Alpha = 20.0 deg.

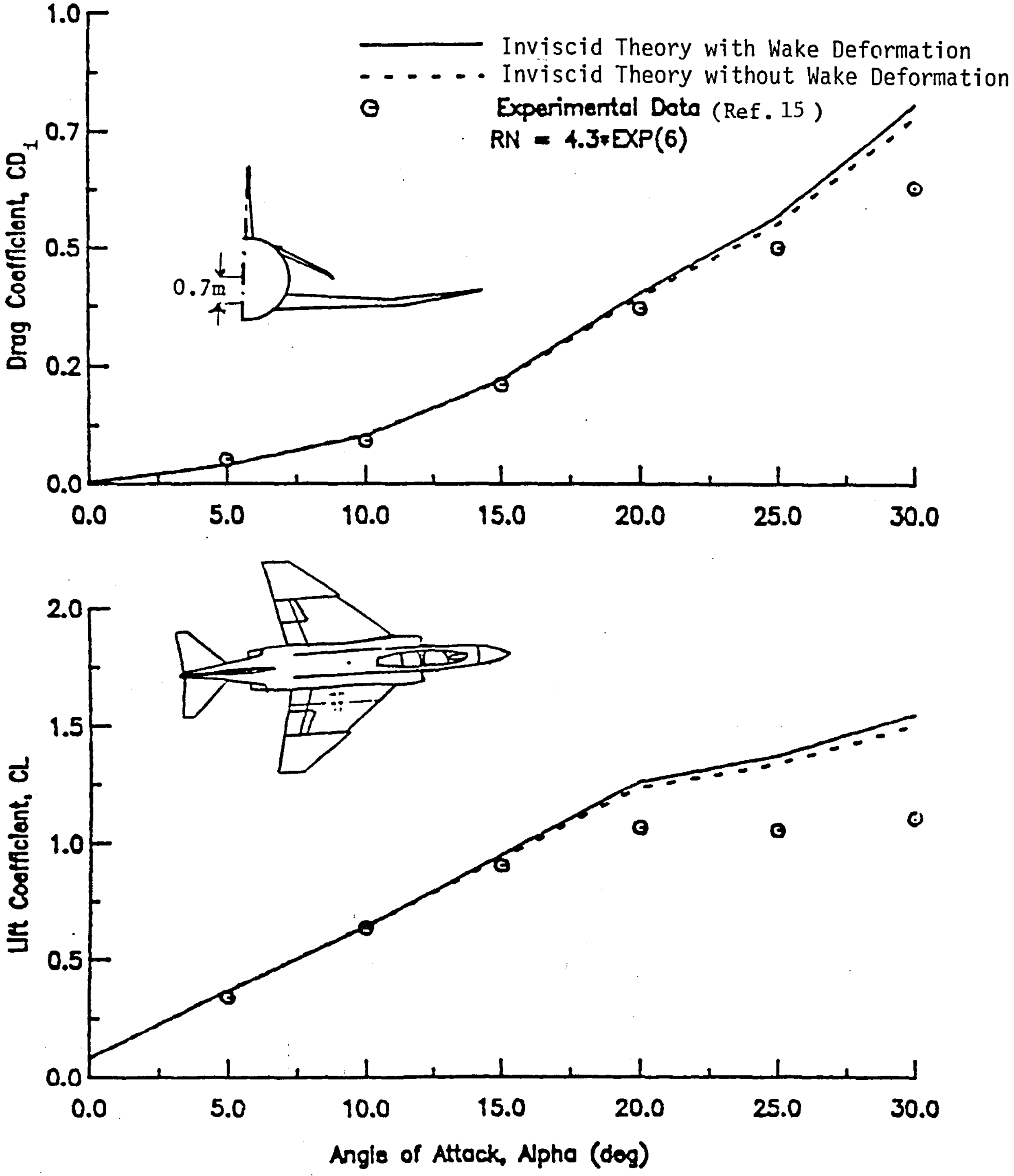

Fig. 6(a) Static Longitudinal Characteristics of a Wing-Body-Tail Configuration

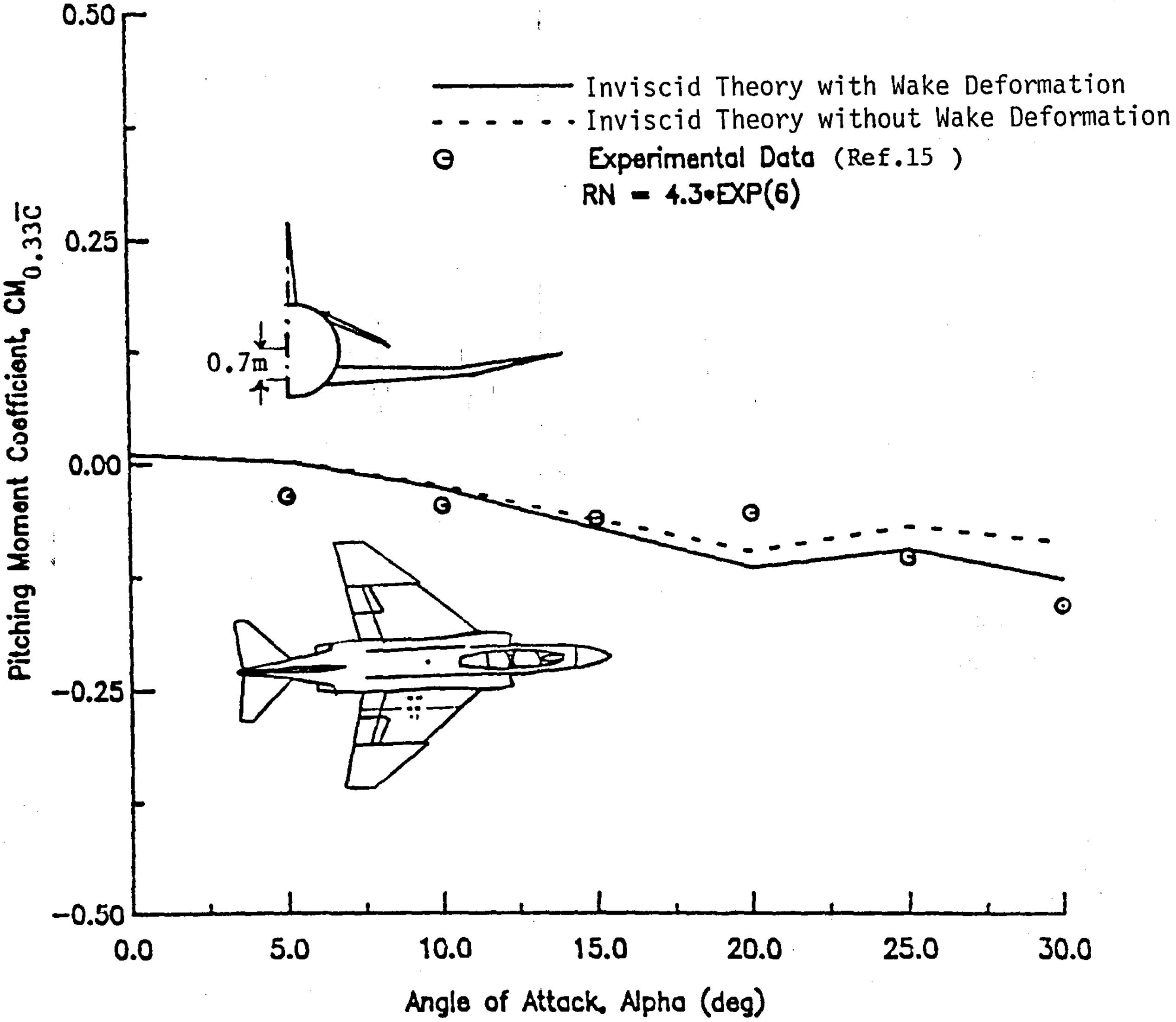

Fig. 6(b) Static Longitudinal Characteristics of a Wing-Body-Tail Configuration (Cont)

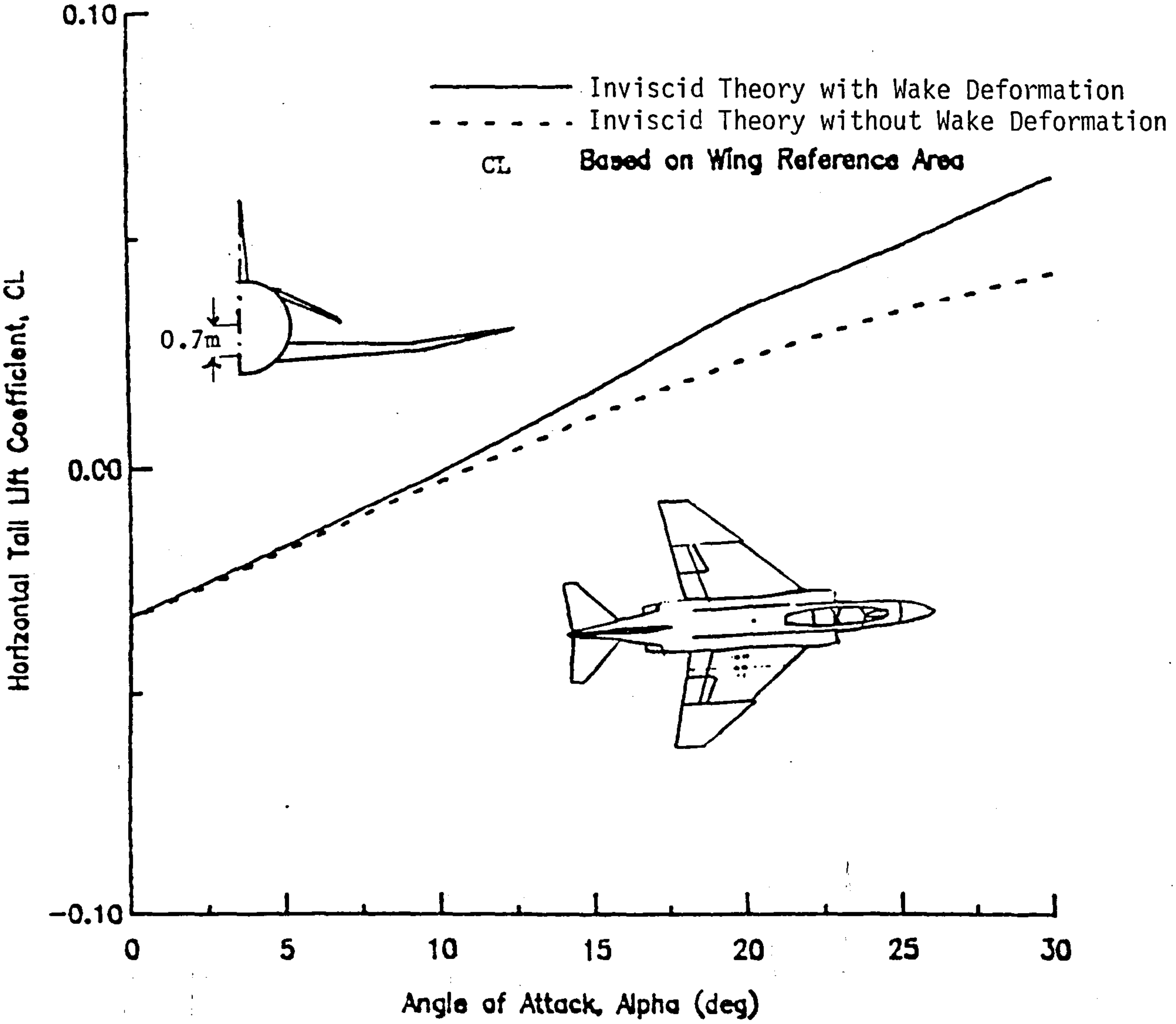

Fig. 7(a) Static Longitudinal Characteristics of Tail Plane of a Wing-Body-Tail Configuration

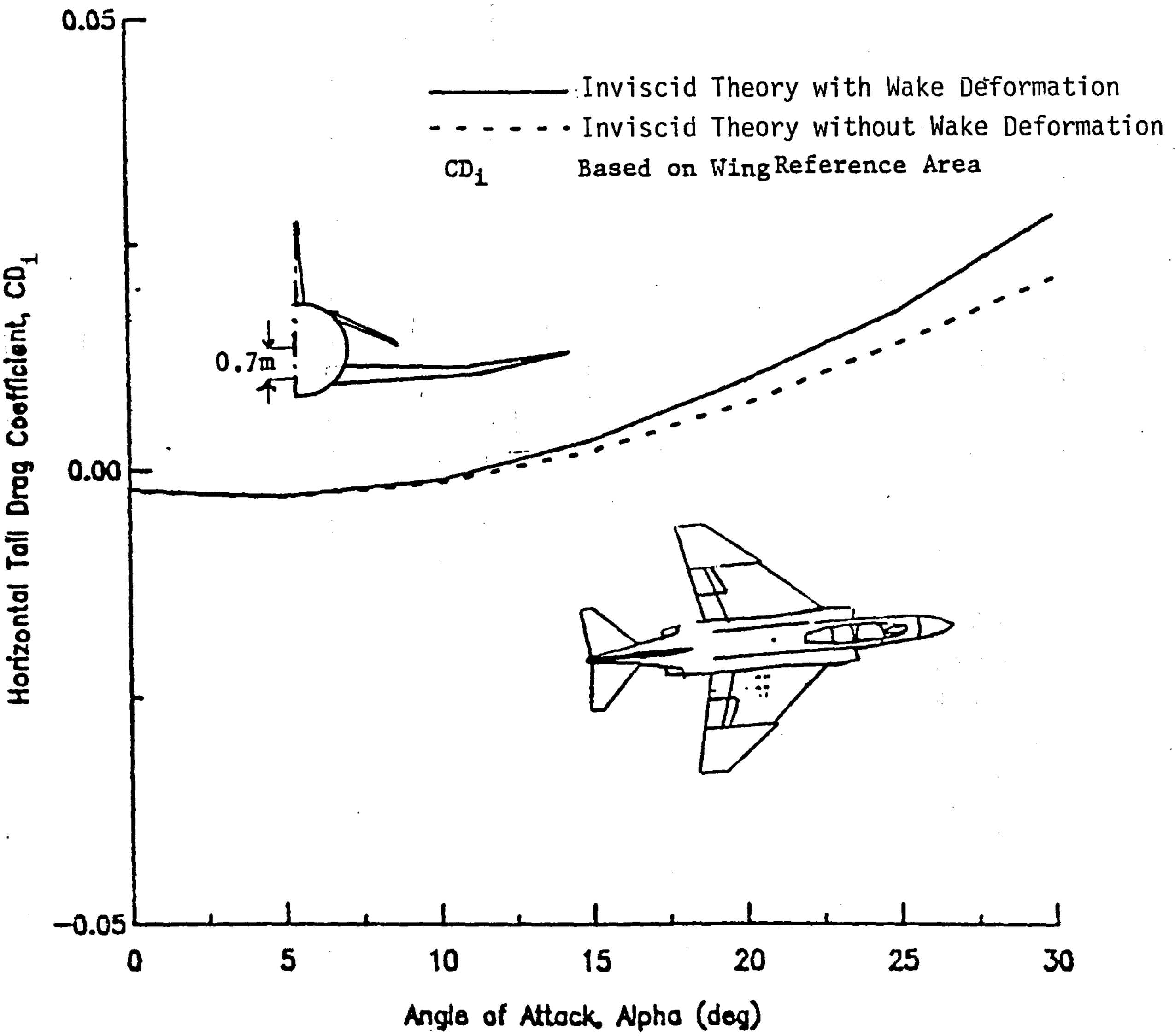

Fig. 7(b) Static Longitudinal Characteristics of Tail Plane of a Wing-Body-Tail Configuration

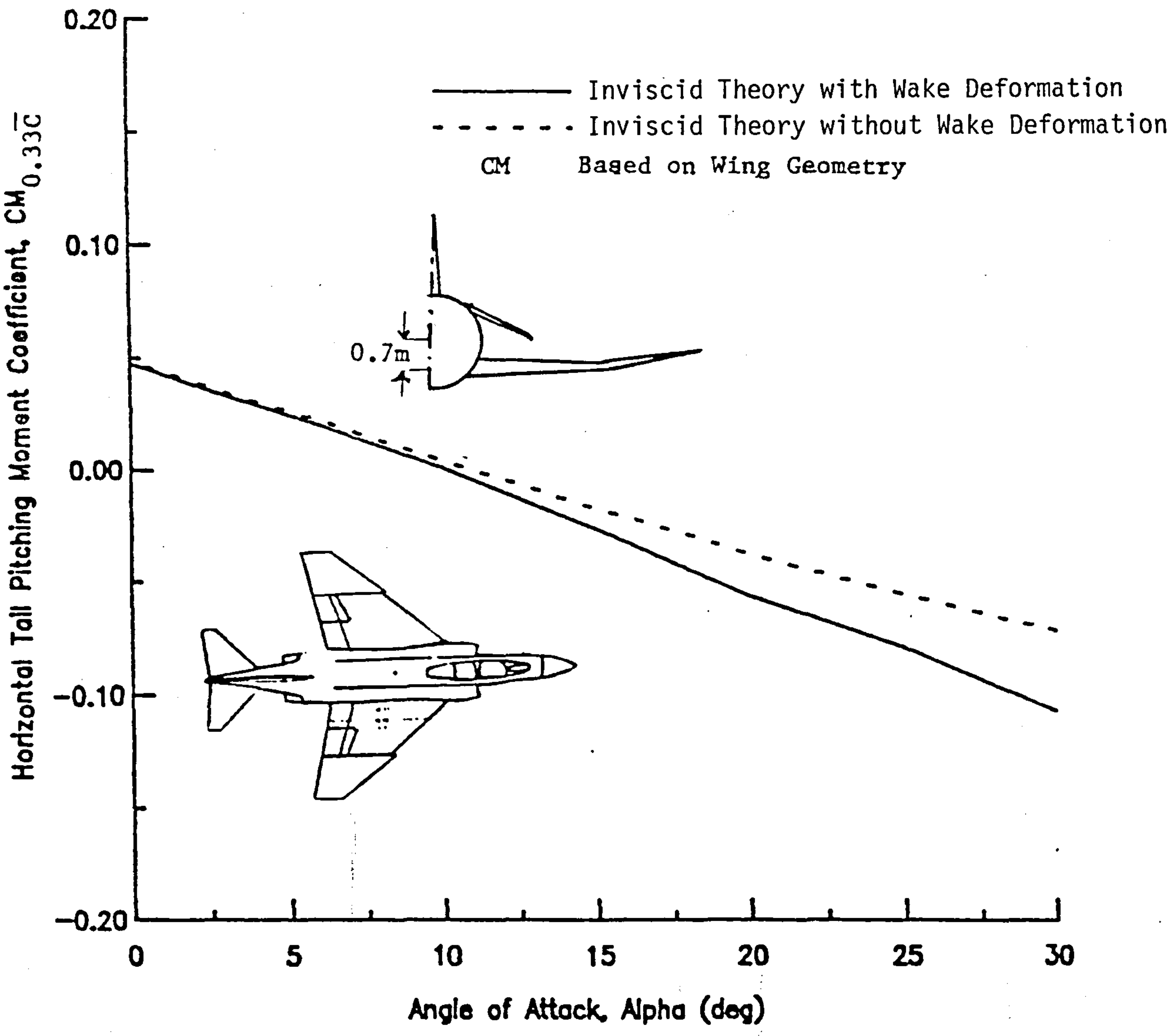

Fig. 7(c) Static Longitudinal Characteristics of Tail Plane of a Wing-Body-Tail Configuration

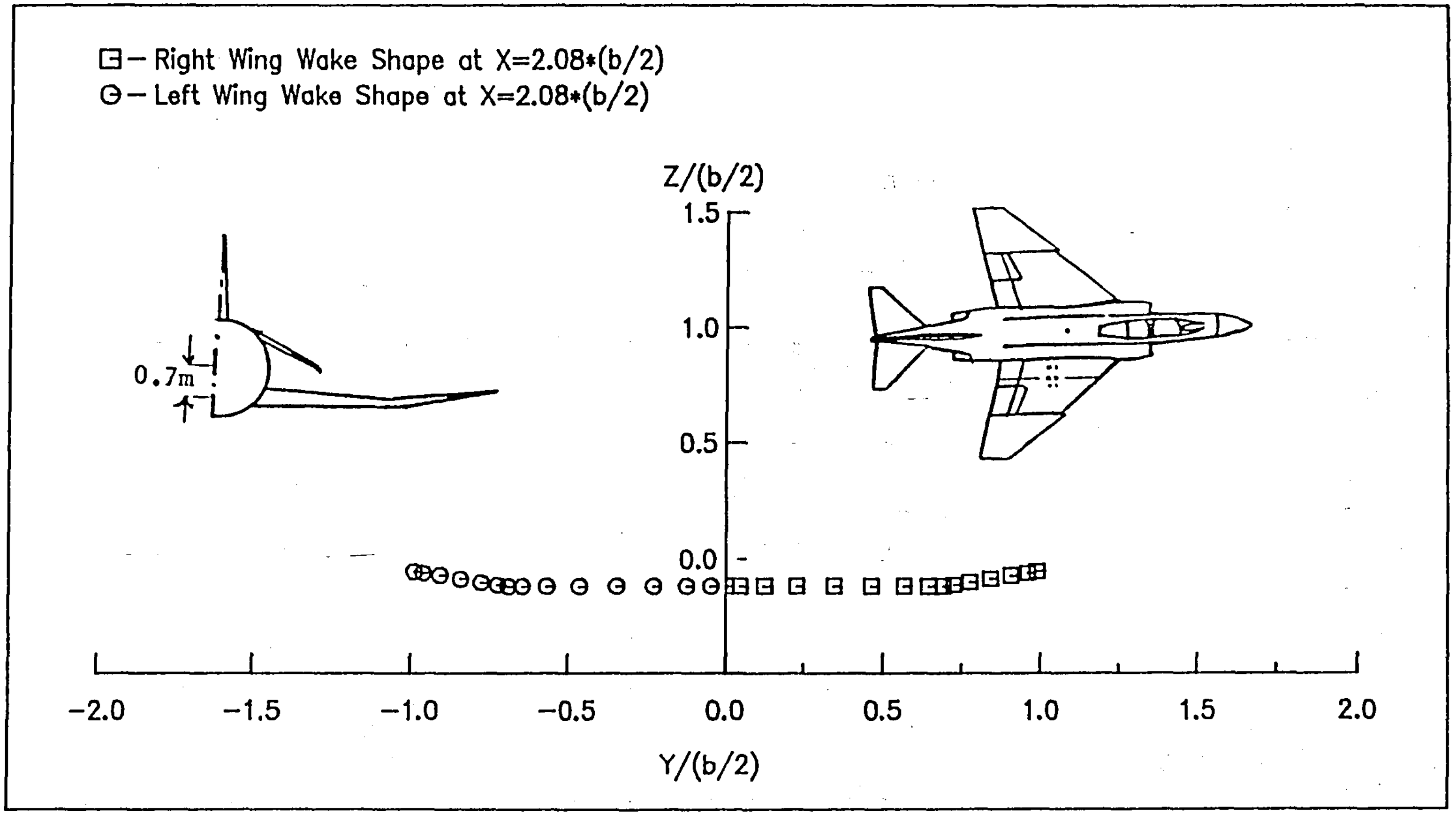

Fig. 8(a) The Wake Shape of a Wing_Body_Tail Configuration
at Alpha = 20 and Beta = 5 deg.

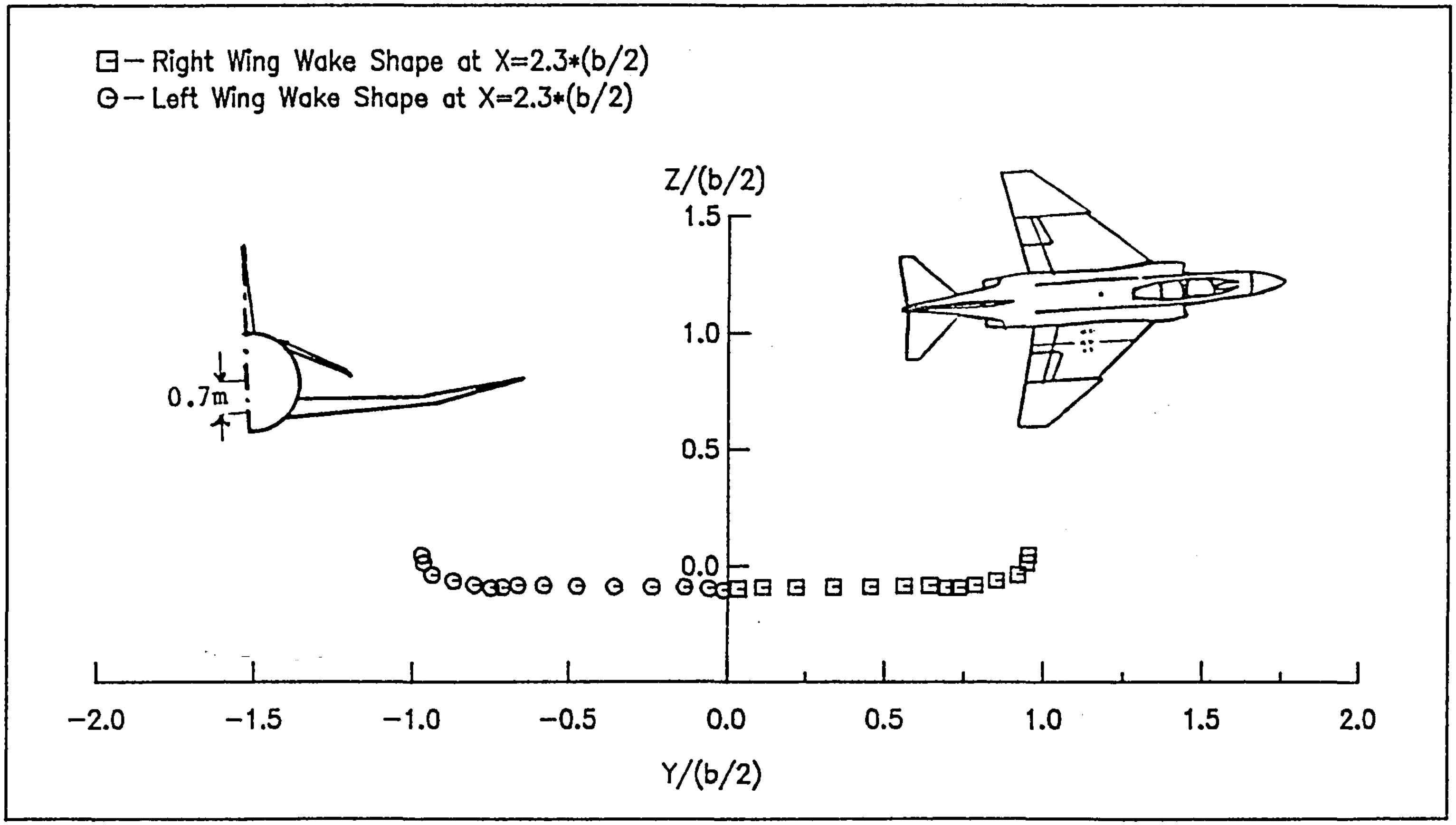

Fig. 8(b) The Wake Shape of a Wing_Body_Tail Configuration at Alpha = 20 and Beta = 5 deg.

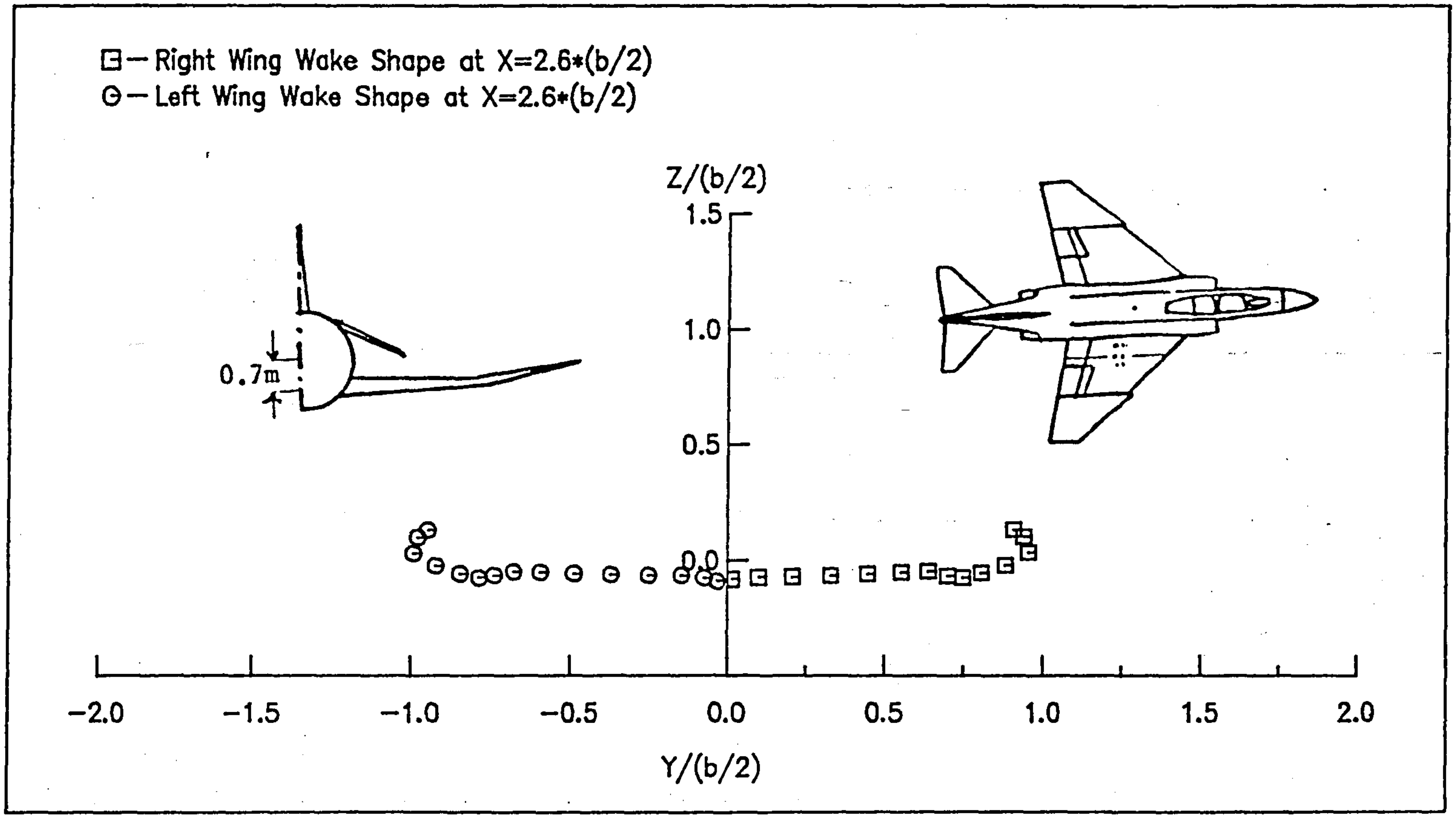

Fig. 8(c) The Wake Shape of a Wing_Body_Tail Configuration
at Alpha = 20 and Beta = 5 deg.

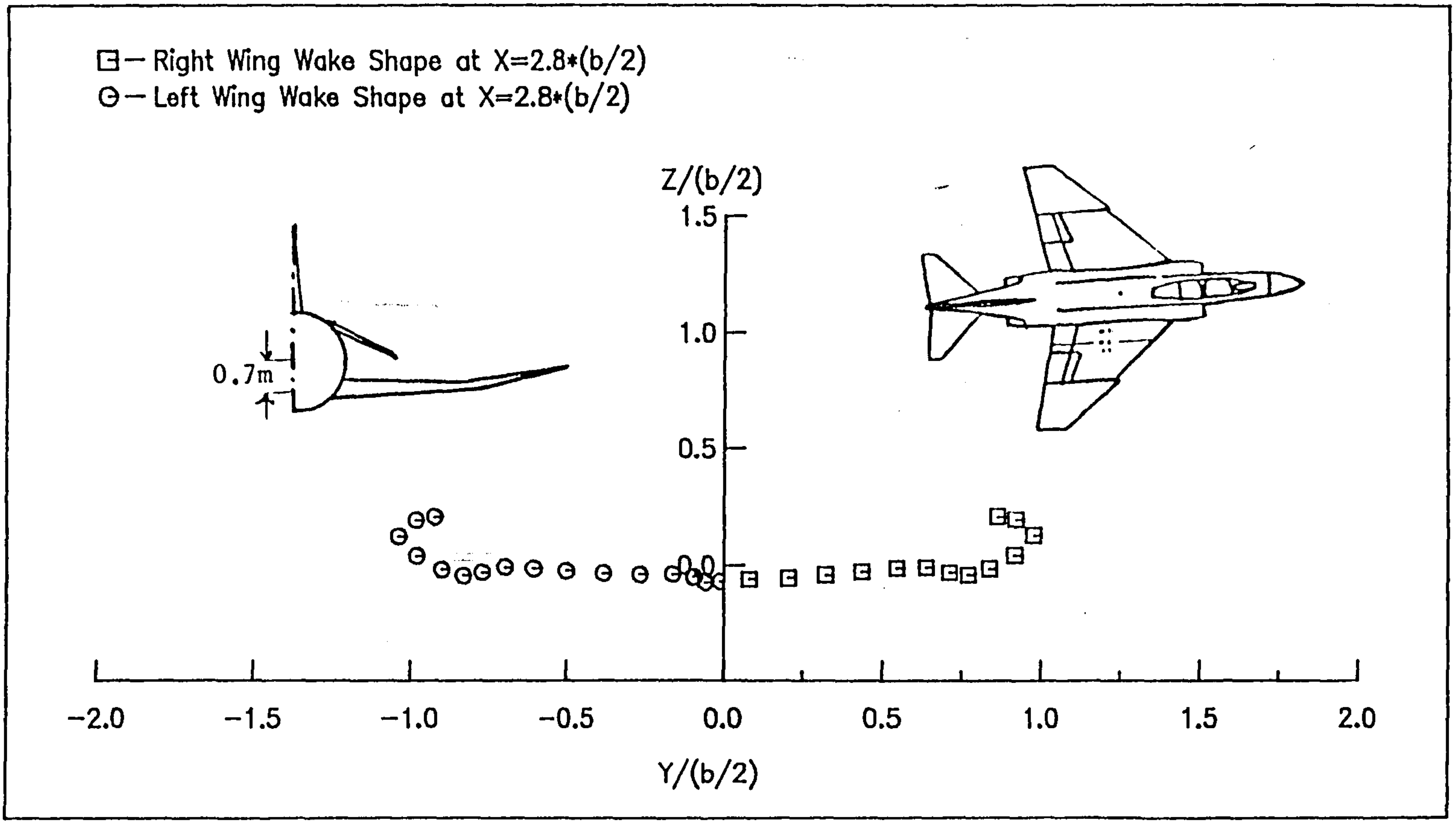

Fig. 8(d) The Wake Shape of a Wing_Body_Tail Configuration at Alpha = 20 and Beta = 5 deg.

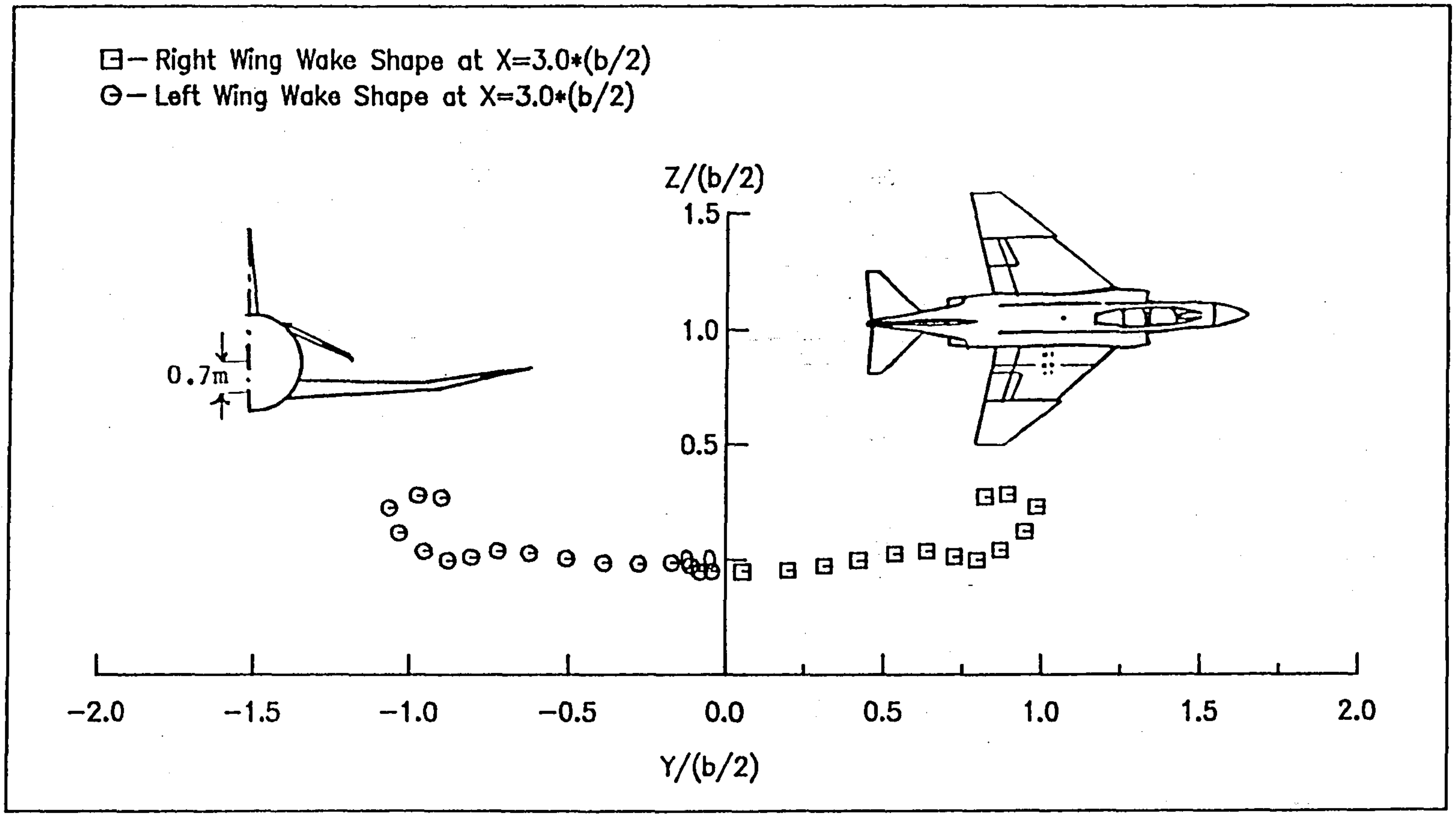

Fig. 8(e) The Wake Shape of a Wing_Body_Tail Configuration
at Alpha = 20 and Beta = 5 deg.

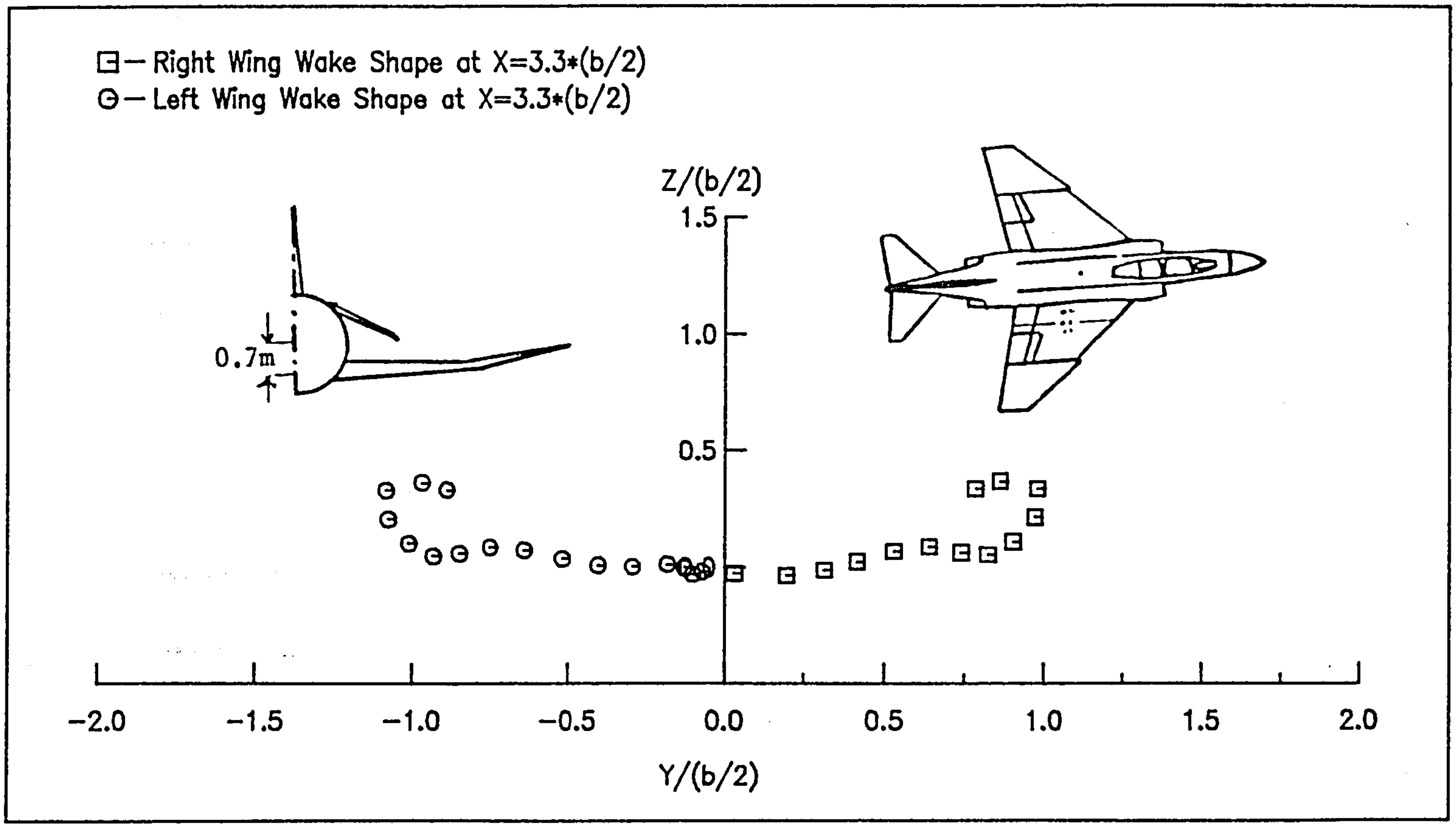

Fig. 8(f) The Wake Shape of a Wing_Body_Tail Configuration
at Alpha = 20 and Beta = 5 deg.

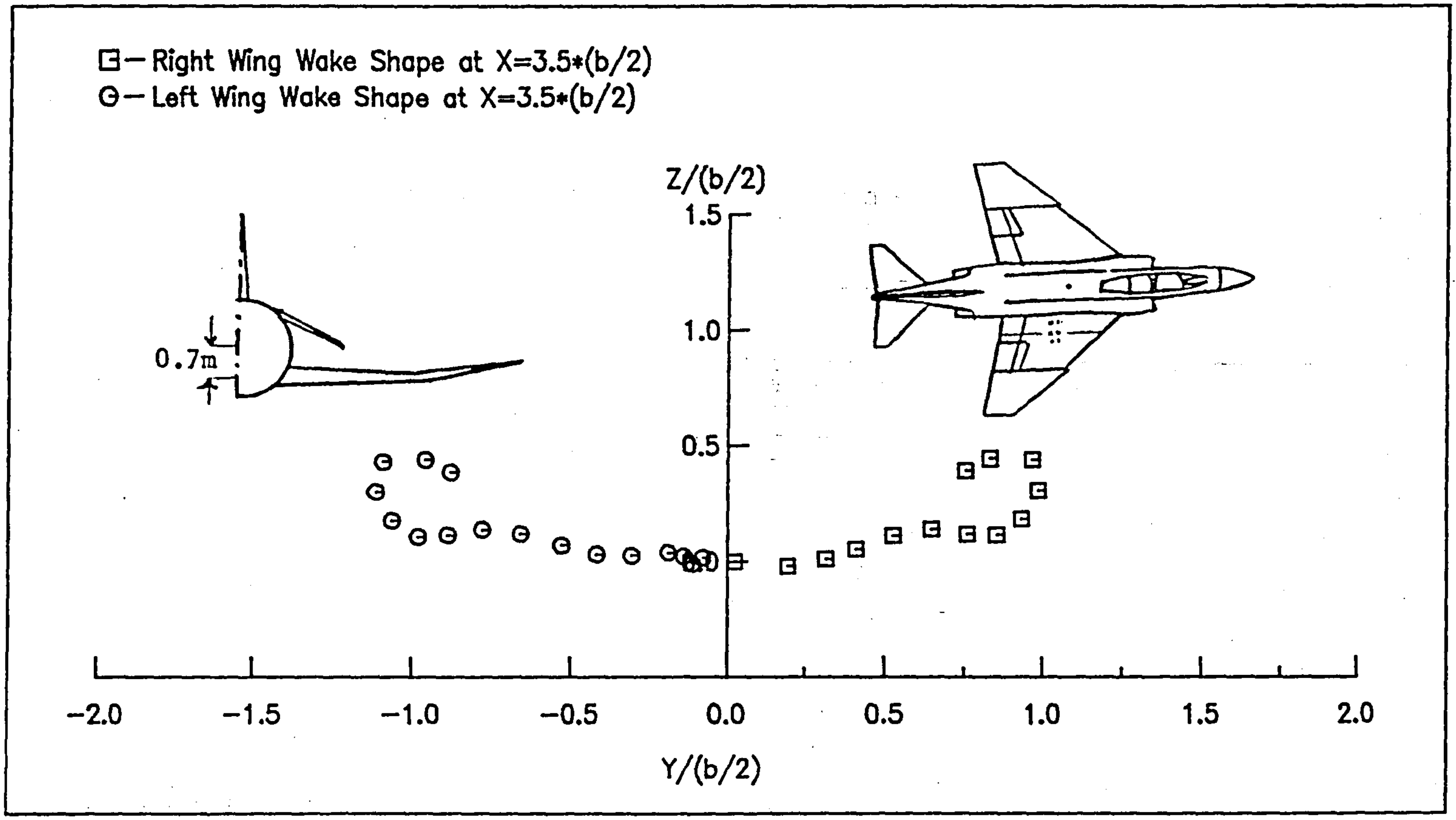

Fig. 8(g) The Wake Shape of a Wing_Body_Tail Configuration
at Alpha = 20 and Beta = 5 deg.

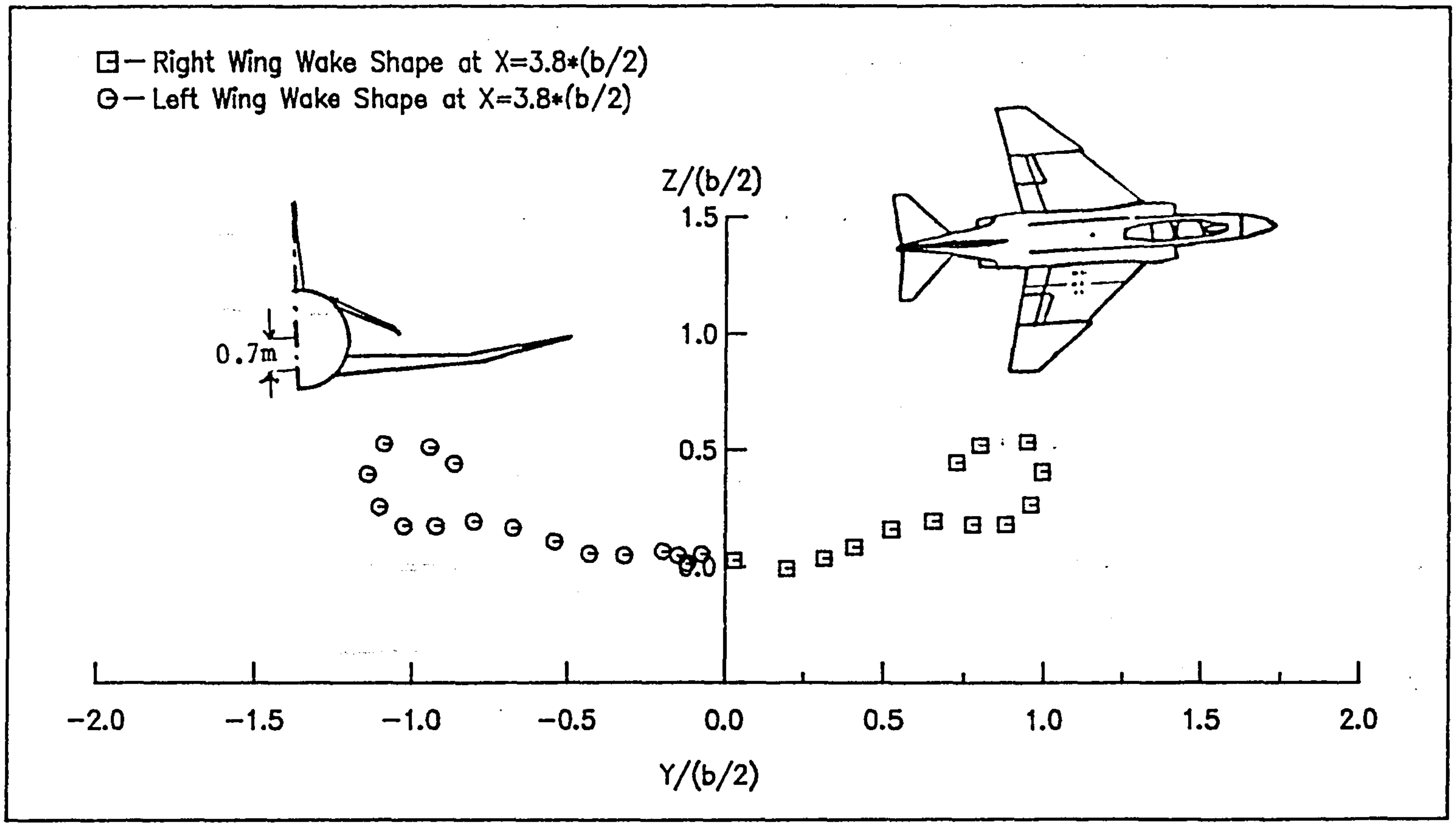

Fig. 8(h) The Wake Shape of a Wing_Body_Tail Configuration at Alpha = 20 and Beta = 5 deg.

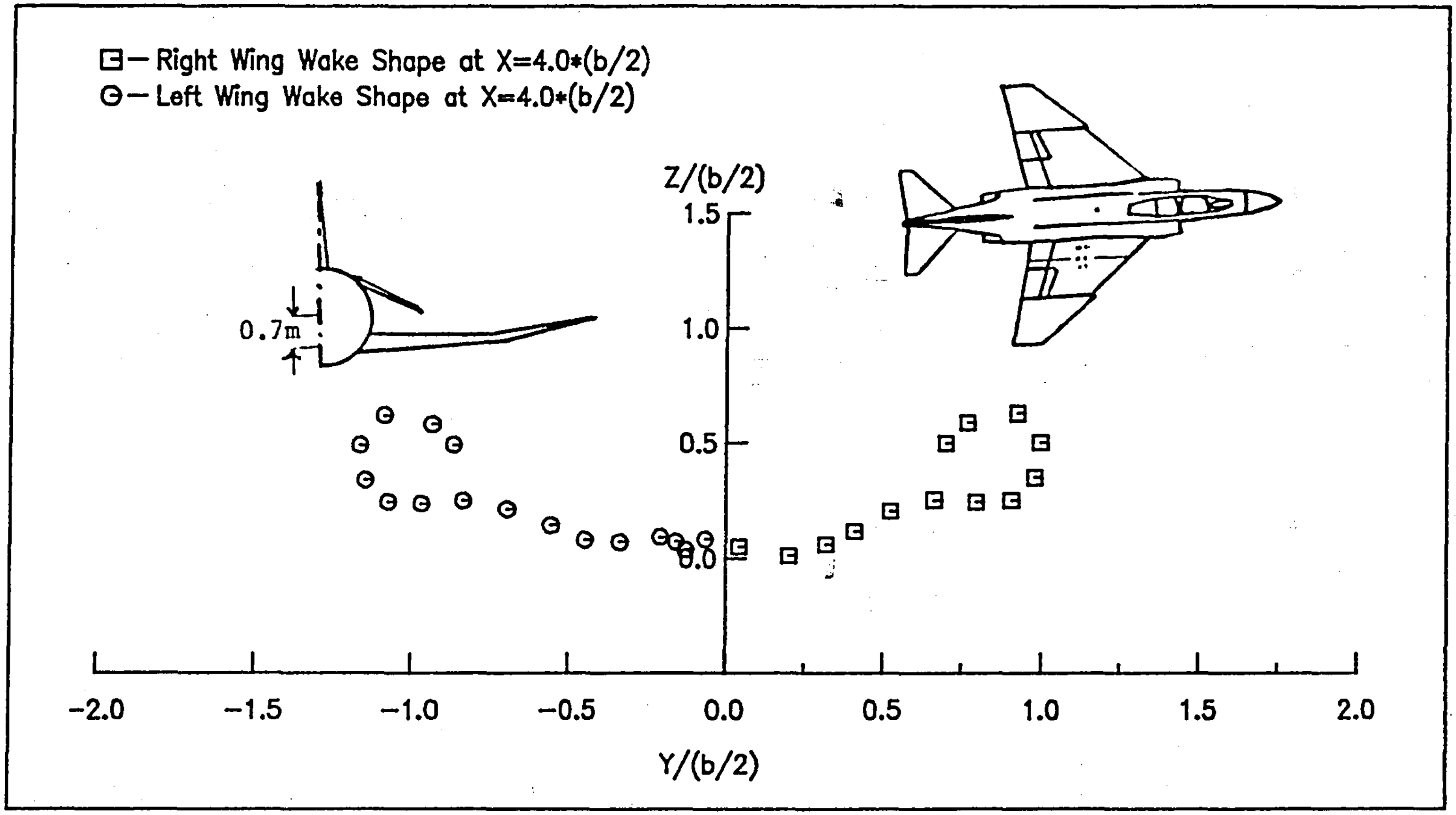

Fig. 8(i) The Wake Shape of a Wing_Body_Tail Configuration
at Alpha = 20 and Beta = 5 deg.

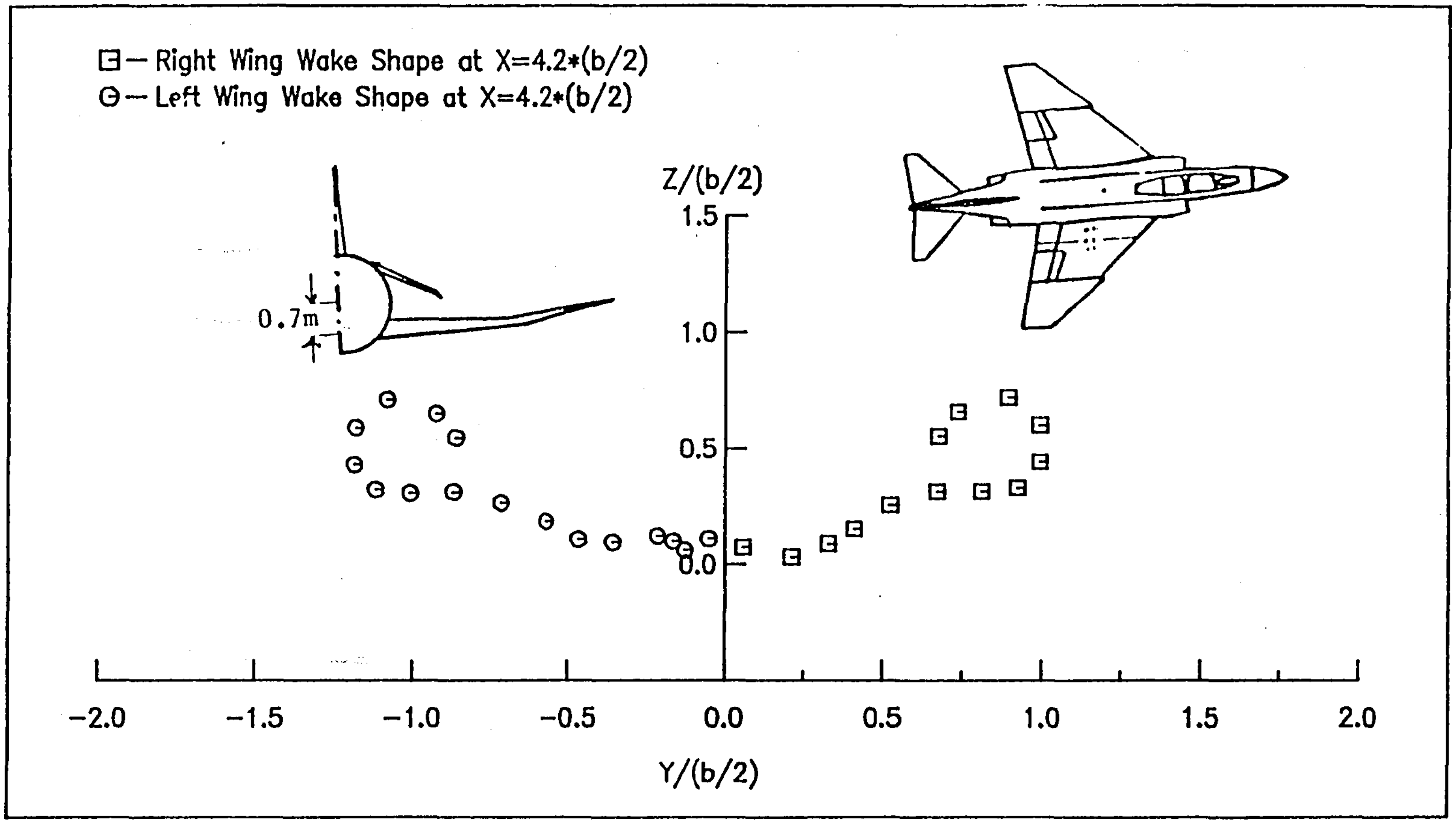

Fig. 8(j) The Wake Shape of a Wing_Body_Tail Configuration
at Alpha = 20 and Beta = 5 deg.

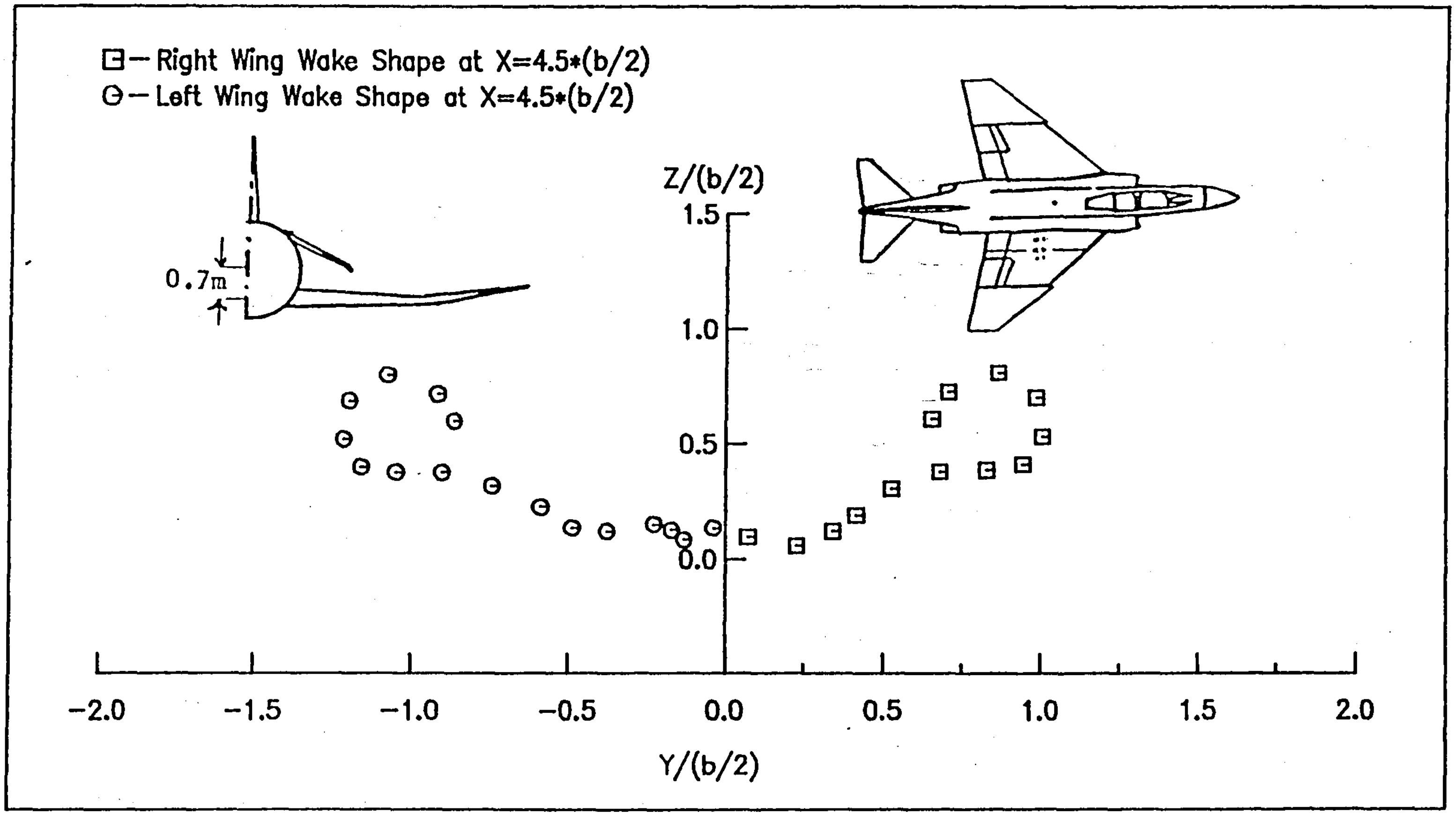

Fig. 8(k) The Wake Shape of a Wing_Body_Tail Configuration
at Alpha = 20 and Beta = 5 deg.

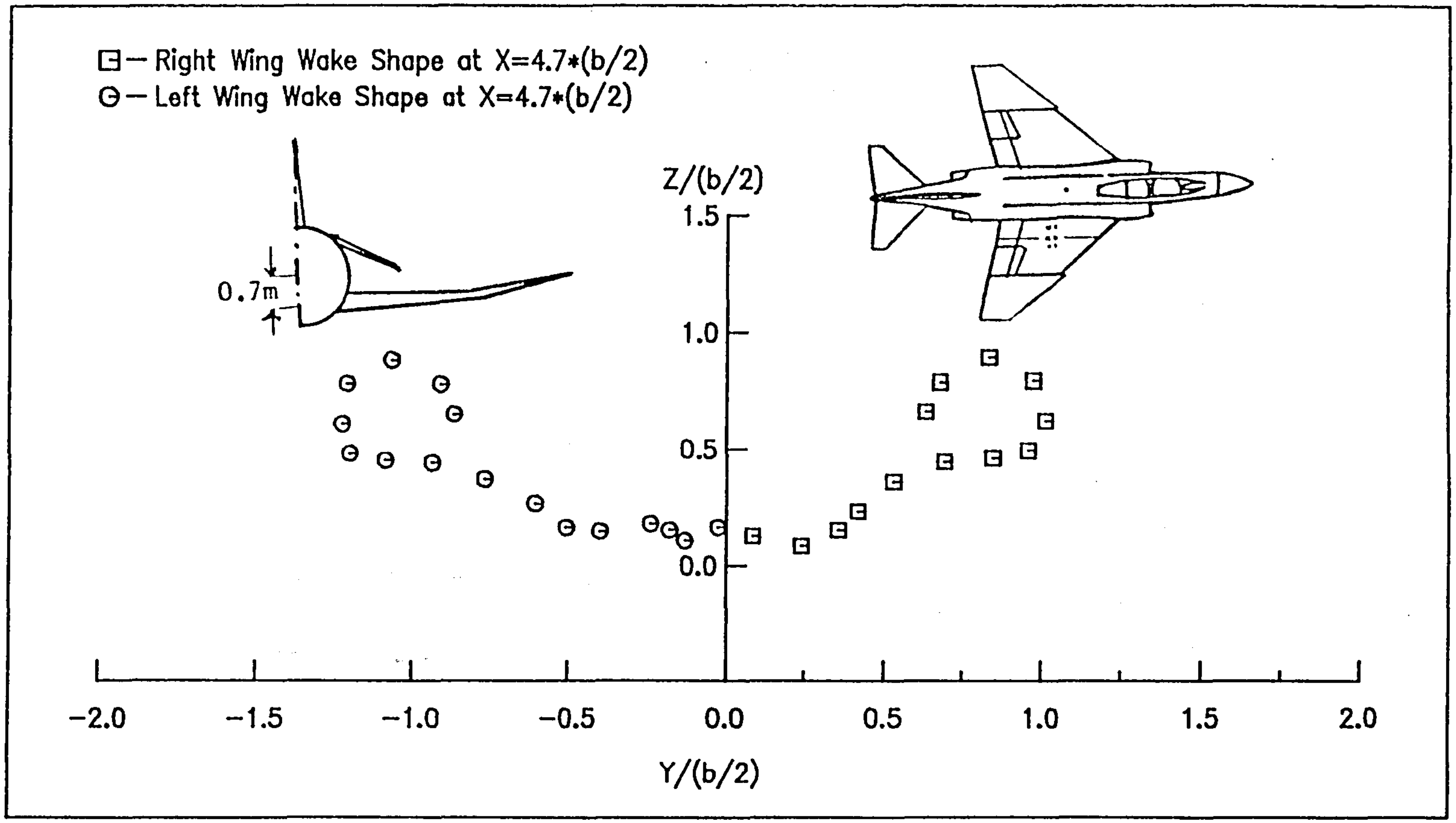

Fig. 8(l) The Wake Shape of a Wing_Body_Tail Configuration at Alpha = 20 and Beta = 5 deg.

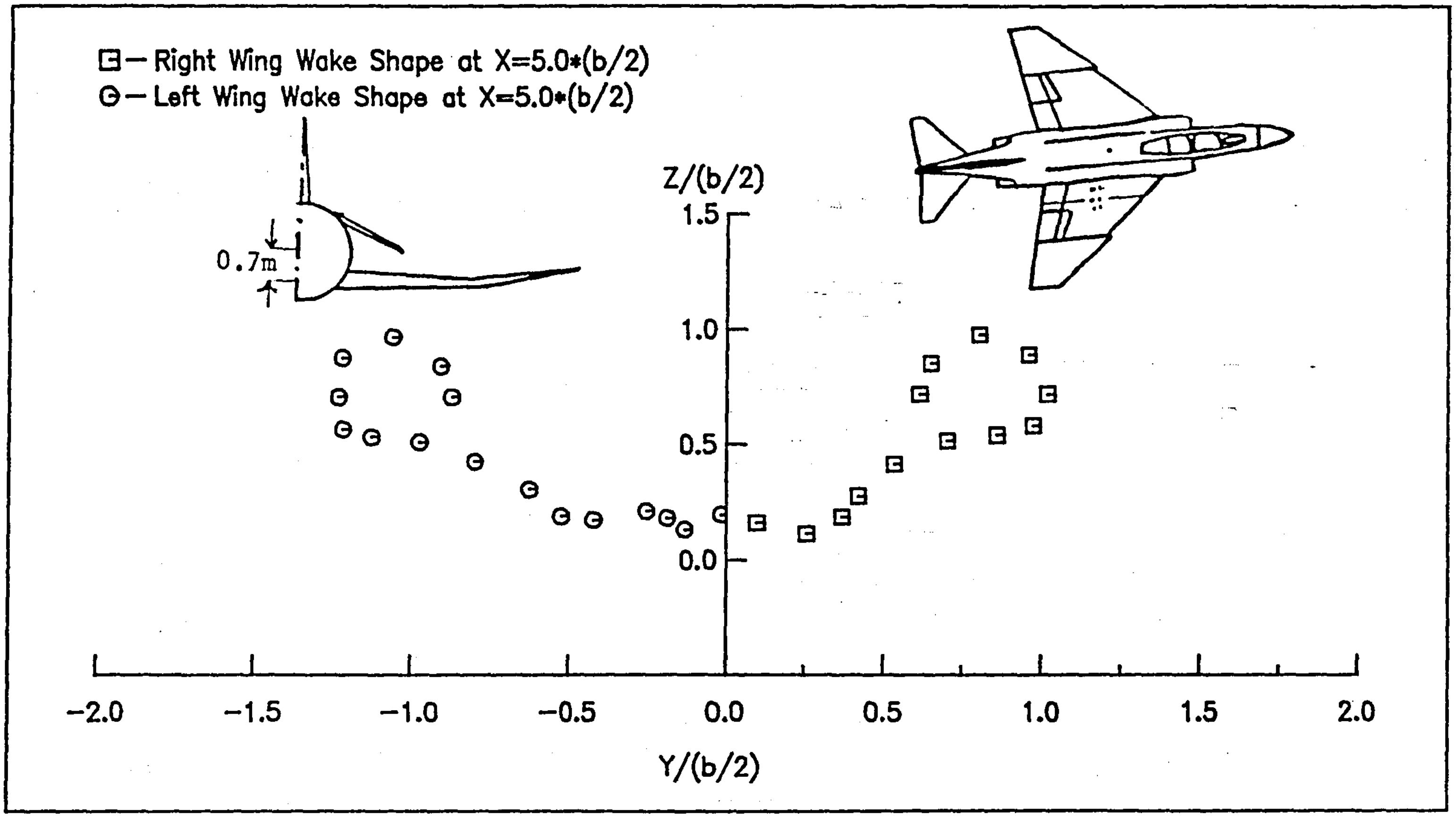

Fig. 8(m) The Wake Shape of a Wing_Body_Tail Configuration
at Alpha = 20 and Beta = 5 deg.

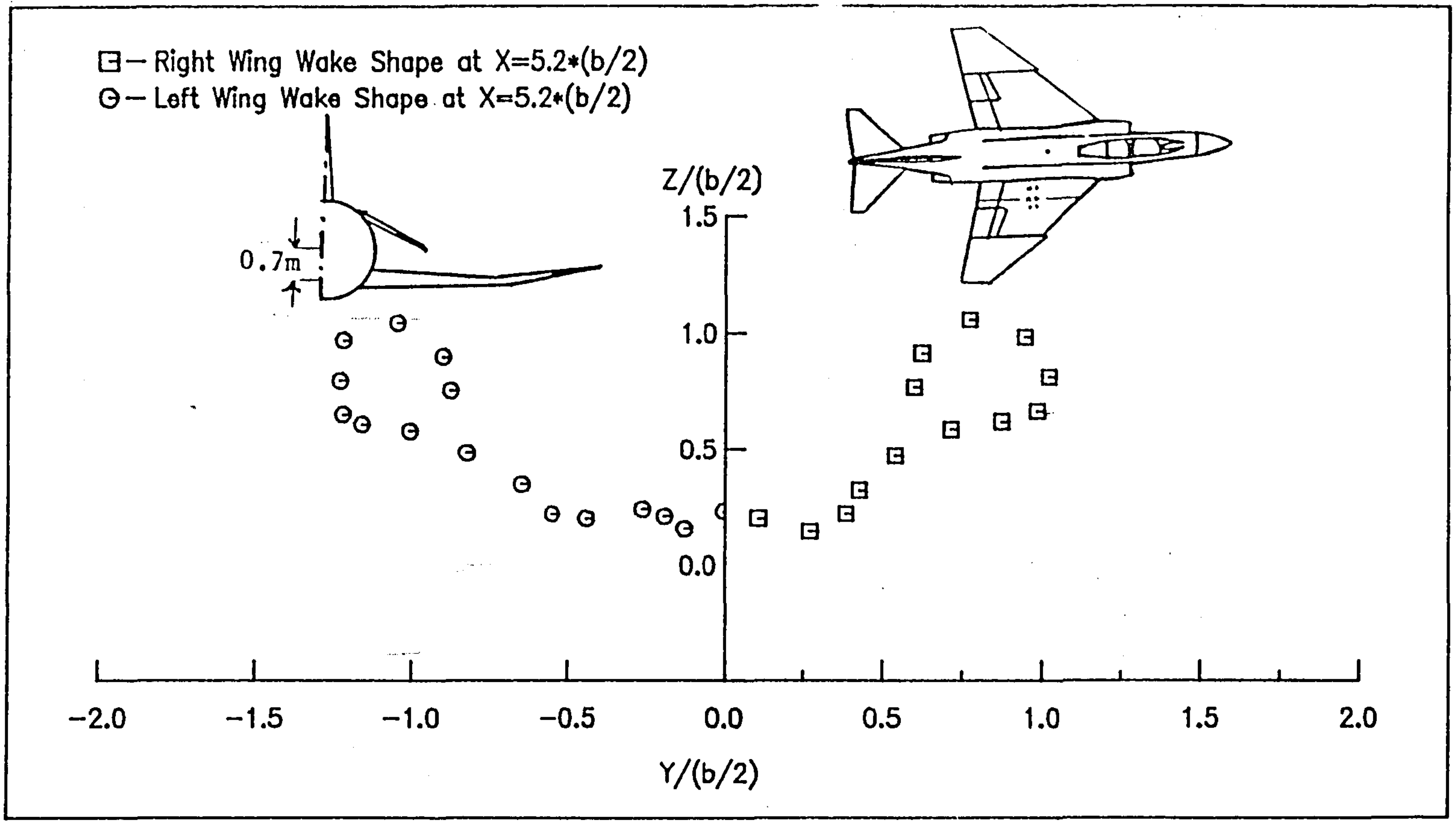

Fig. 8(n) The Wake Shape of a Wing_Body_Tail Configuration at Alpha = 20 and Beta = 5 deg.

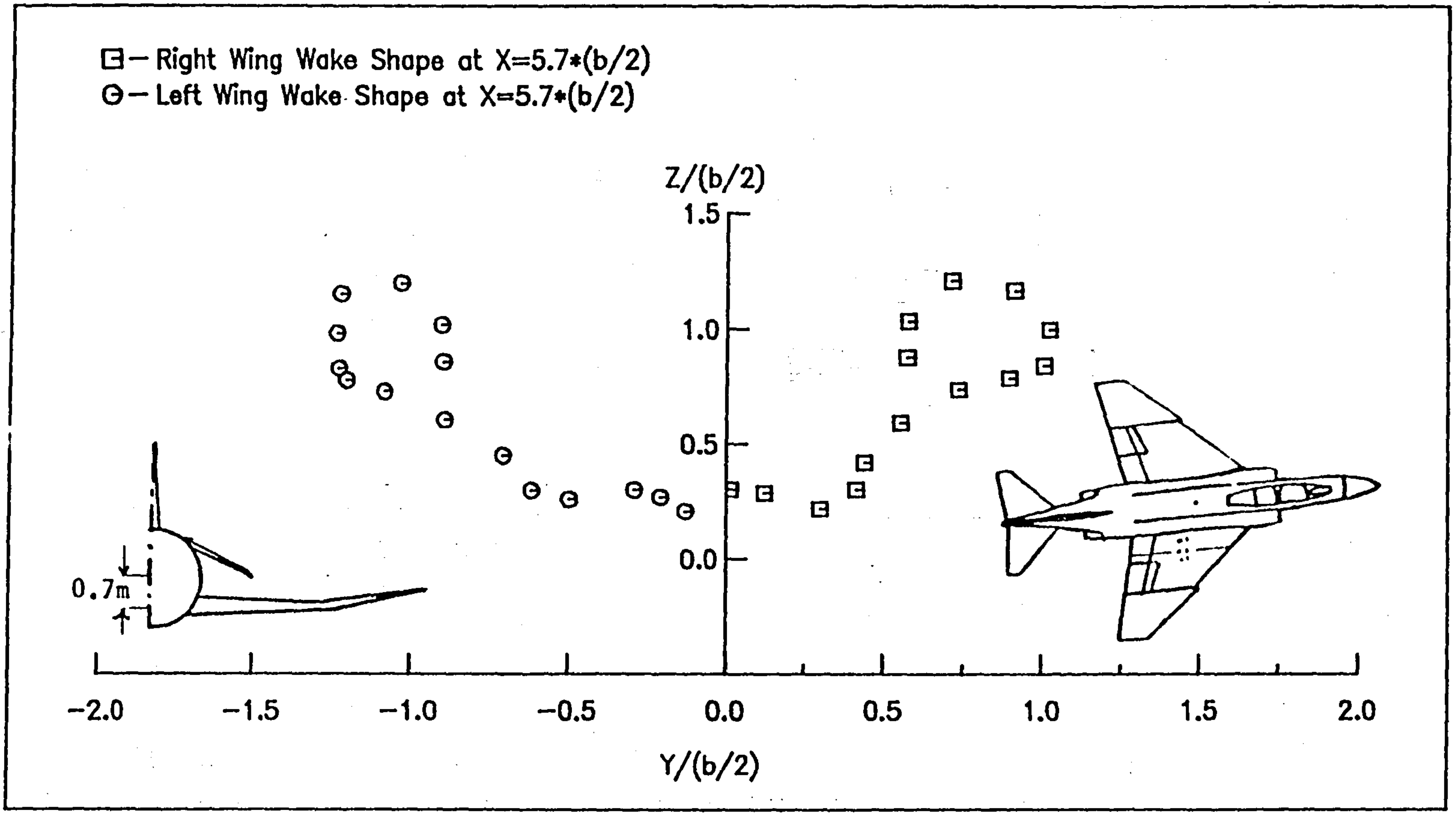

Fig. 8(o) The Wake Shape of a Wing_Body_Tail Configuration
at Alpha = 20 and Beta = 5 deg.

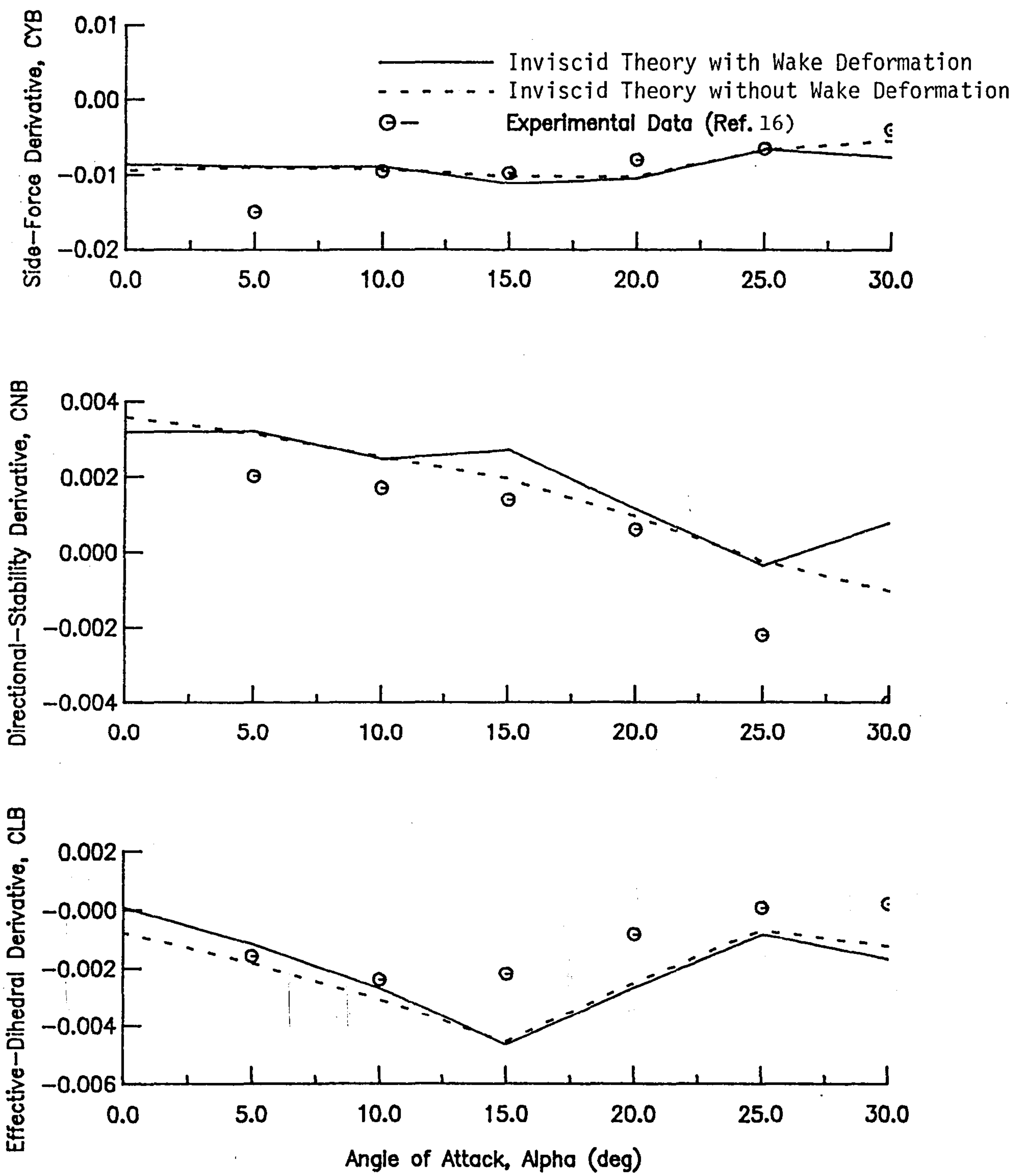

Fig. 9(a) Static Lateral-Directional Stability Derivatives of a Wing_Body_Tail Configuration

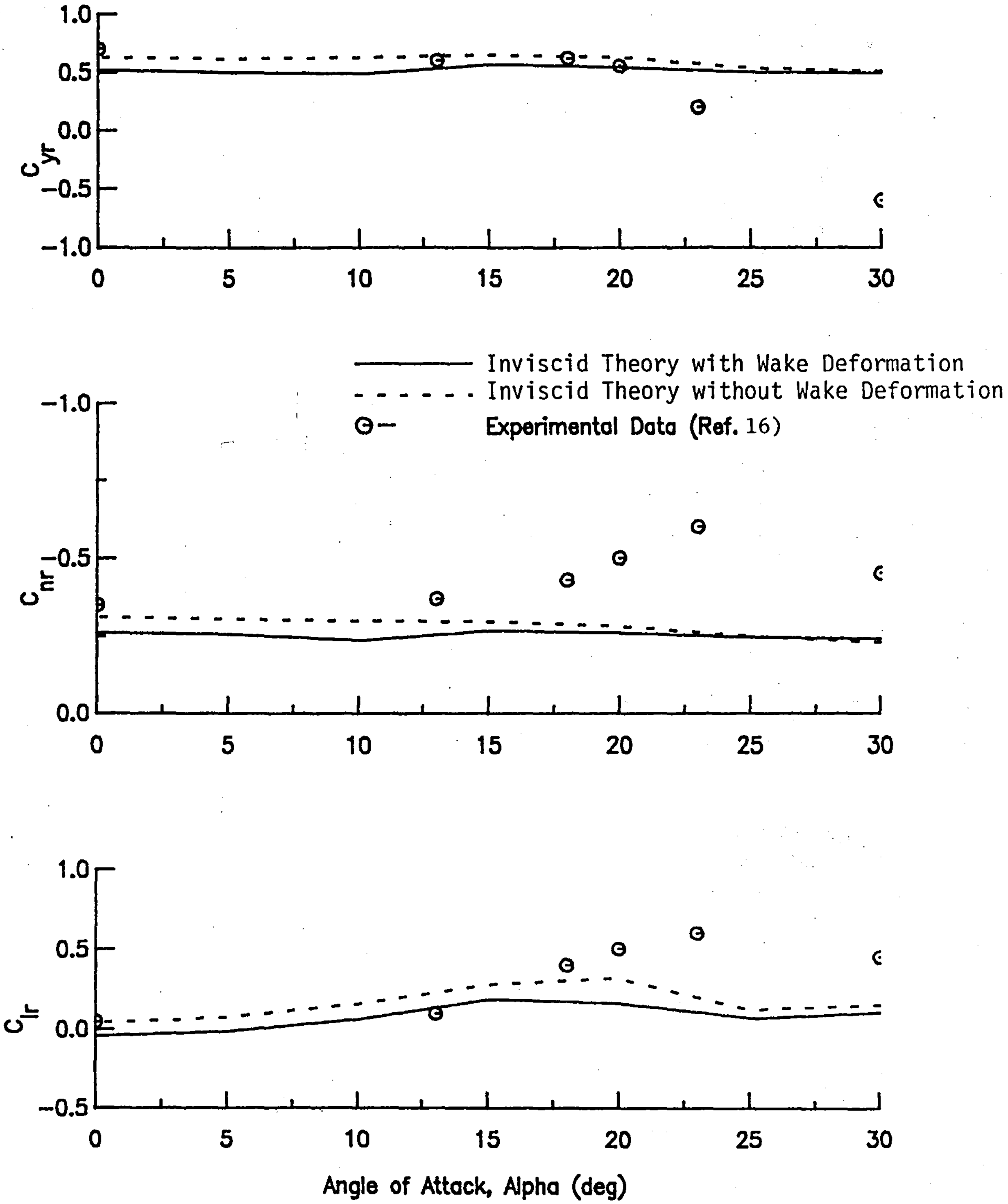

Fig. 9(b) Static Lateral–Directional Stability Derivatives of a Wing_Body_Tail Configuration

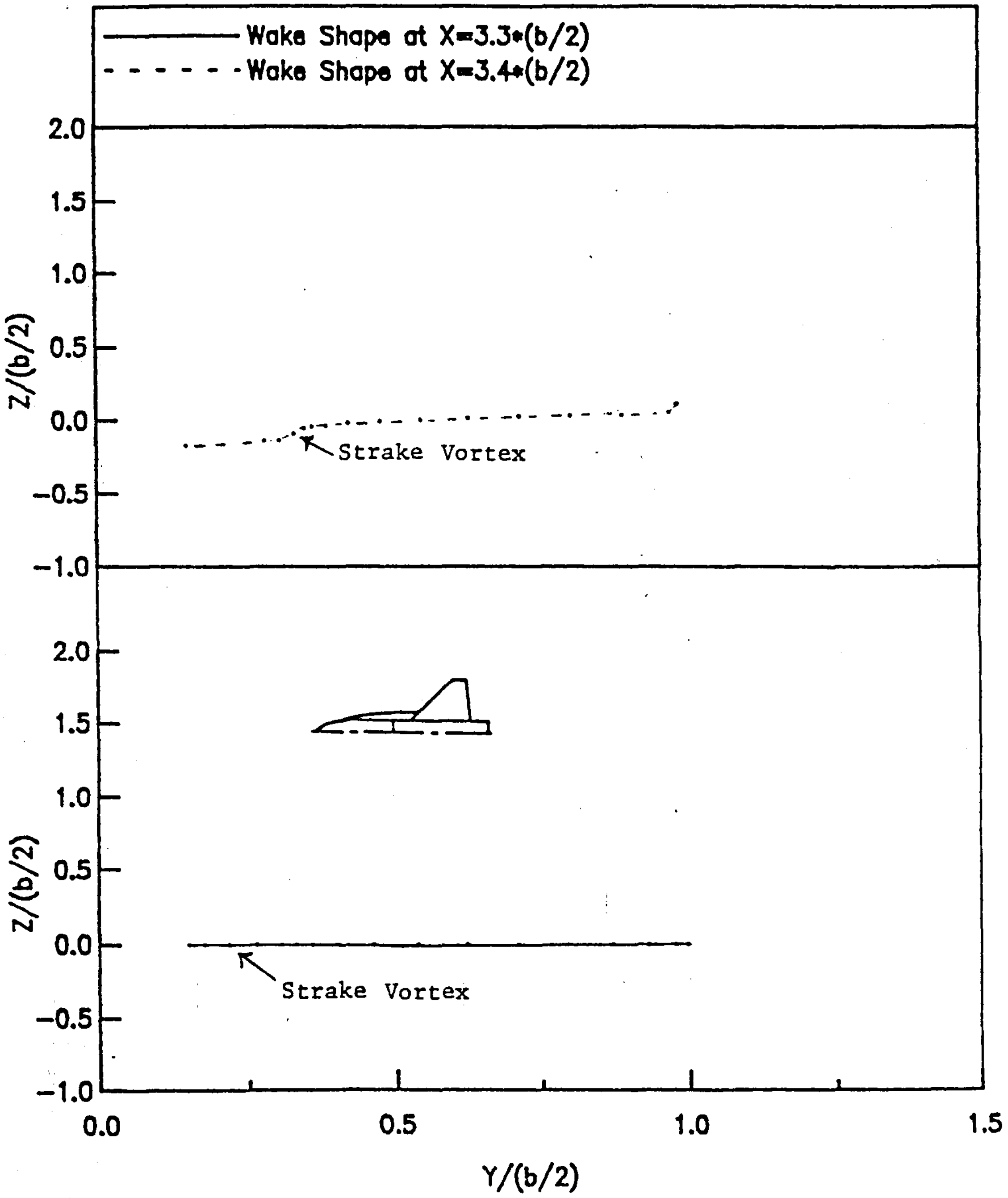

Fig. 10(a) Wake Shape of the Straked Wing-Body Configuration at Alpha = 29. deg.

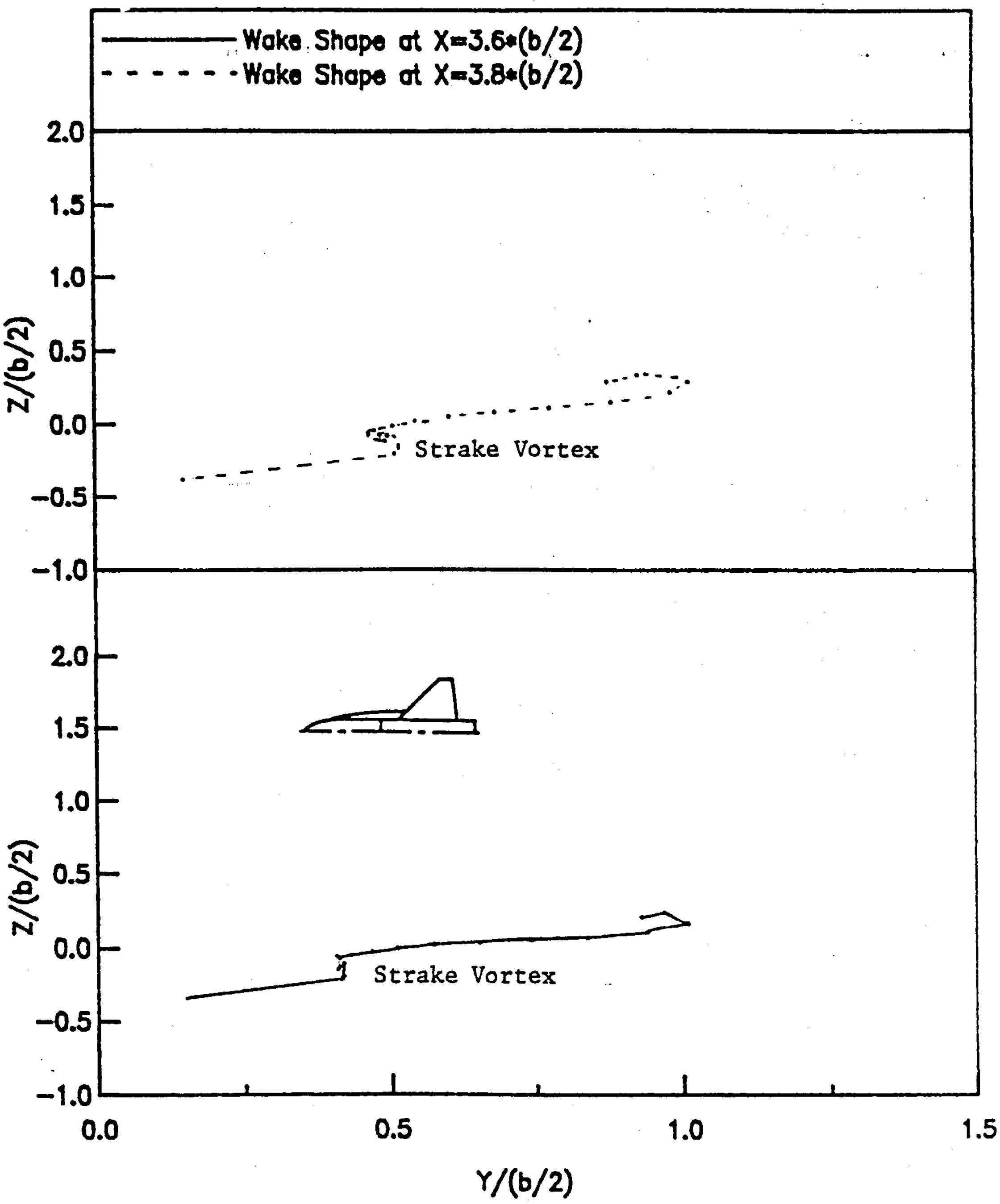

Fig. 10(b) Wake Shape of the Straked Wing-Body Configuration at Alpha = 29. deg.

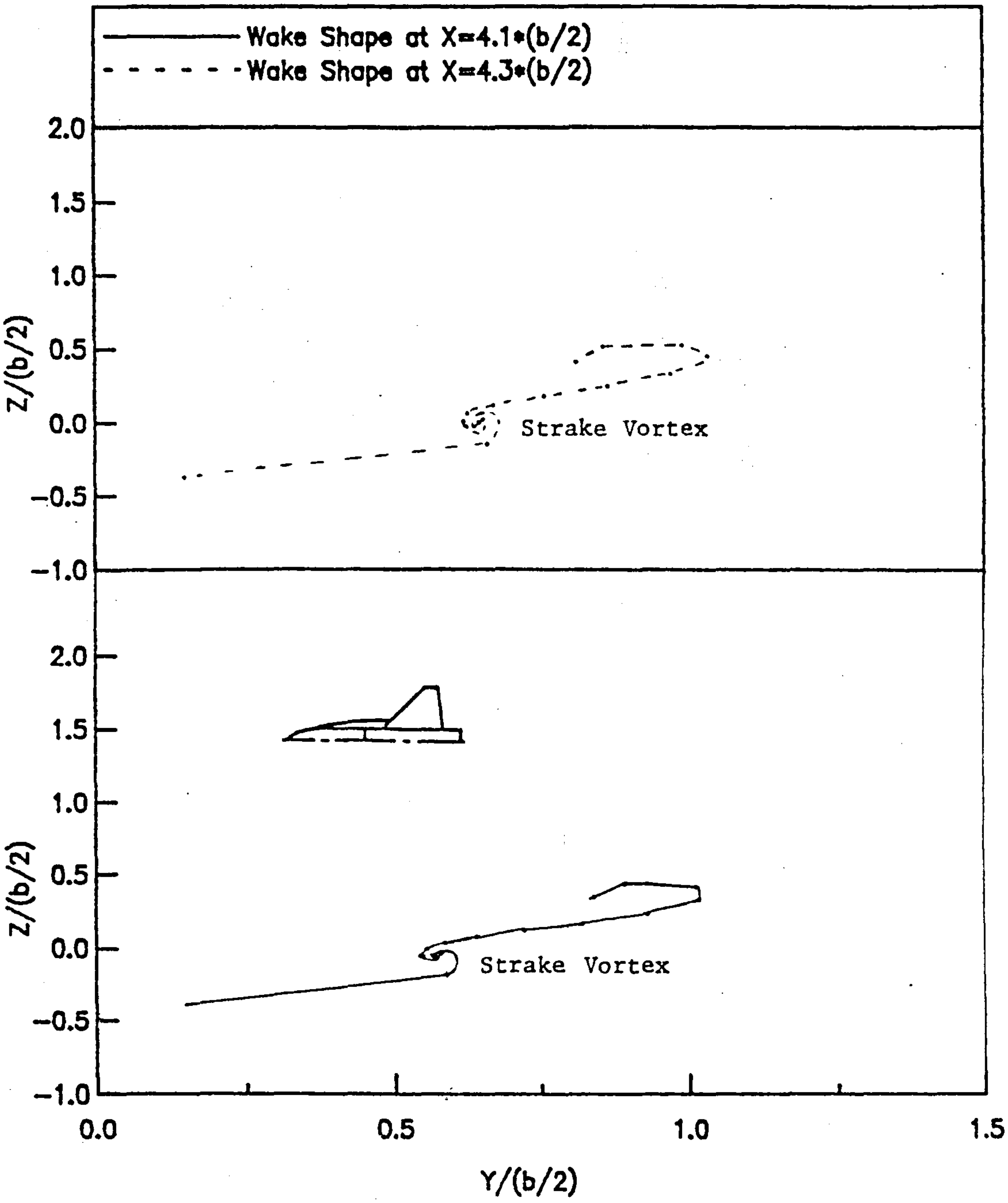

Fig. 10(c) Wake Shape of the Straked Wing-Body Configuration at Alpha = 29. deg.

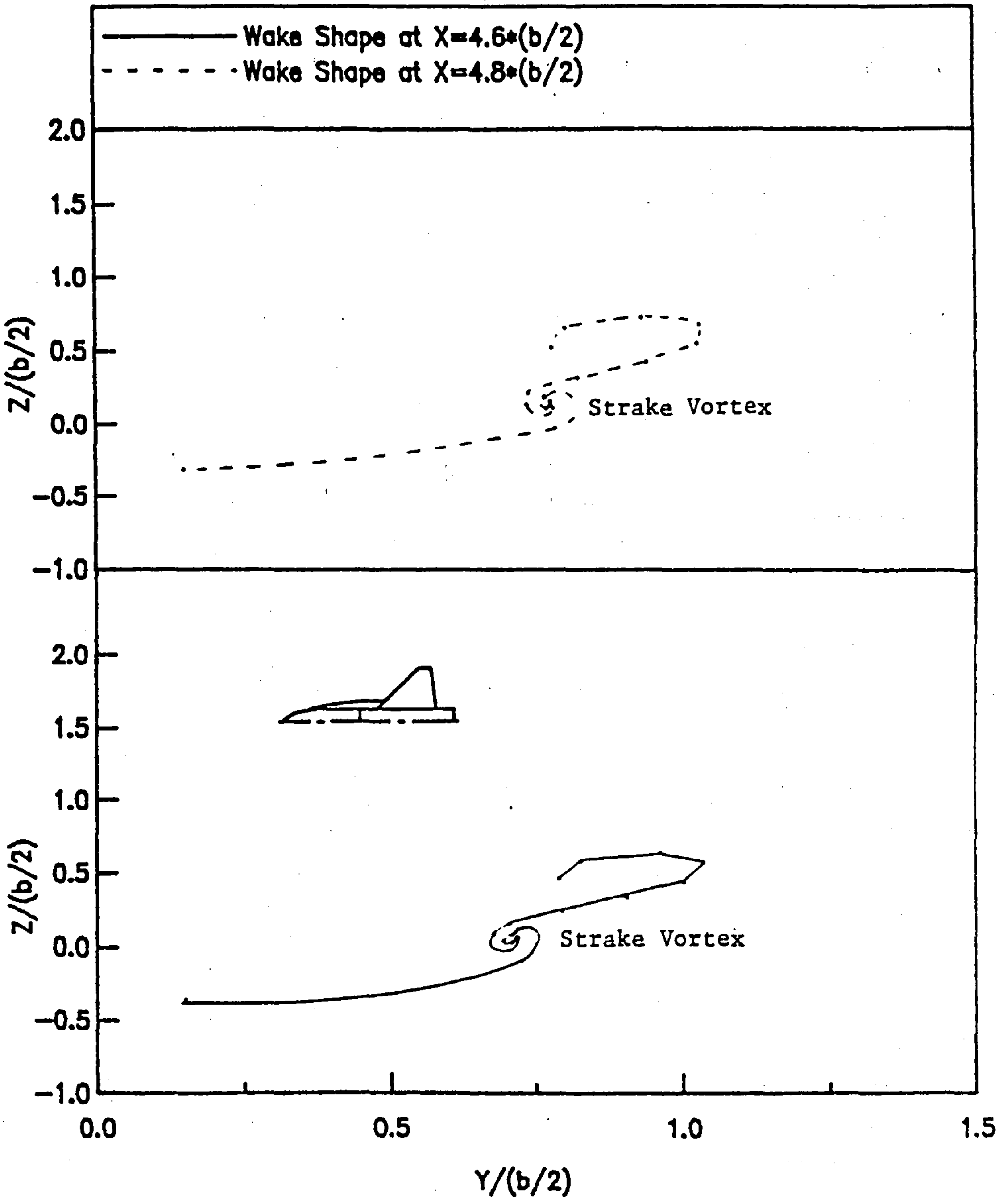

Fig. 10(d) Wake Shape of the Straked Wing-Body Configuration at Alpha = 29. deg.

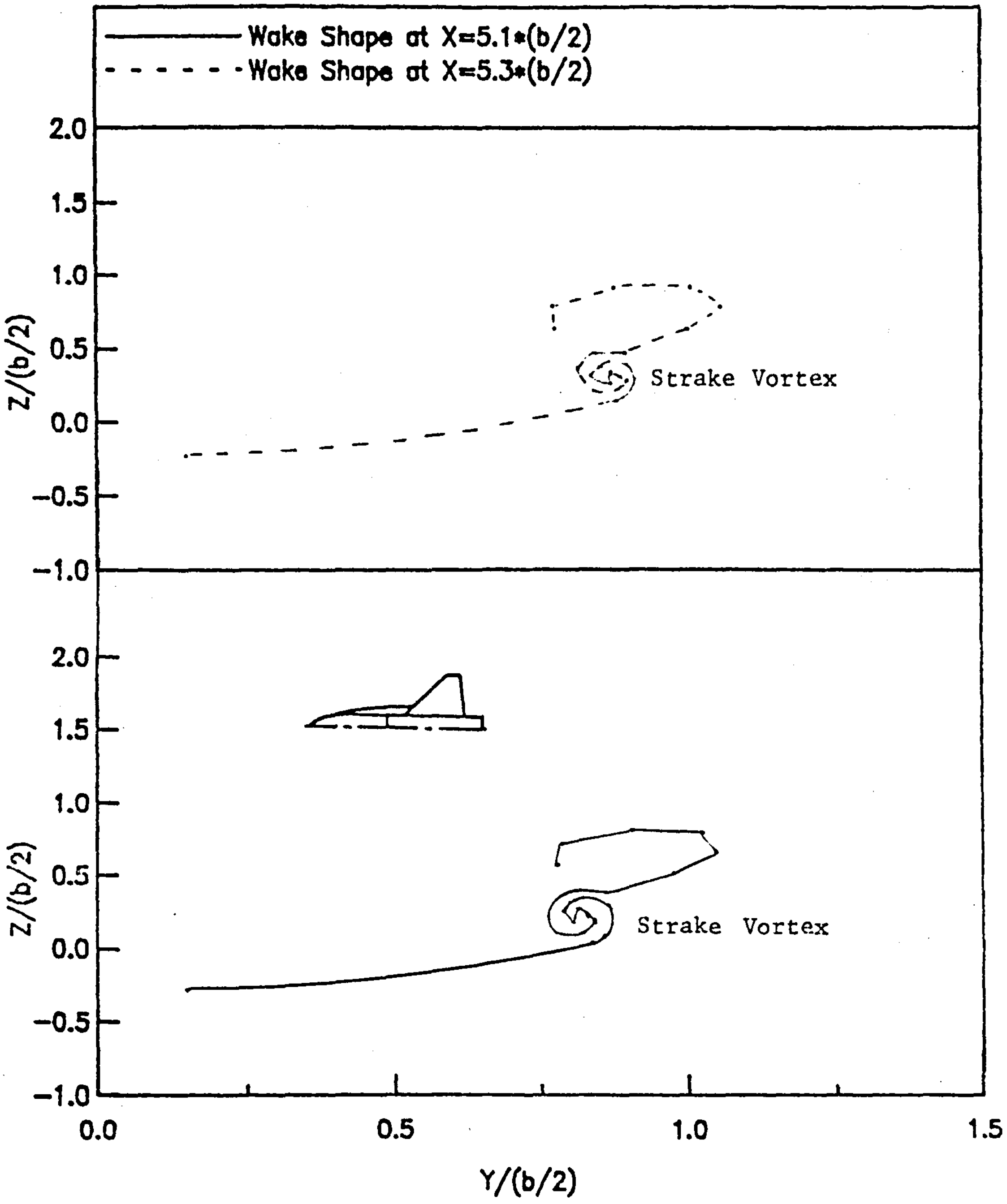

Fig. 10(e) Wake Shape of the Straked Wing-Body Configuration at Alpha = 29. deg.

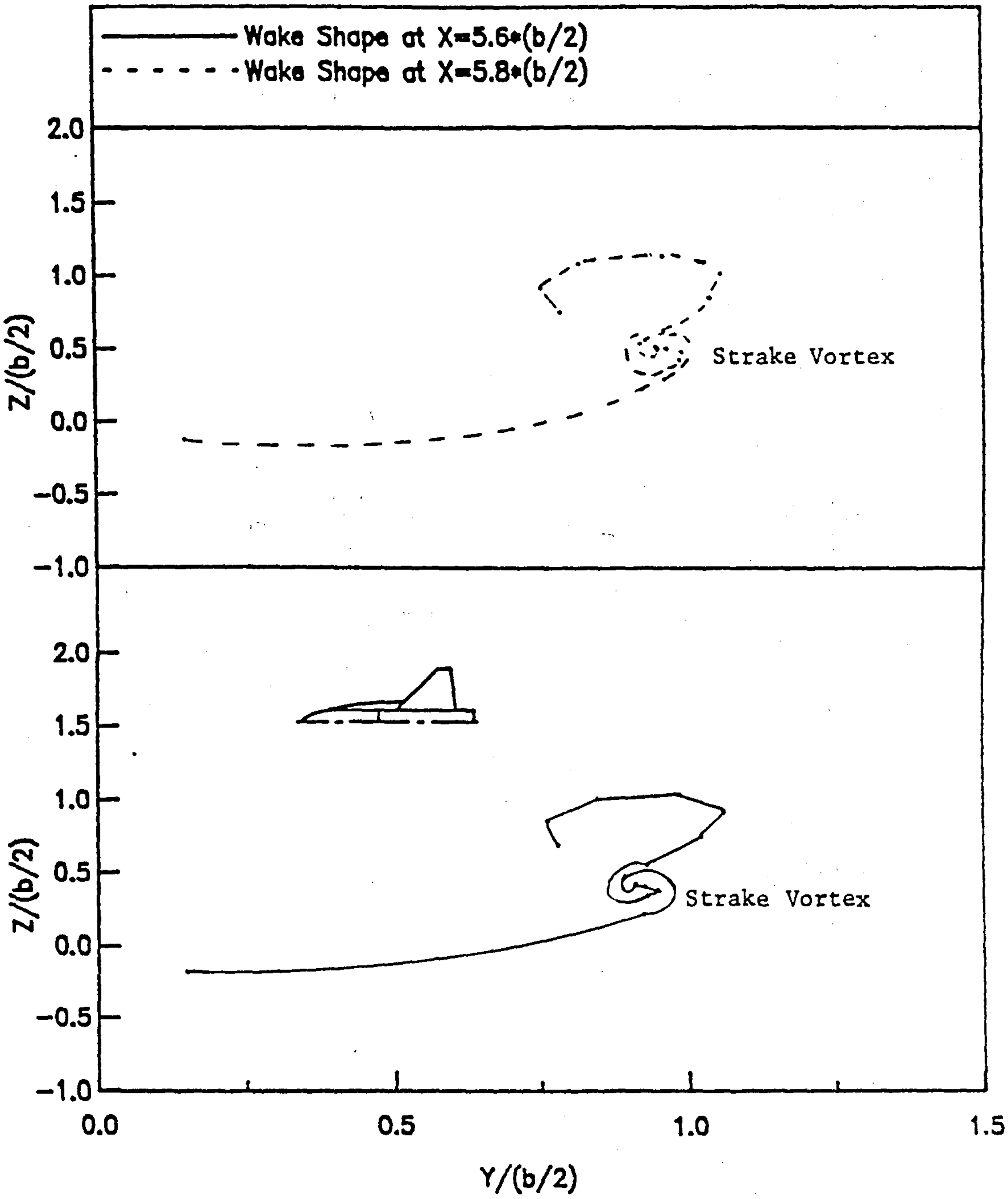

Fig. 10(f) Wake Shape of the Straked Wing-Body Configuration at Alpha = 29. deg.

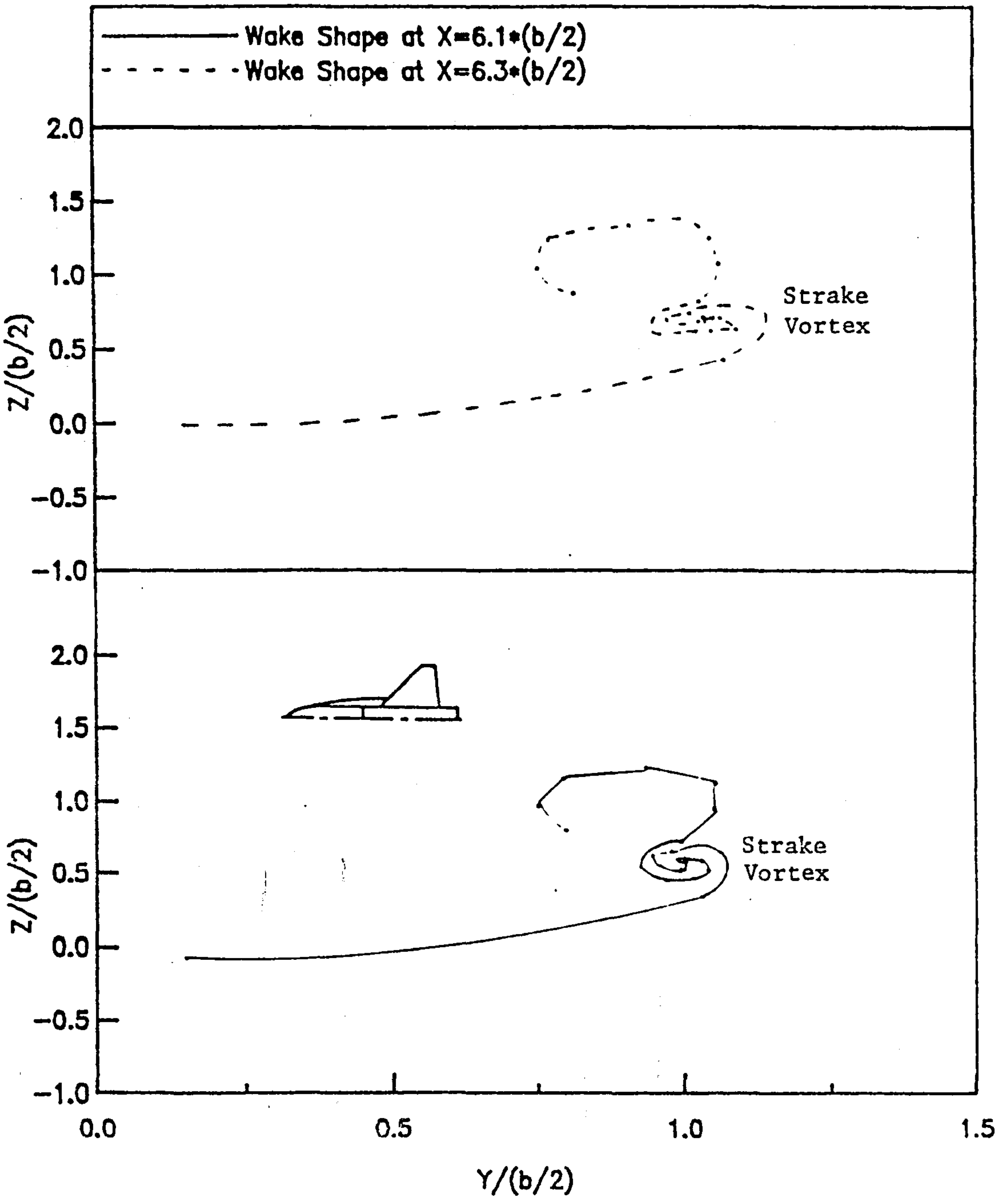

Fig. 10(g) Wake Shape of the Straked Wing-Body Configuration at Alpha = 29. deg.

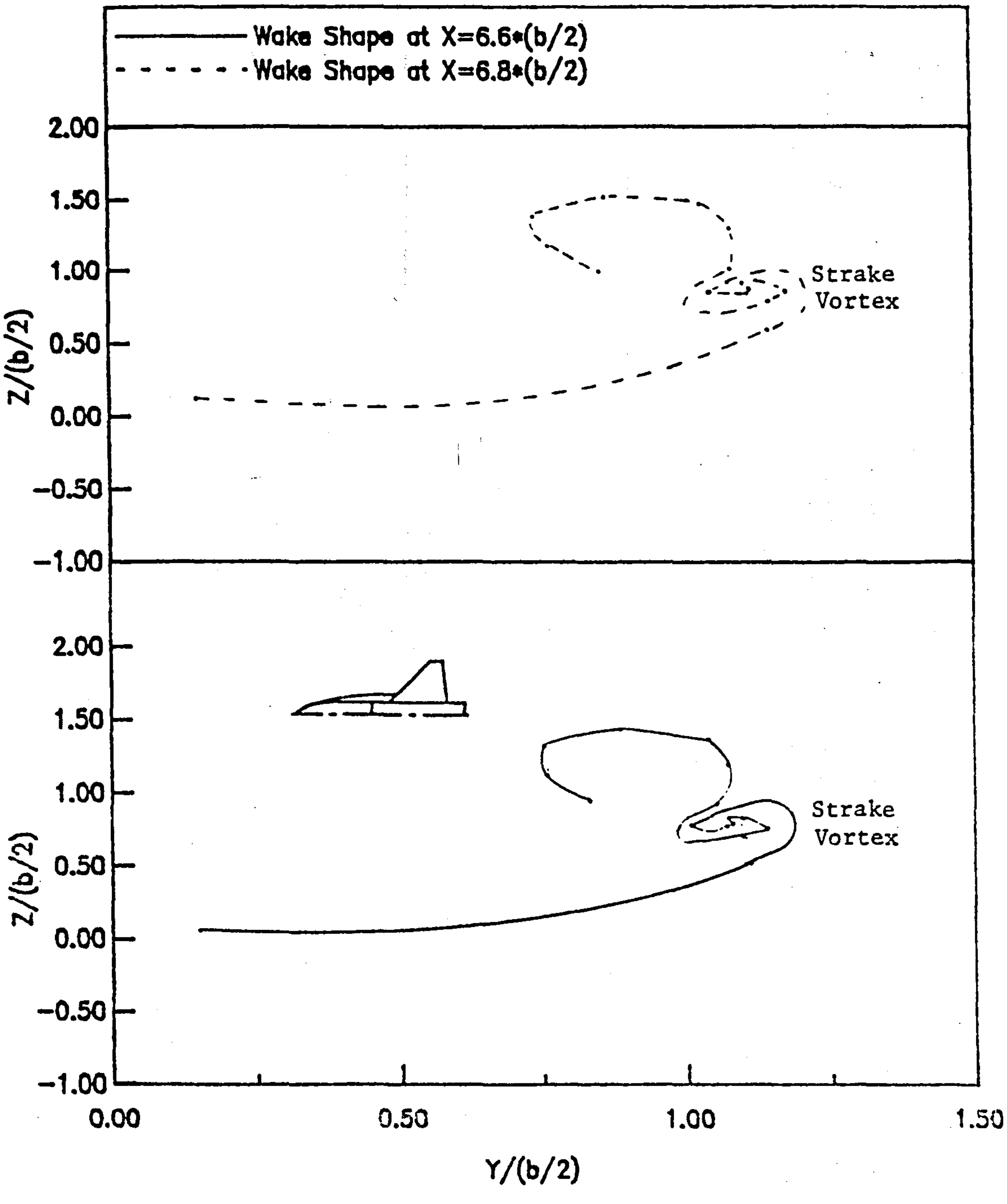

Fig. 10(h) Wake Shape of the Straked Wing-Body Configuration at Alpha = 29. deg.

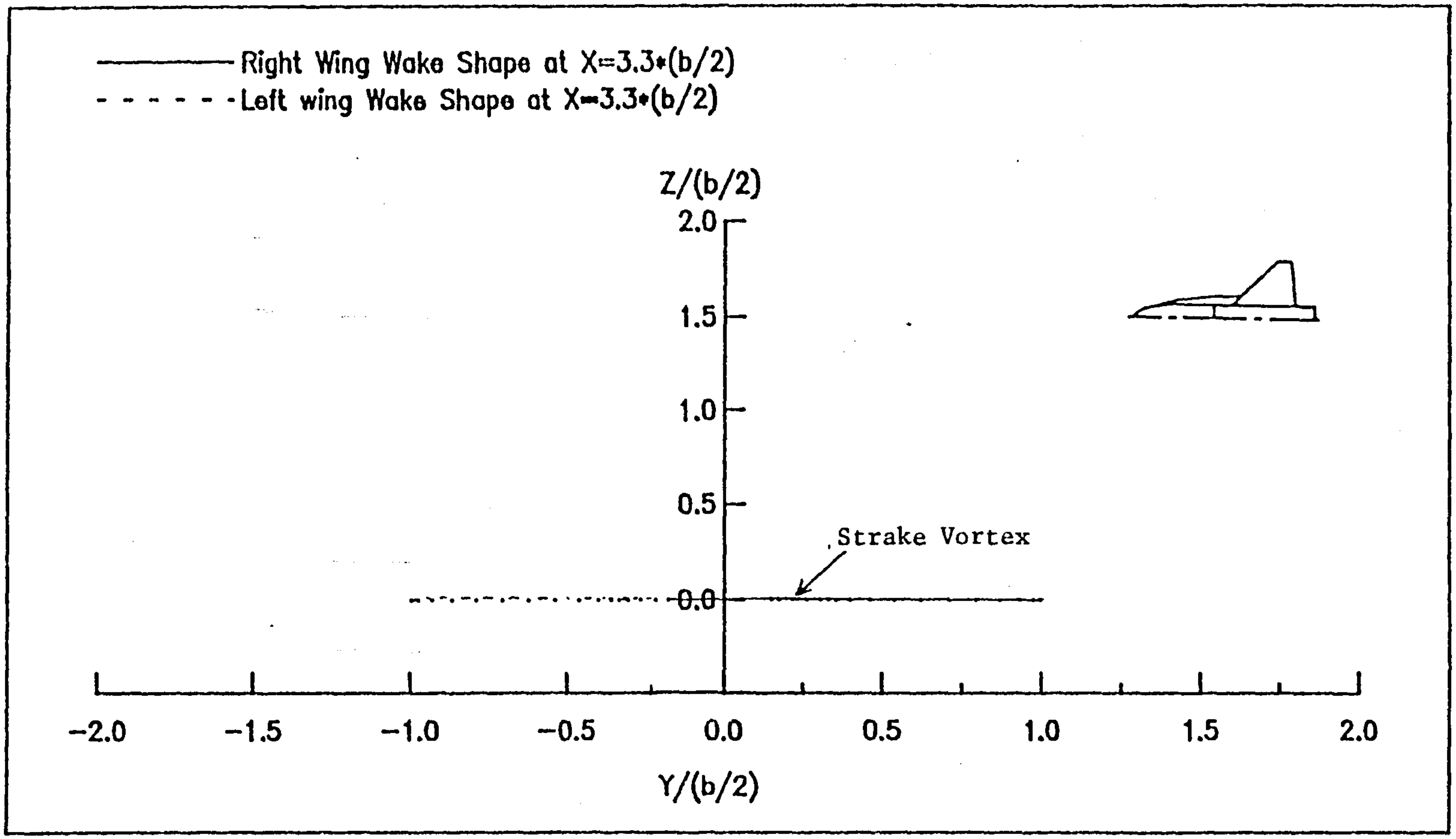

Fig. 11(a) Wake Shape of the Straked Wing-Body Configuration

at Alpha = 29 and Beta = 17 deg.

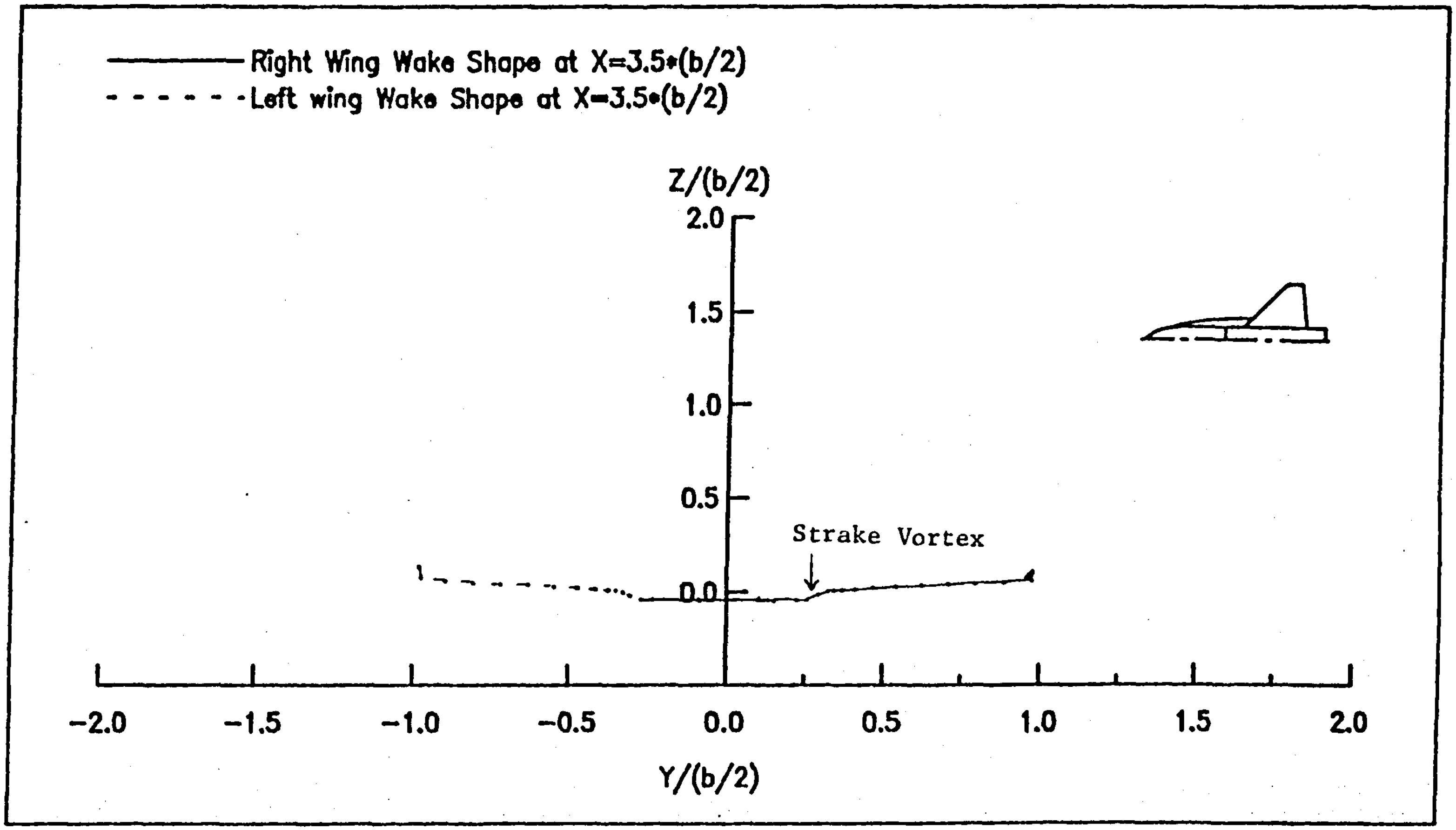

Fig. 11(b) Wake Shape of the Straked Wing-Body Configuration at Alpha = 29 and Beta = 17 deg.

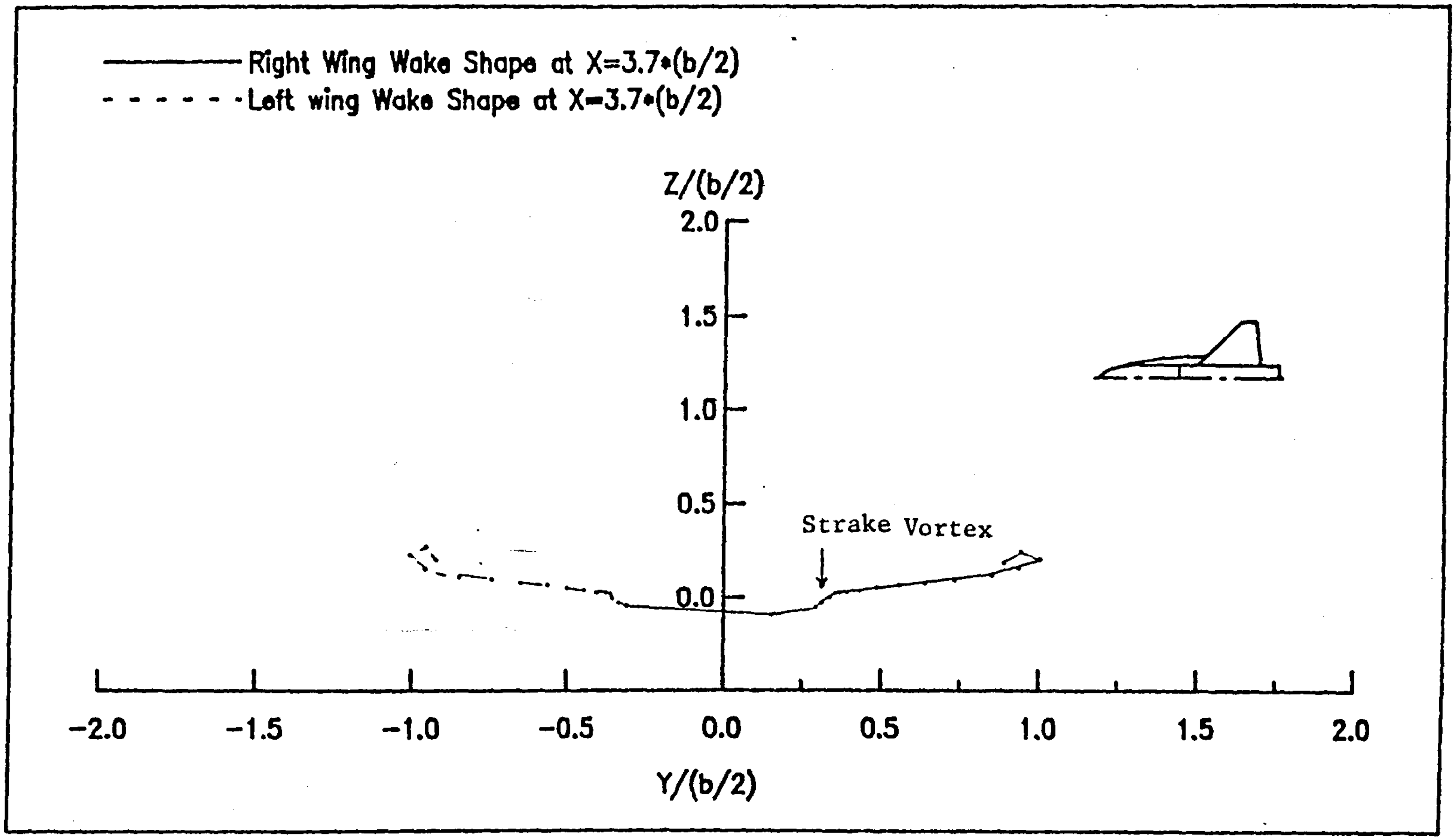

Fig. 11(c) Wake Shape of the Straked Wing-Body Configuration at Alpha = 29 and Beta = 17 deg.

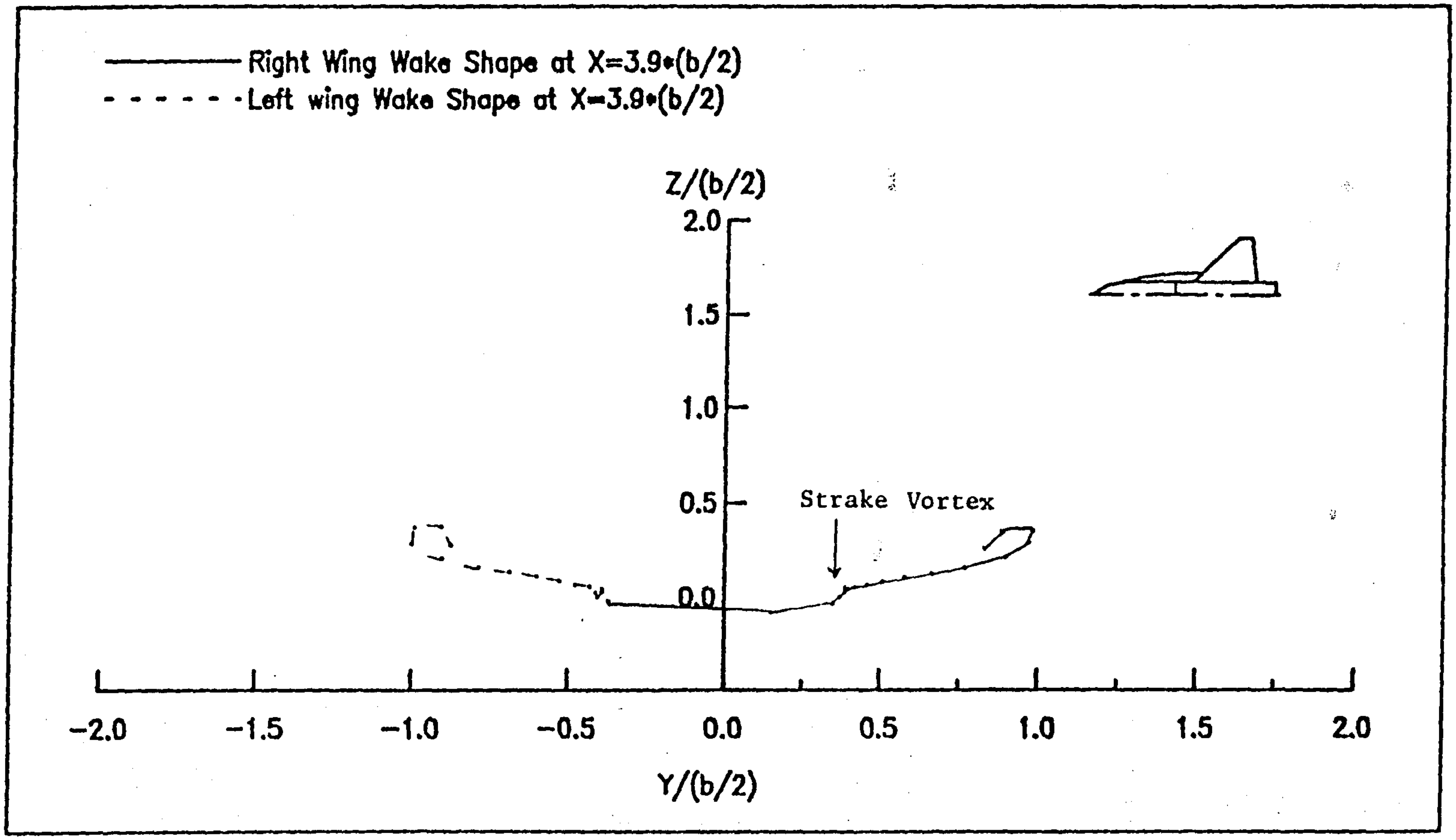

Fig. 11(d) Wake Shape of the Straked Wing-Body Configuration

at Alpha = 29 and Beta = 17 deg.

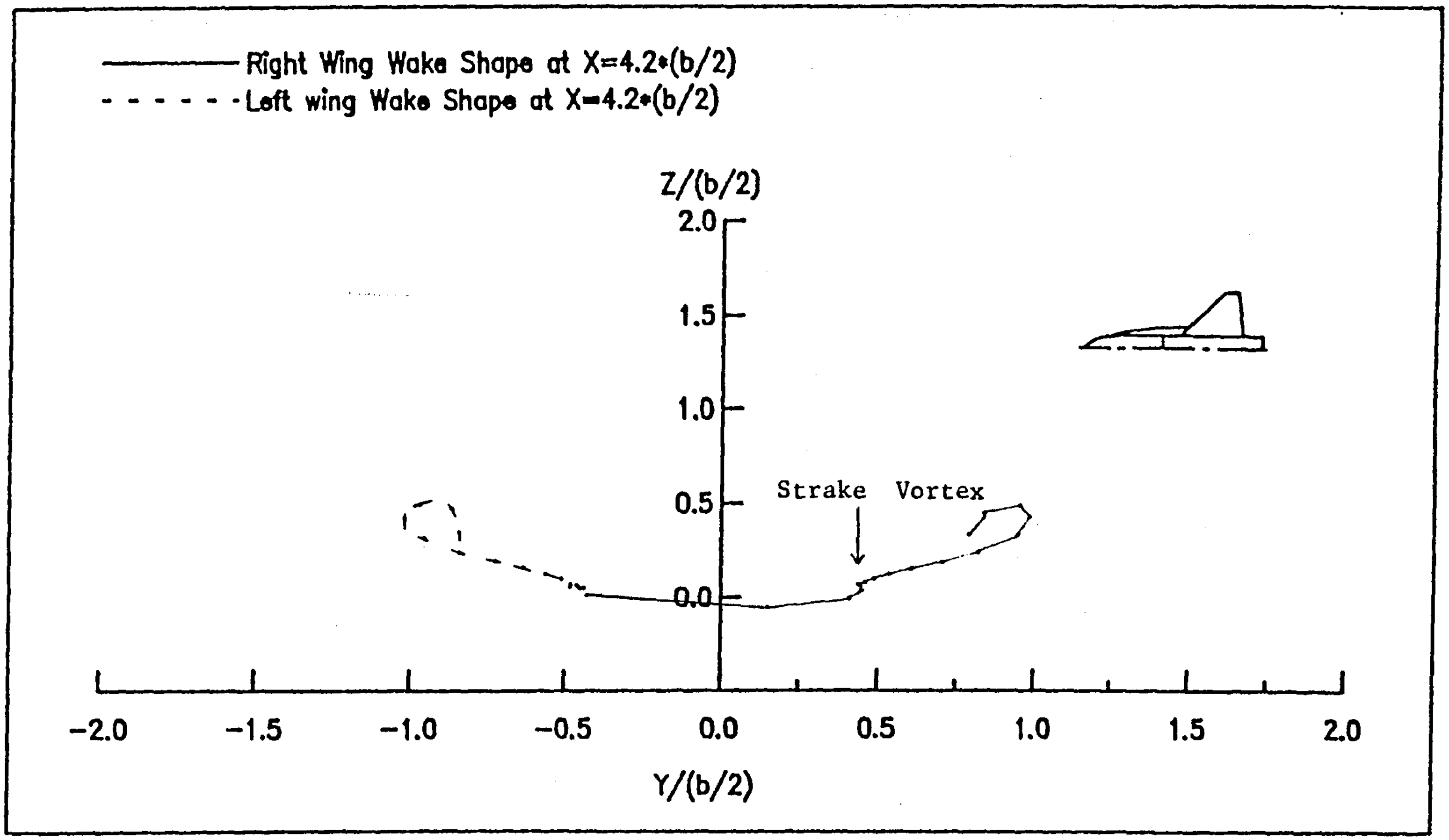

Fig. 11(e) Wake Shape of the Straked Wing-Body Configuration at Alpha = 29 and Beta = 17 deg.

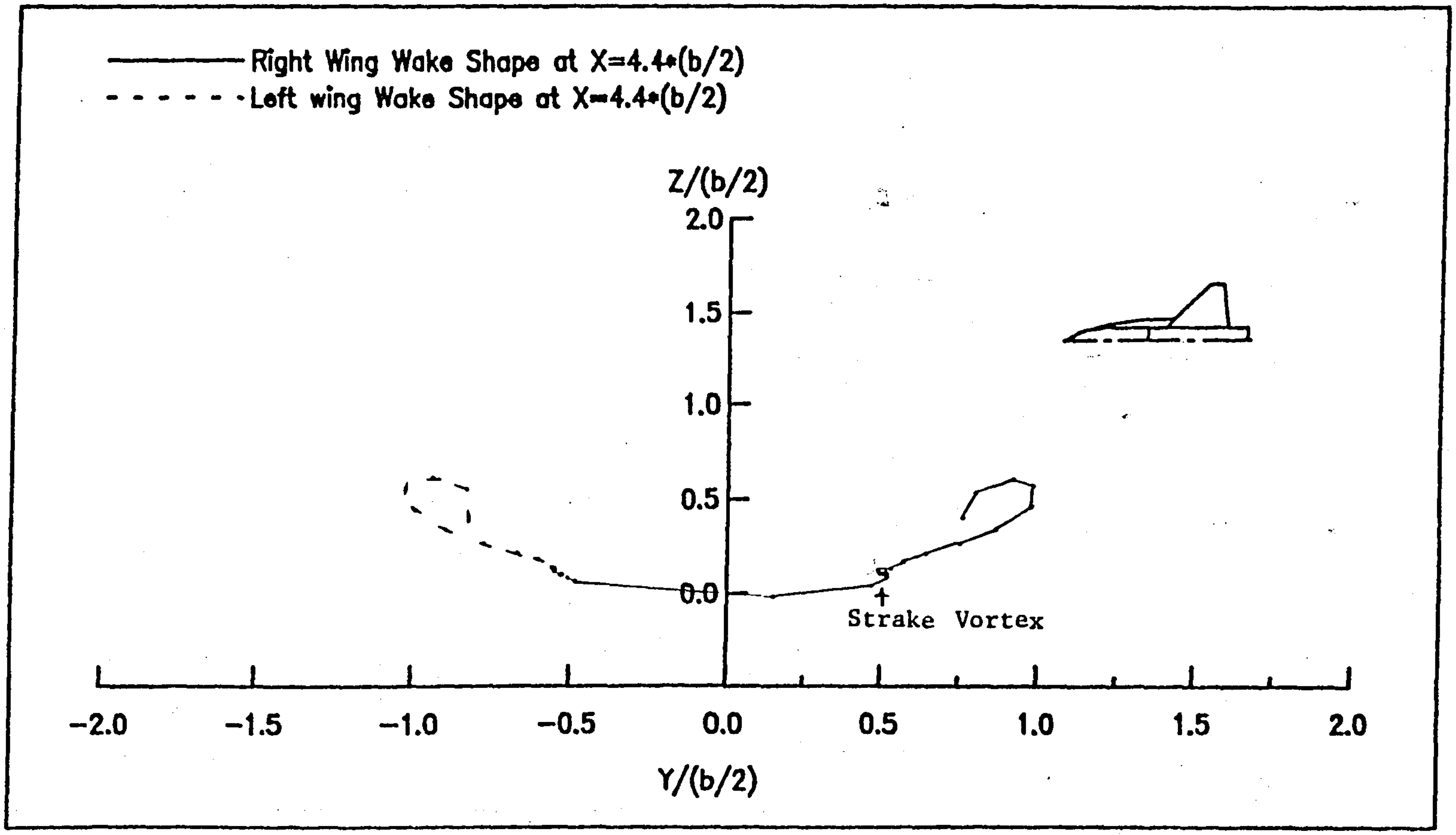

Fig. 11(f) Wake Shape of the Straked Wing-Body Configuration at Alpha = 29 and Beta = 17 deg.

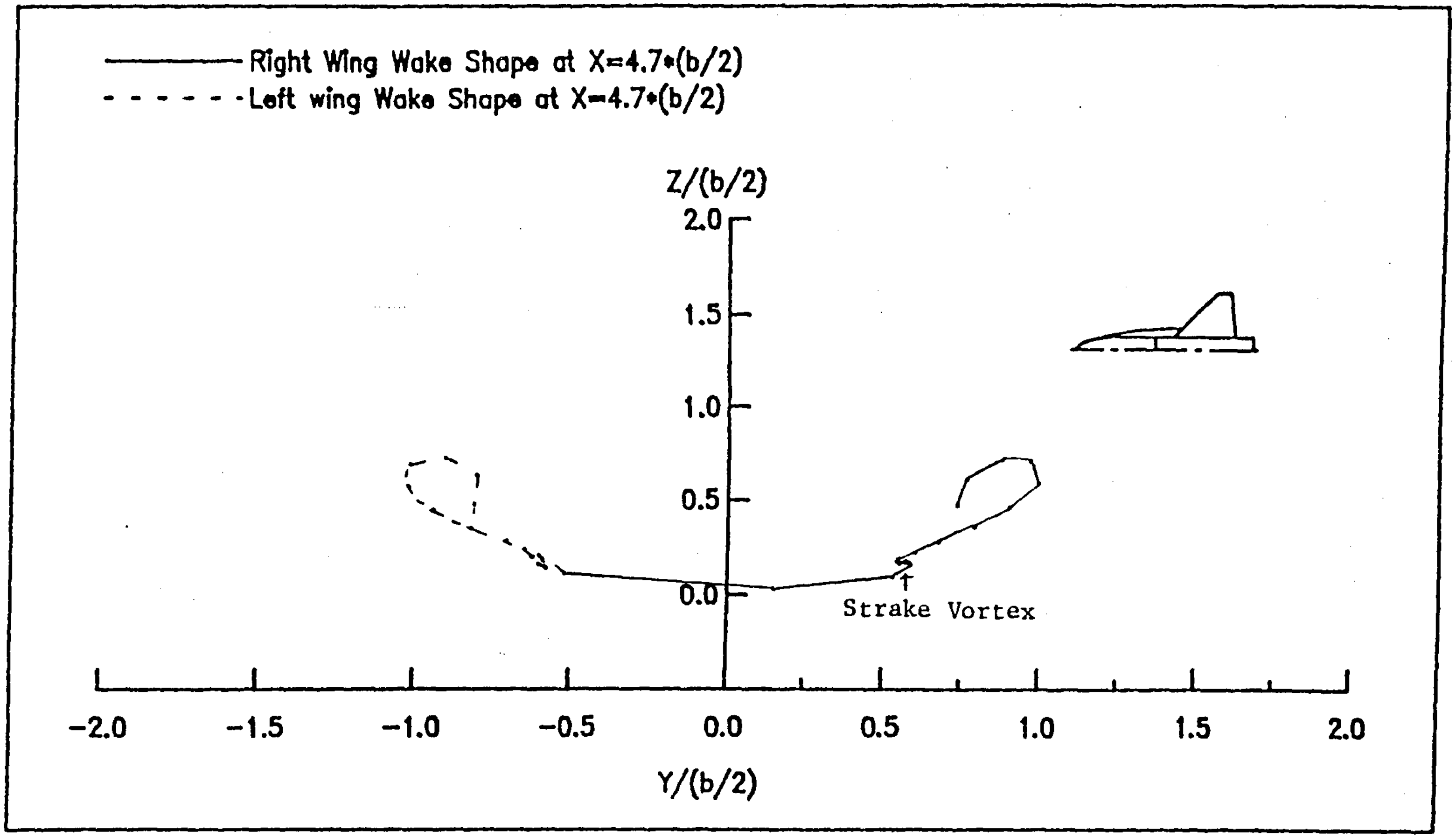

Fig. 11(g) Wake Shape of the Straked Wing-Body Configuration

at Alpha = 29 and Beta = 17 deg.

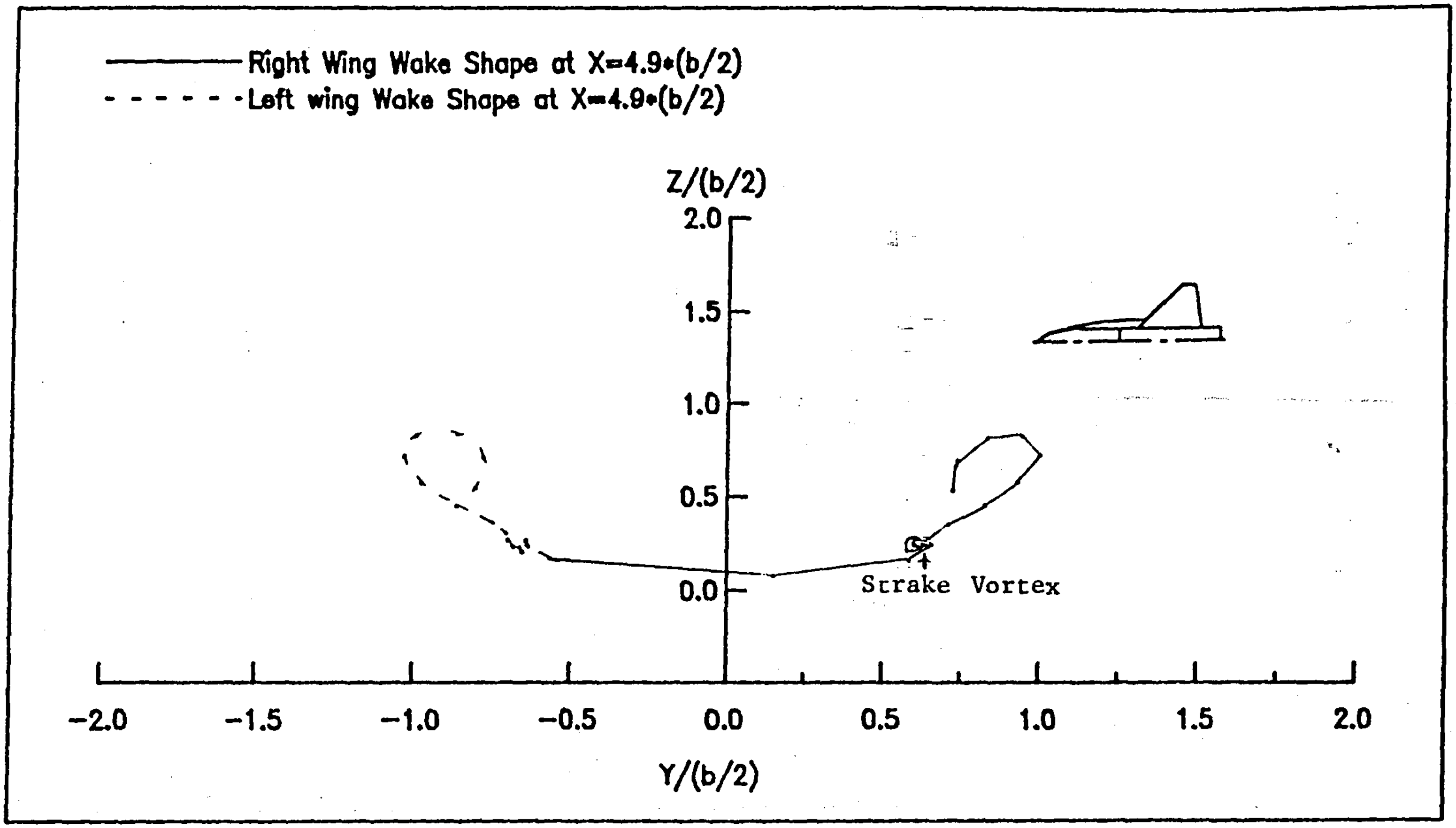

Fig. 11(h) Wake Shape of the Straked Wing-Body Configuration at Alpha = 29 and Beta = 17 deg.

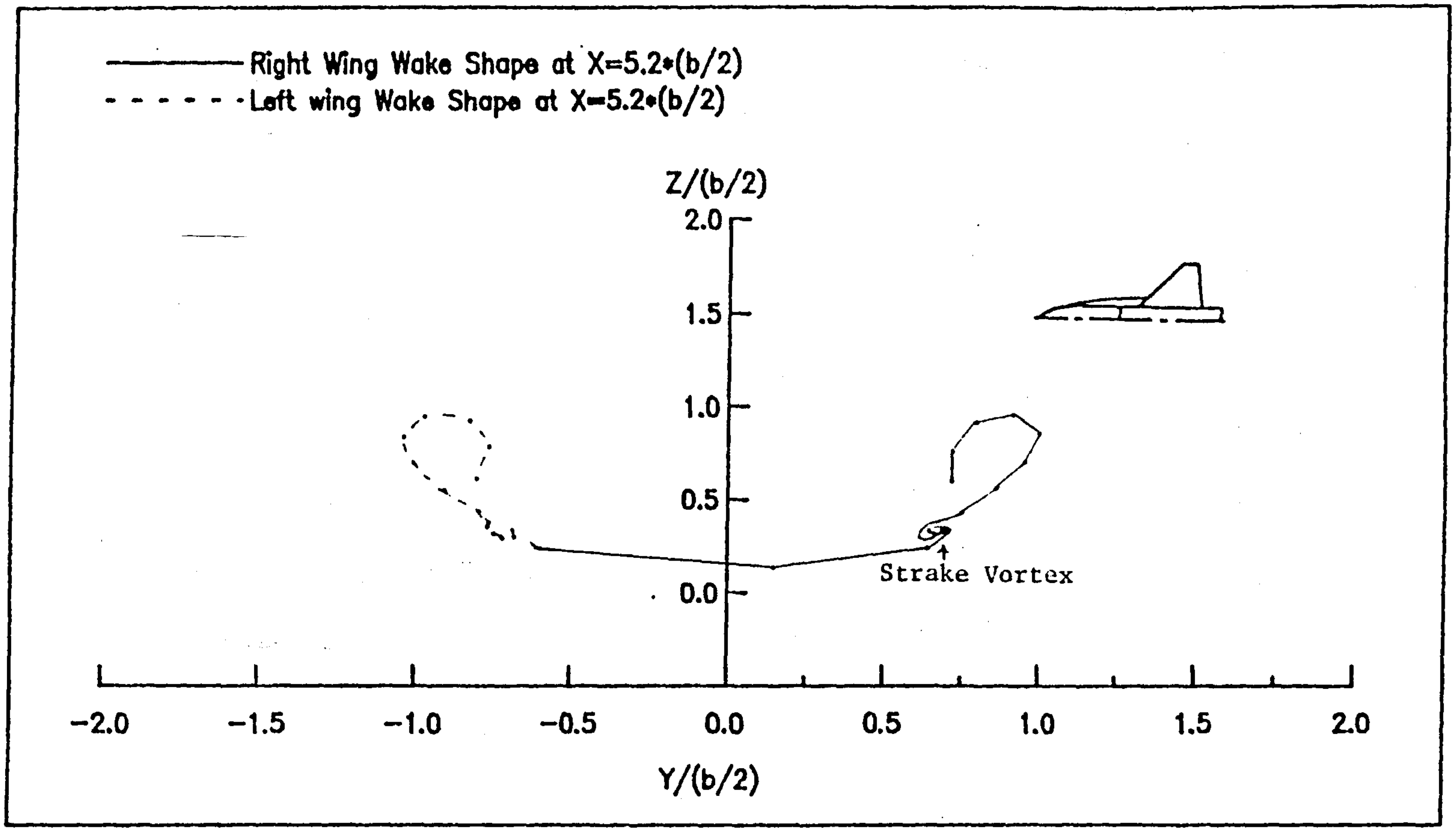

Fig. 11(i) Wake Shape of the Straked Wing-Body Configuration at Alpha = 29 and Beta = 17 deg.

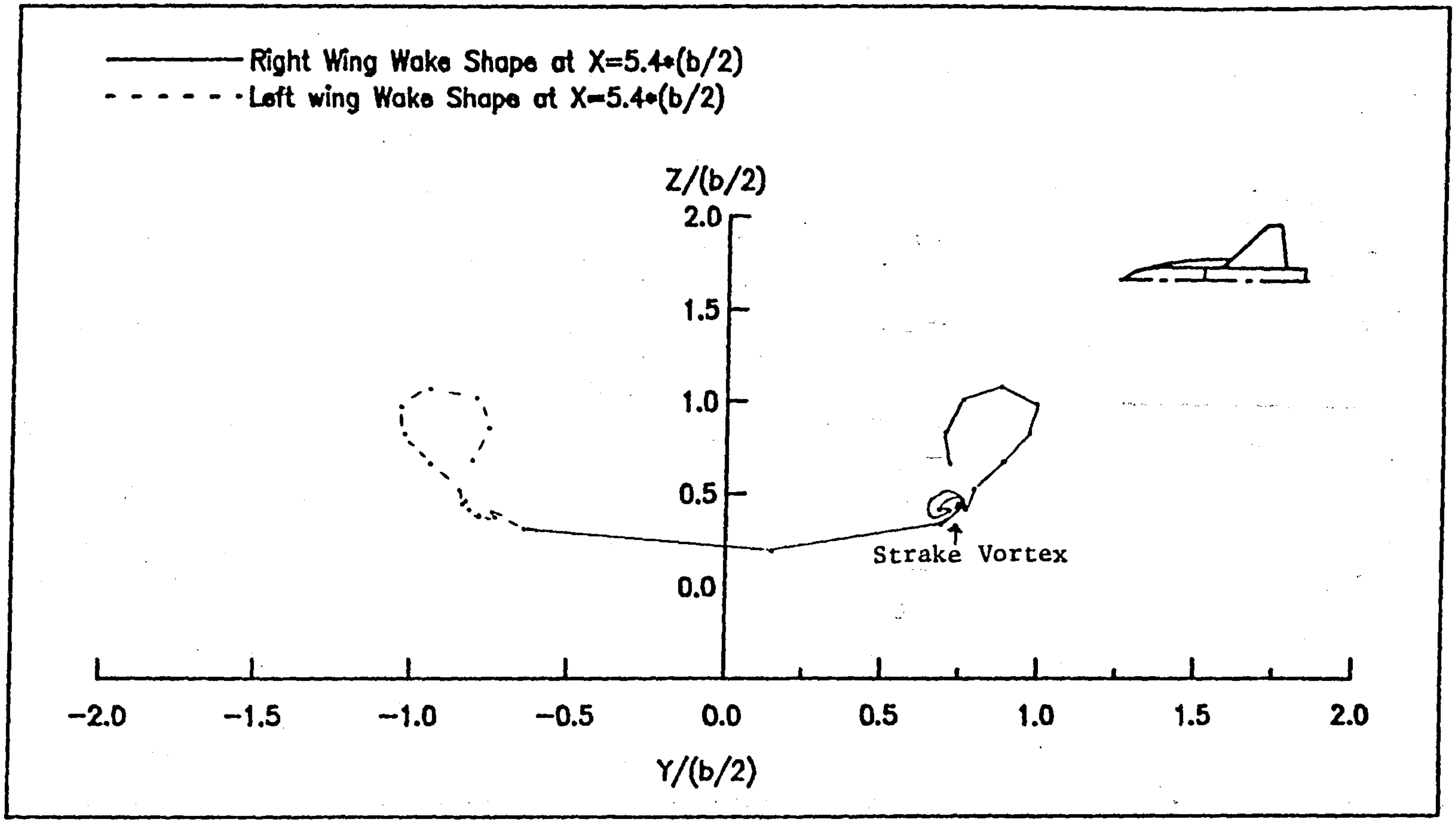

Fig. 11(j) Wake Shape of the Straked Wing-Body Configuration at Alpha = 29 and Beta = 17 deg.

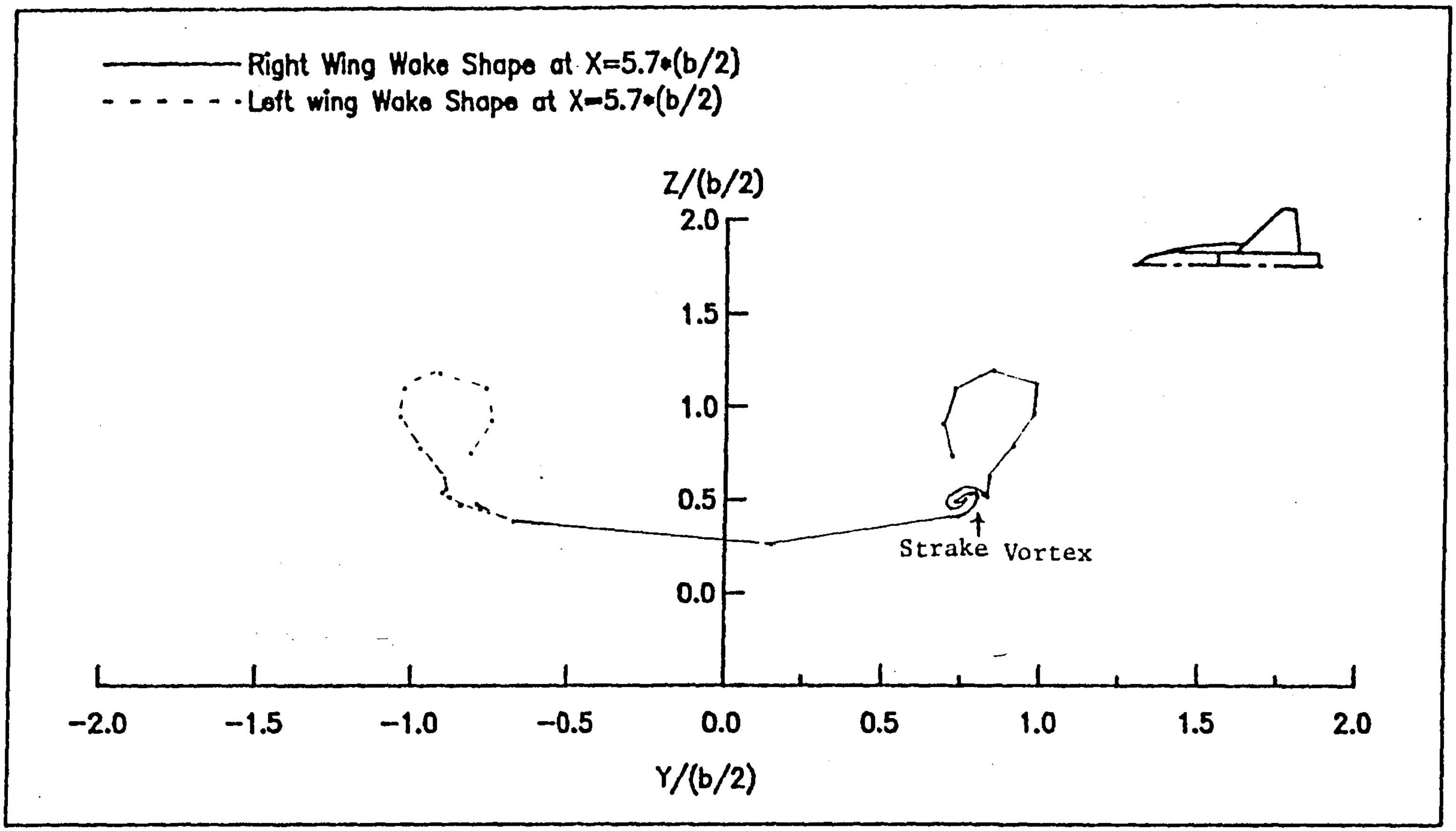

Fig. 11(k) Wake Shape of the Straked Wing-Body Configuration at Alpha = 29 and Beta = 17 deg.

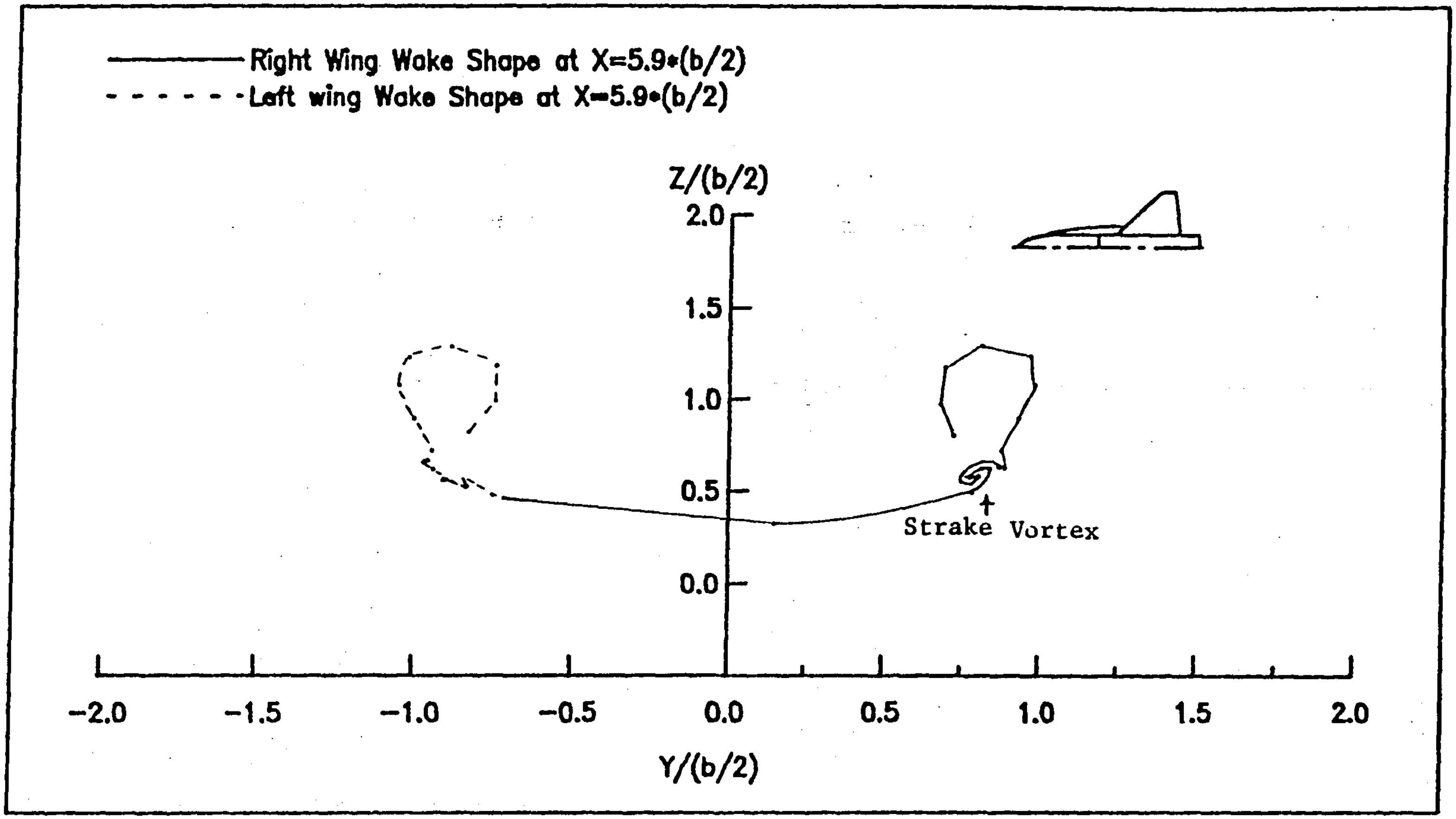

Fig. 11(1) Wake Shape of the Straked Wing-Body Configuration at Alpha = 29 and Beta = 17 deg.

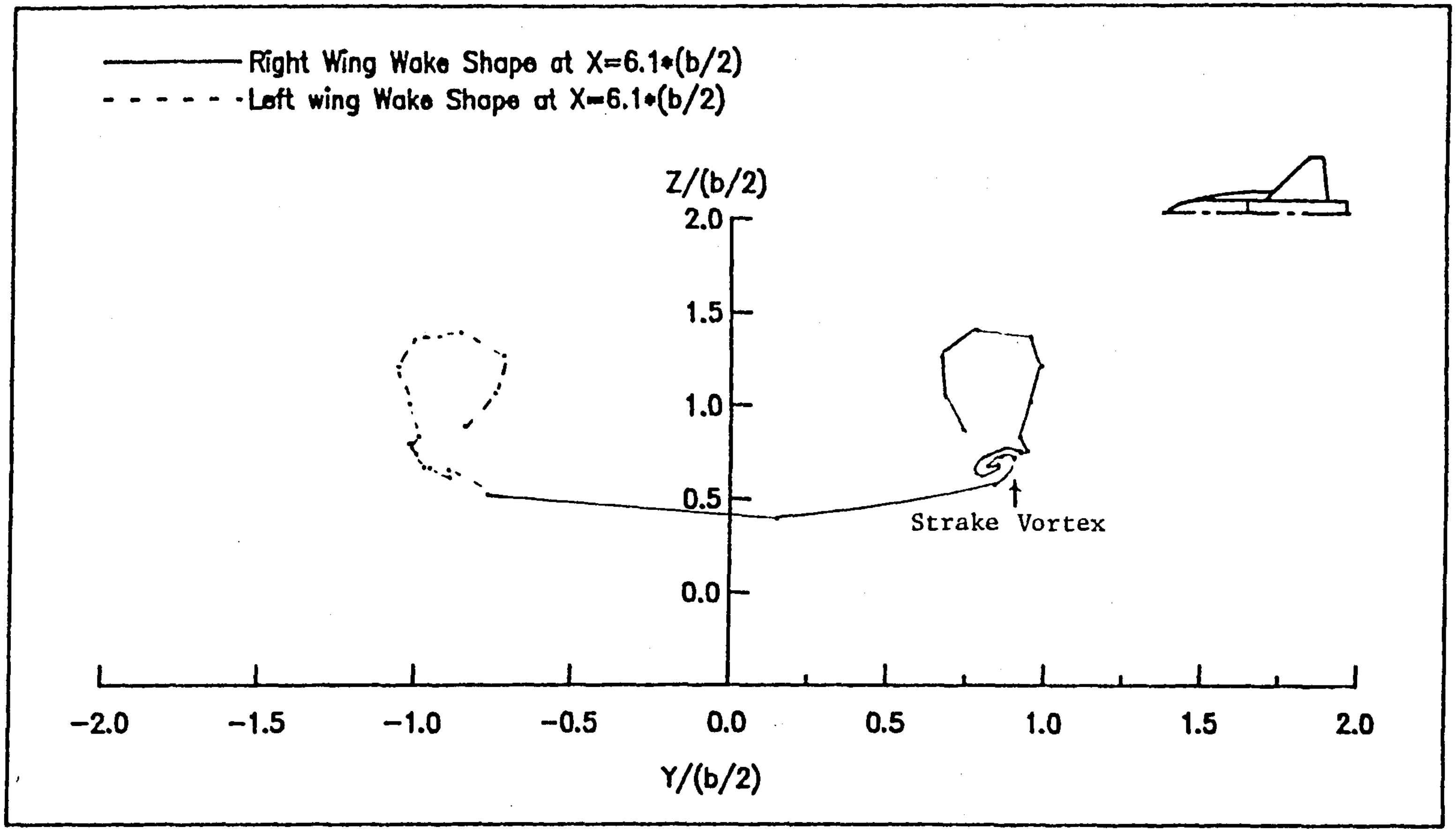

Fig. 11(m) Wake Shape of the Straked Wing-Body Configuration at Alpha = 29 and Beta = 17 deg.

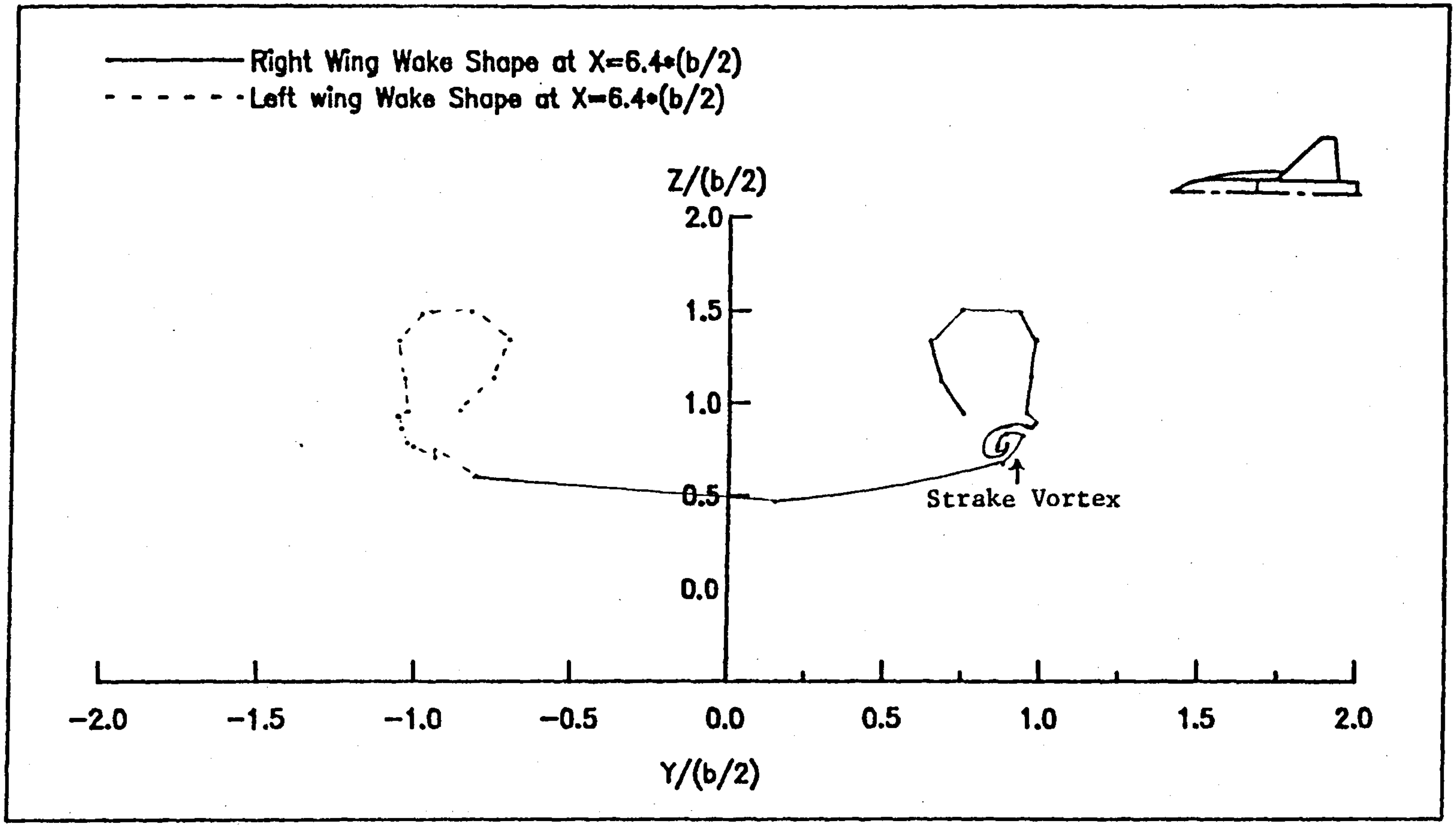

Fig. 11(n) Wake Shape of the Straked Wing-Body Configuration at Alpha = 29 and Beta = 17 deg.

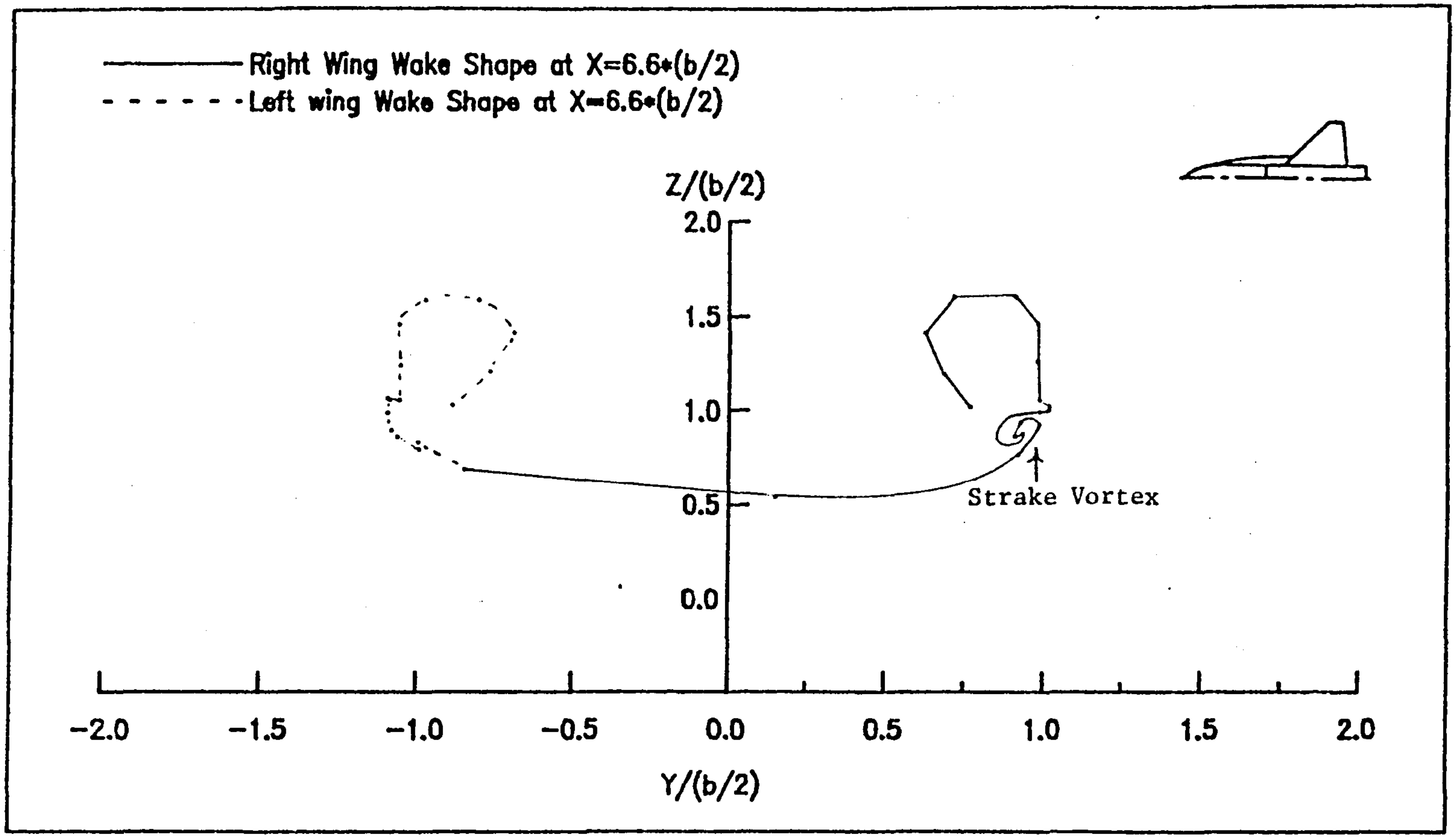

Fig. 11(o) Wake Shape of the Straked Wing-Body Configuration at Alpha = 29 and Beta = 17 deg.

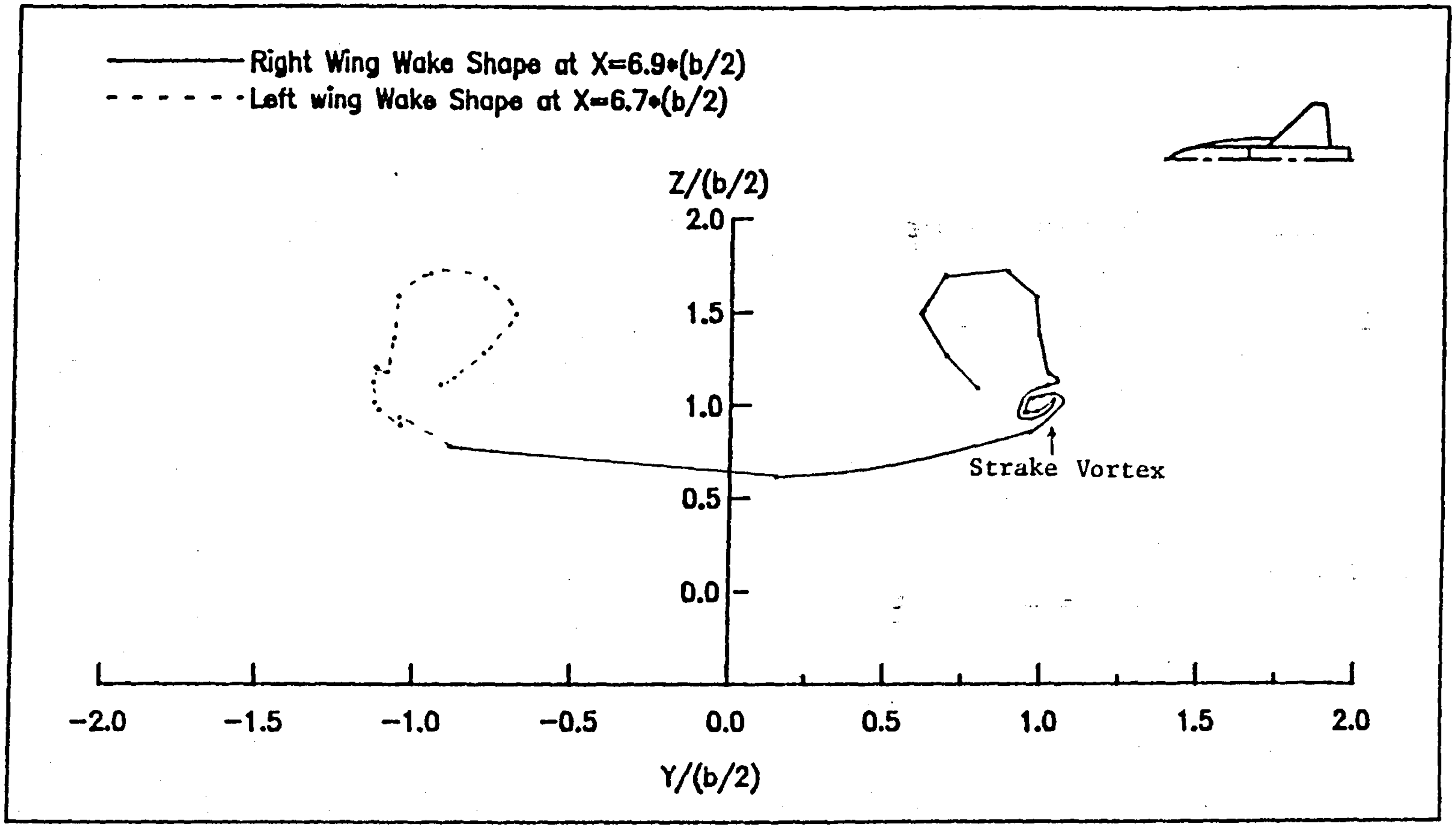

Fig. 11(p) Wake Shape of the Straked Wing-Body Configuration at Alpha = 29 and Beta = 17 deg.

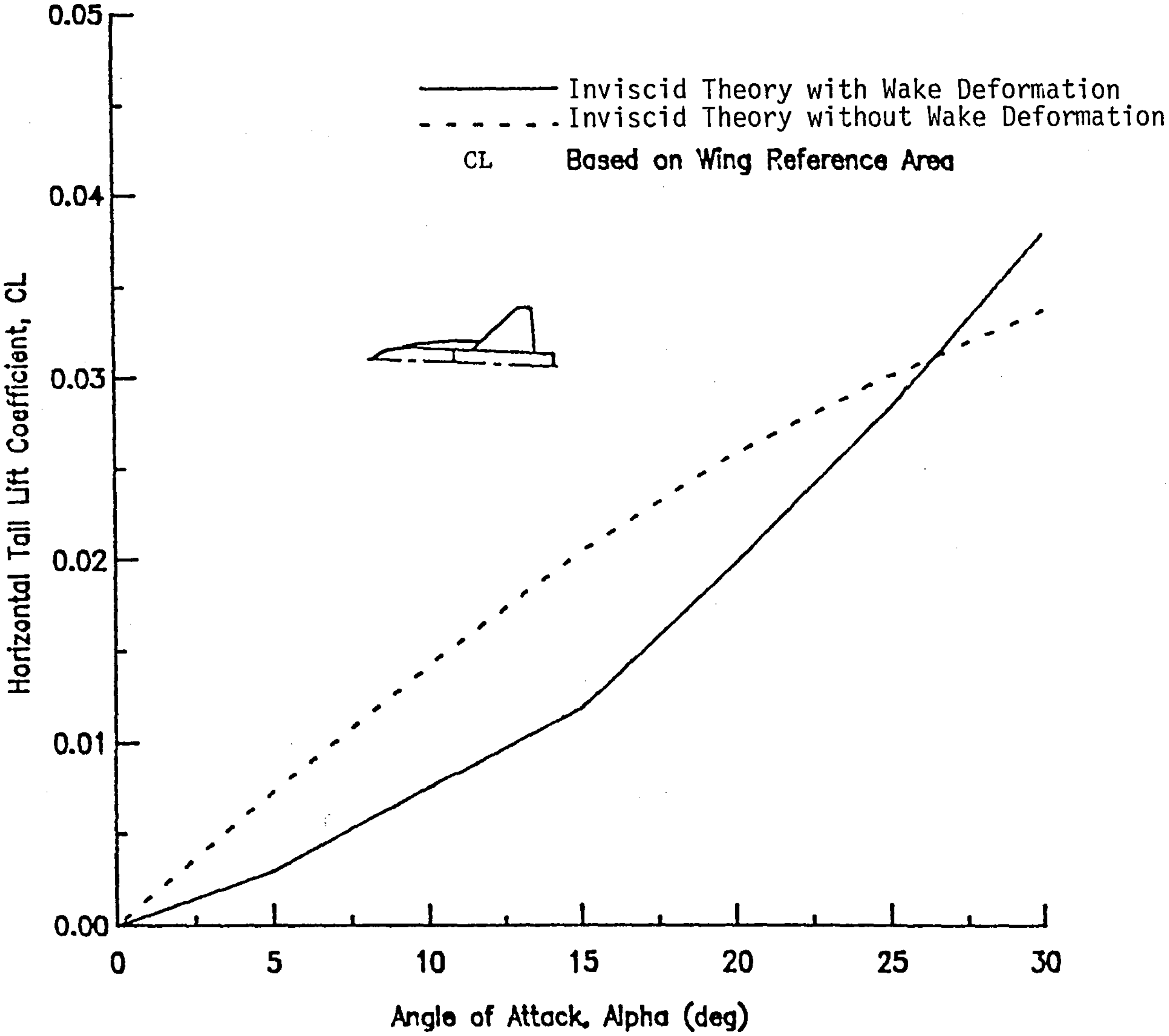

Fig. 12(a) Static Longitudinal Characteristics of the Straked Wing-Body Configuration

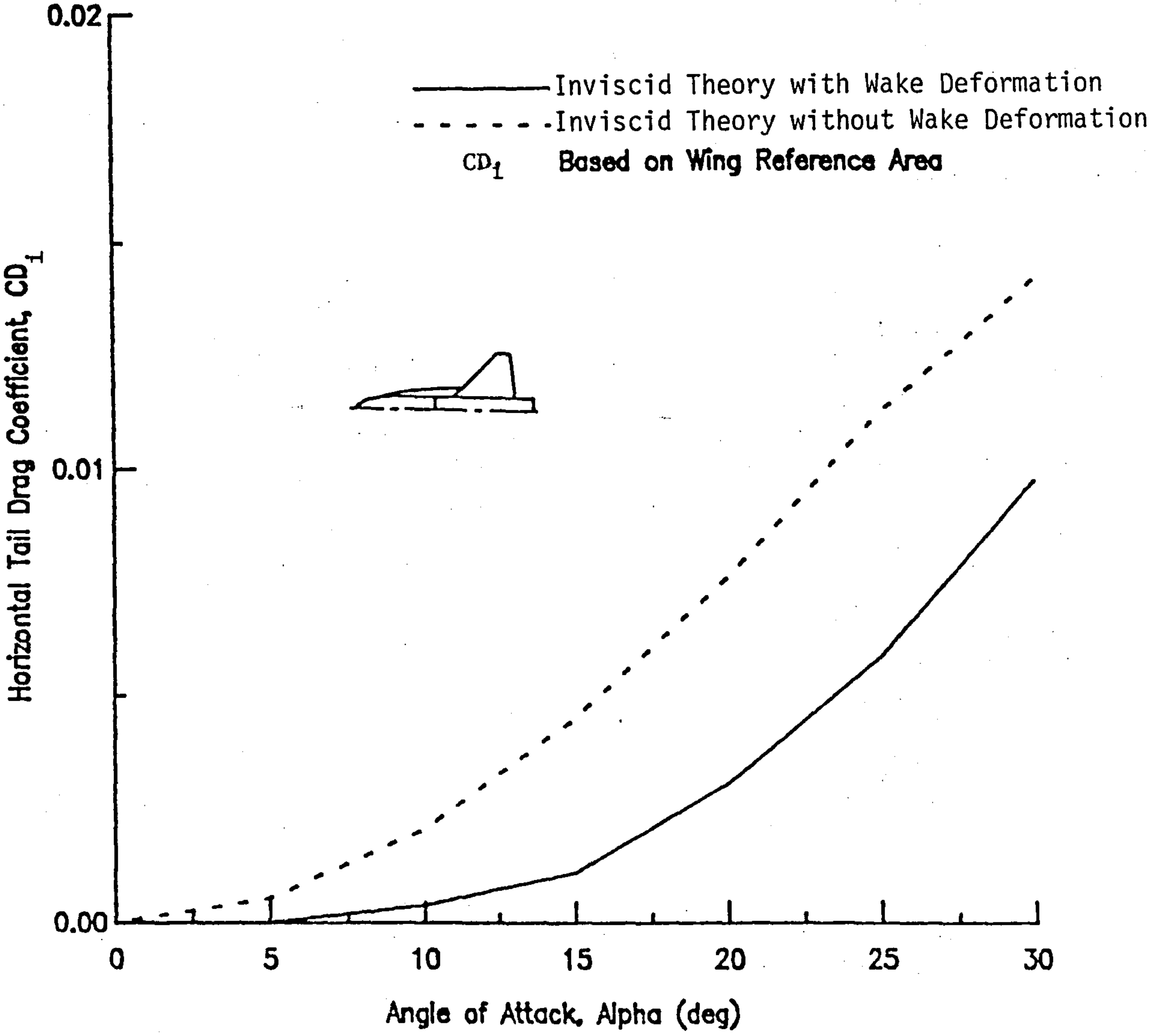

Fig. 12(b) Static Longitudinal Characteristics of the

Straked Wing-Body Configuration

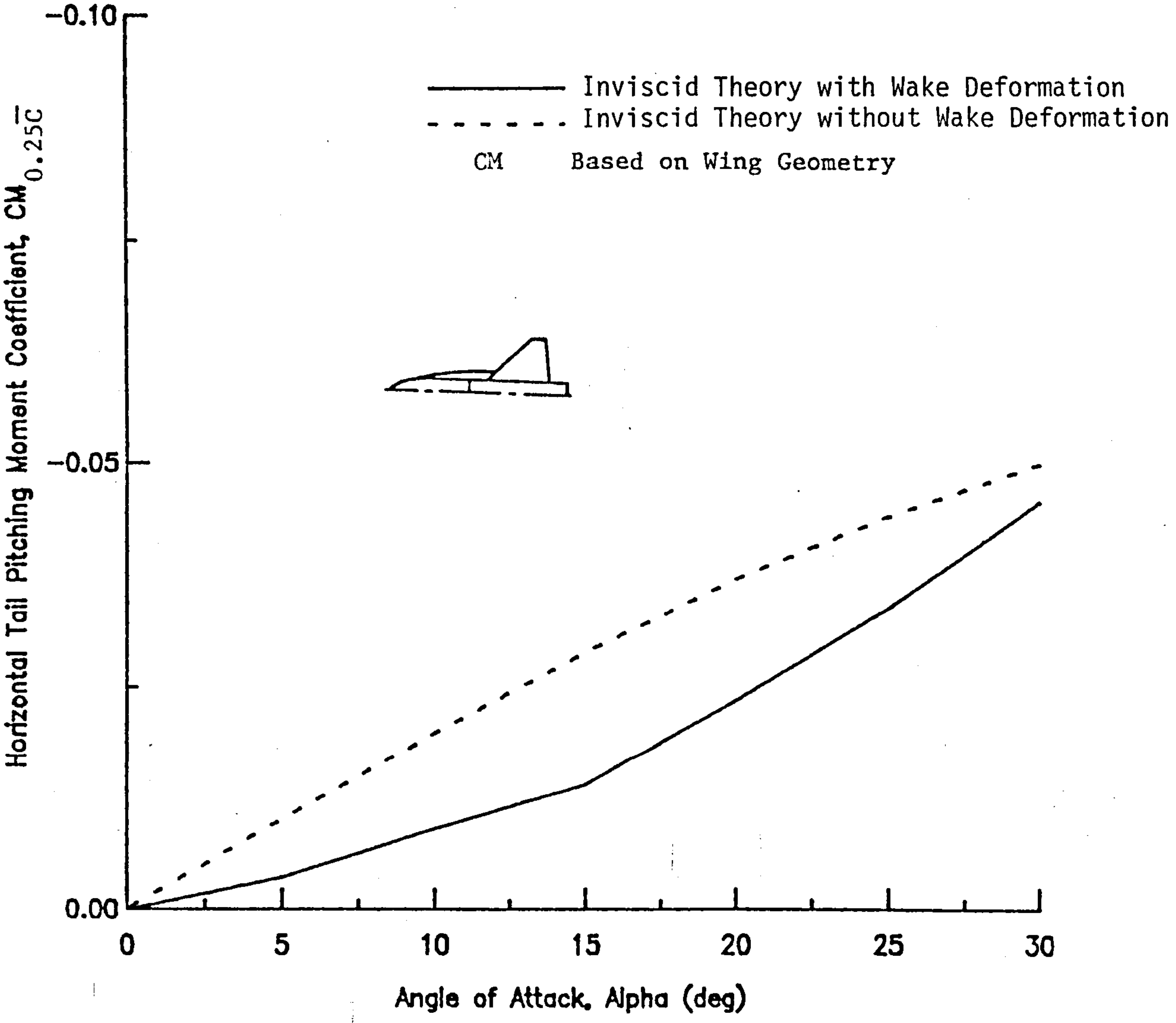

Fig. 12(c) Static Longitudinal Characteristics of the Straked Wing-Body Configuration

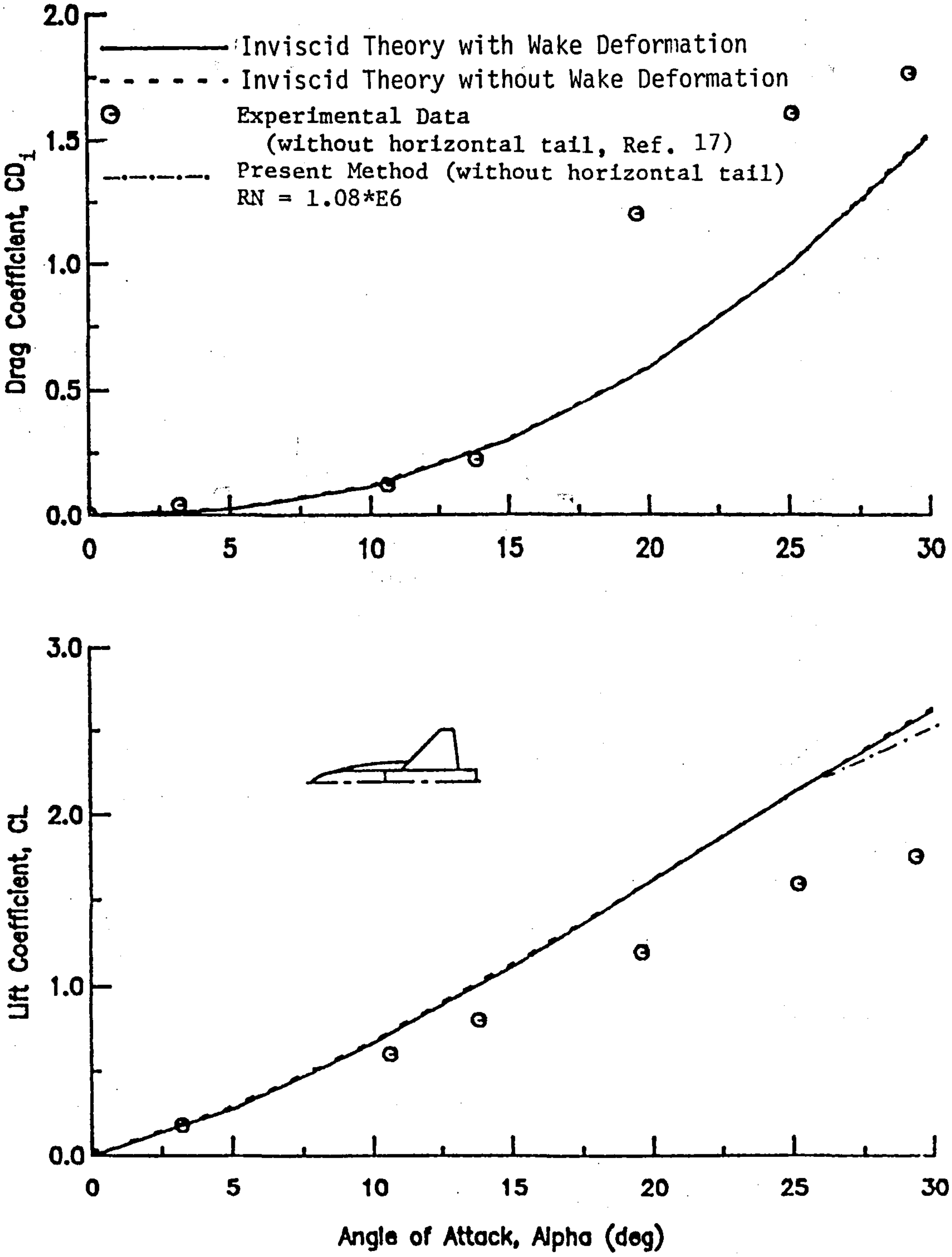

Fig. 13(a) Static Longitudinal Characteristics of the Straked Wing-Body Configuration at Beta = 0.0 deg.

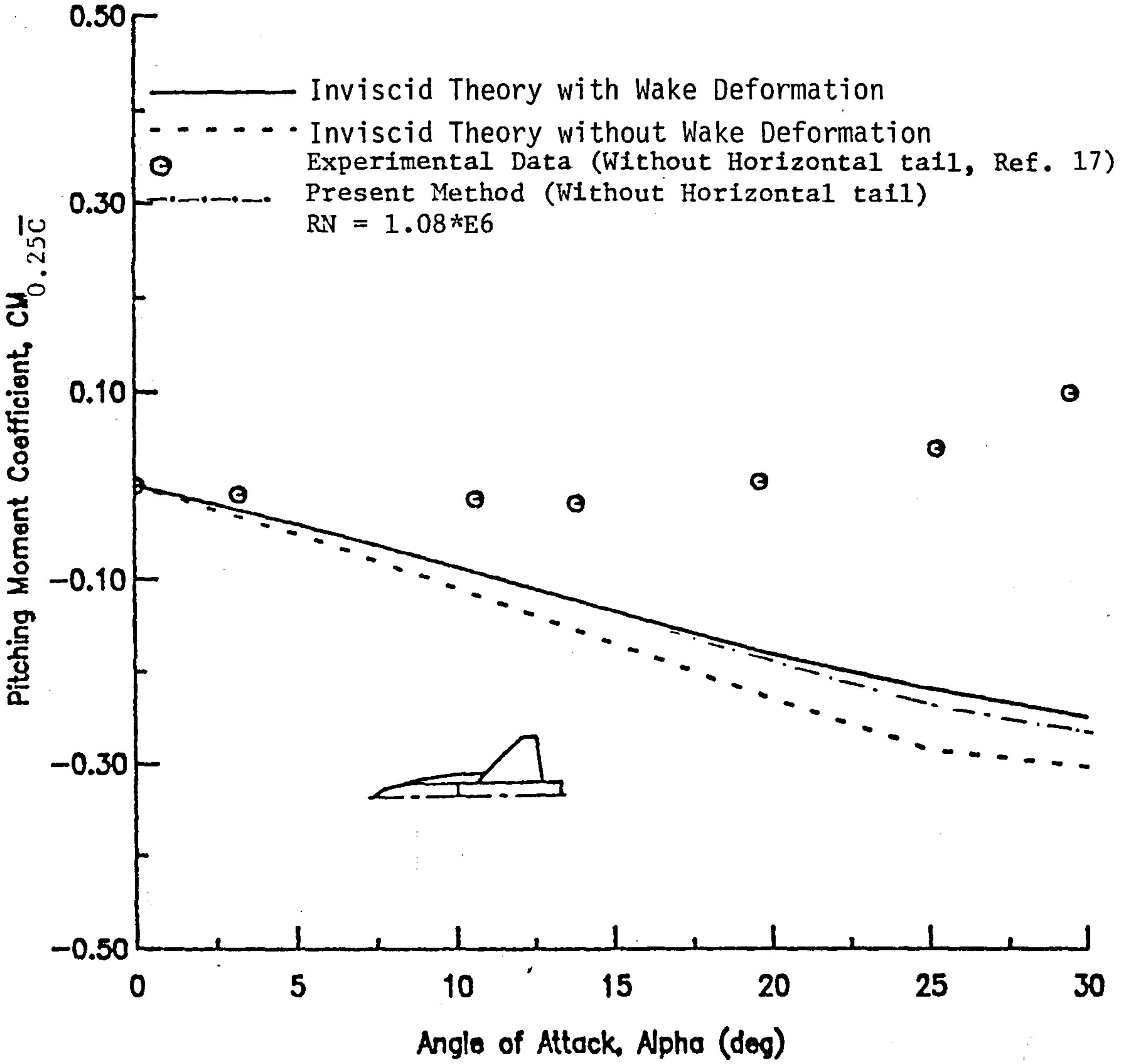

Fig. 13(b) Static Longitudinal Characteristics of the Straked Wing-Body Configuration (Cont)

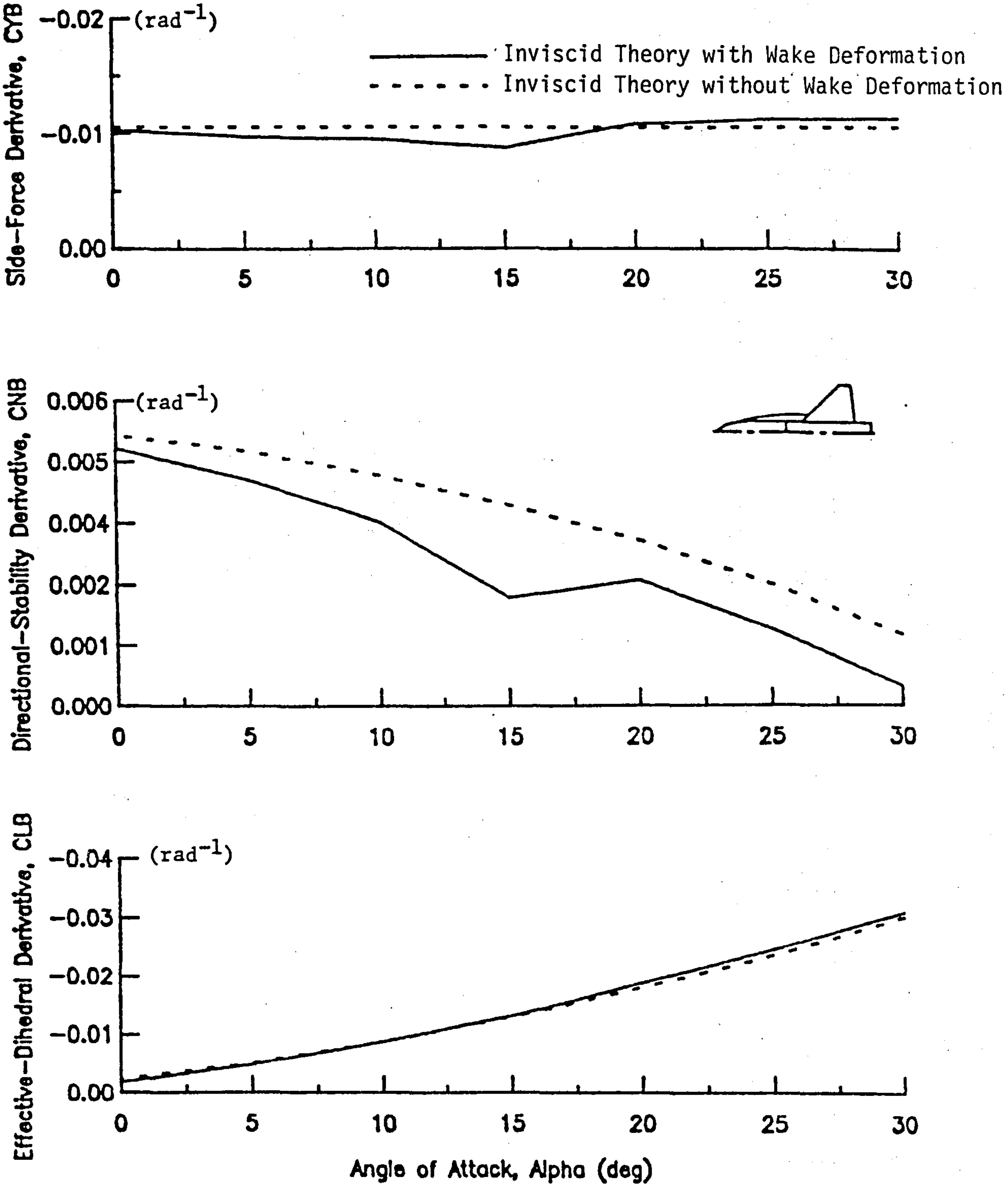

Fig. 14 Static Lateral-Directional Stability Derivatives of the Straked Wing-Body Configuration at Beta = 17 deg.

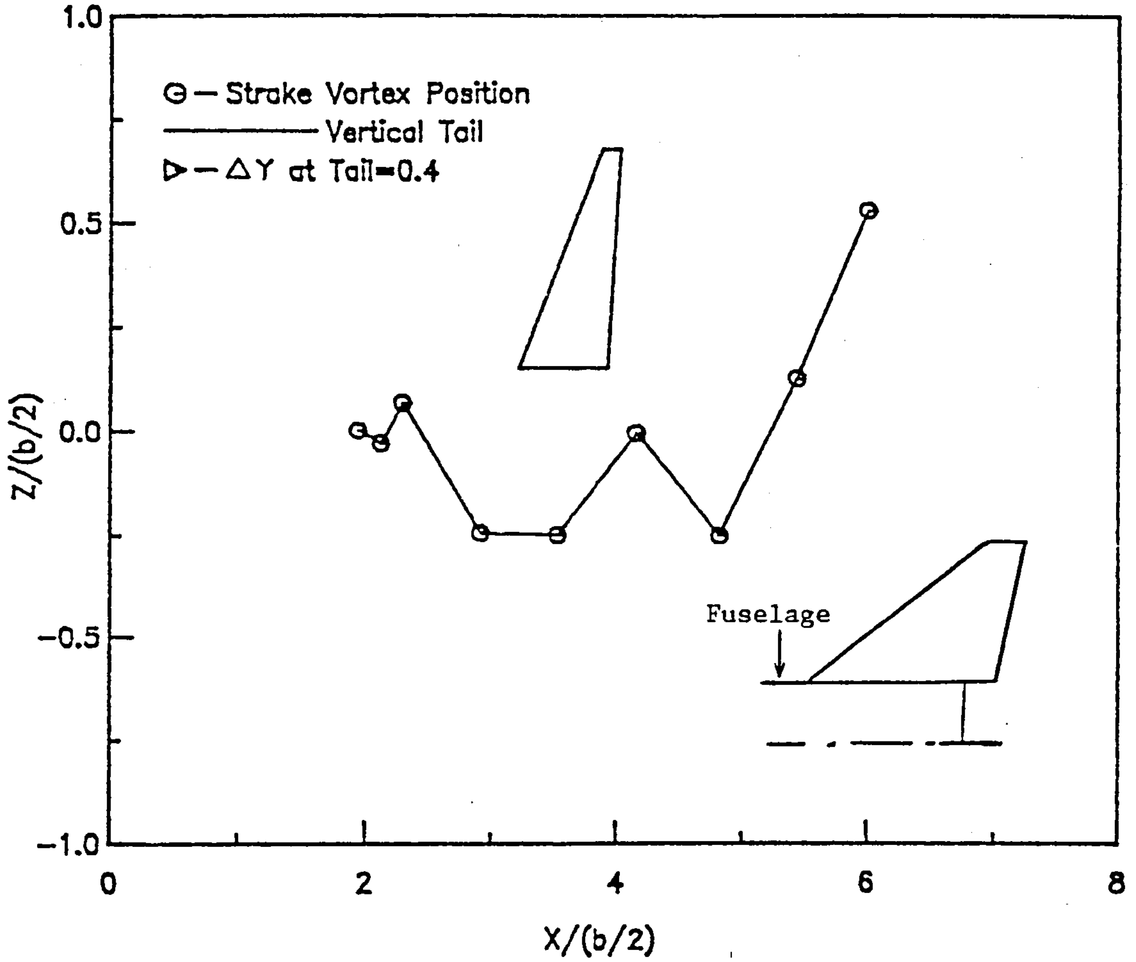

Fig. 15 Effect of Strake Vortex on Vertical Tail for Straked Wing-Body Configuration at Alpha = 29 deg.

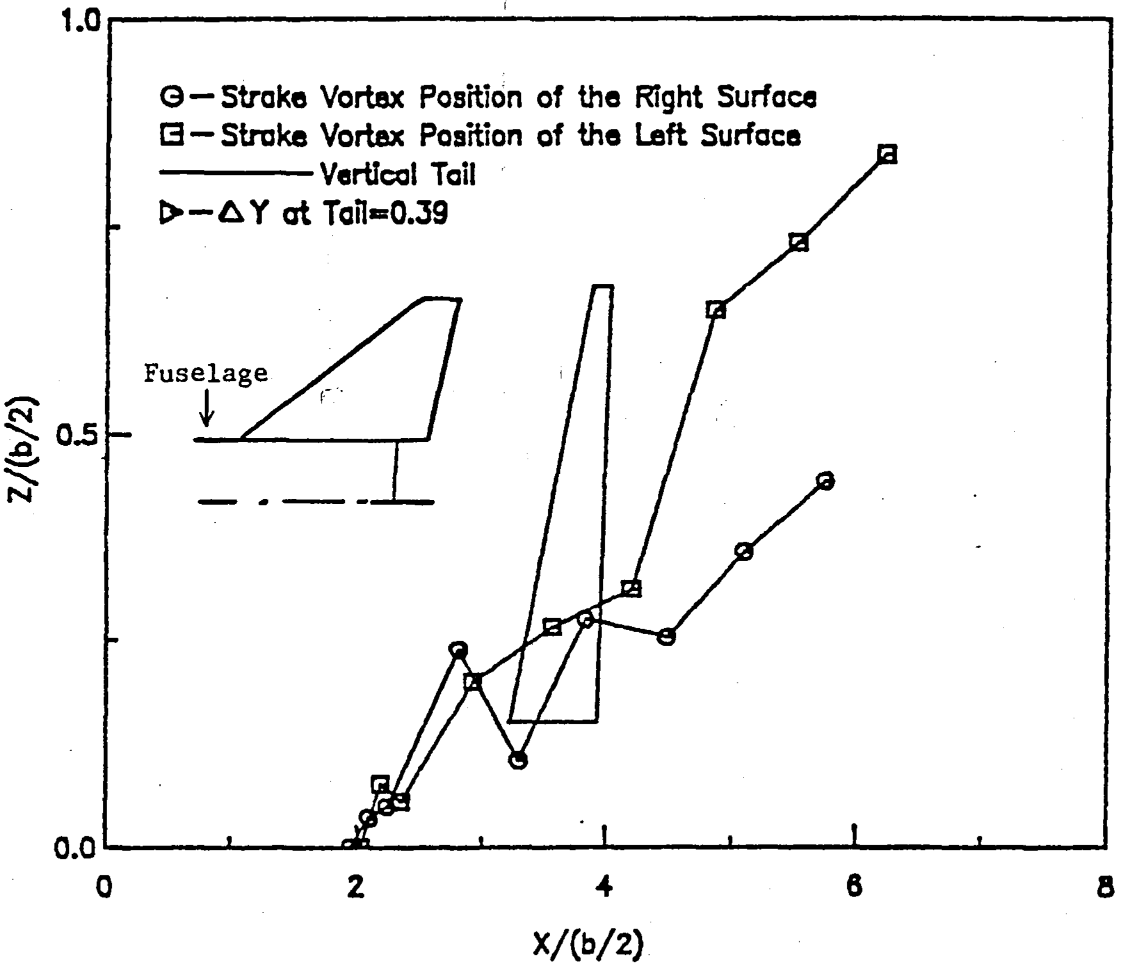

Fig. 16 Effect of Strake Vortex on Vertical Tail for Straked Wing-Body Configuration at Alpha = 29 and Beta = 17 deg.

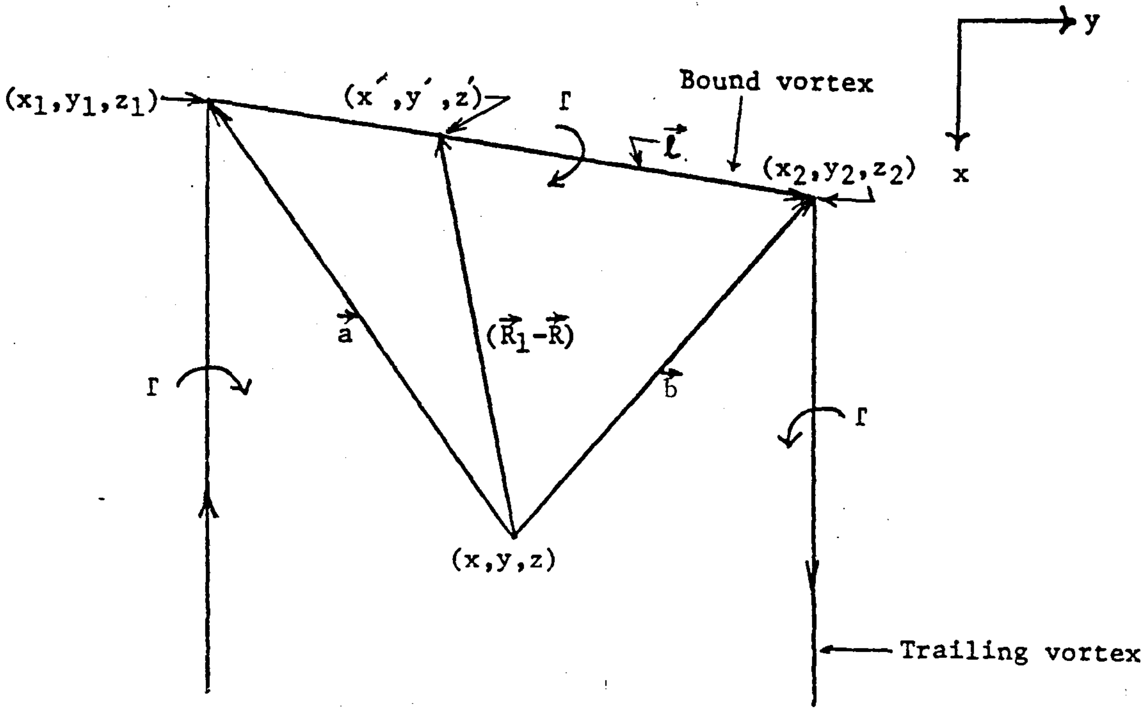

Geometry for a Horseshoe Vortex

Fig. 17

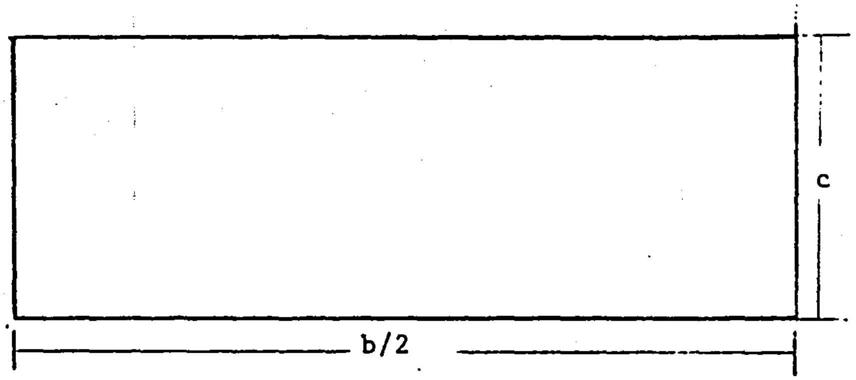

Span (b) = 8

Chord Length (c) = 1

Lift Coefficient = 1

Rectangular Wing Geometry and Aerodynamic Configuration

Fig. 18

Strake-Wing Geometry (Taken from Ref. 17)

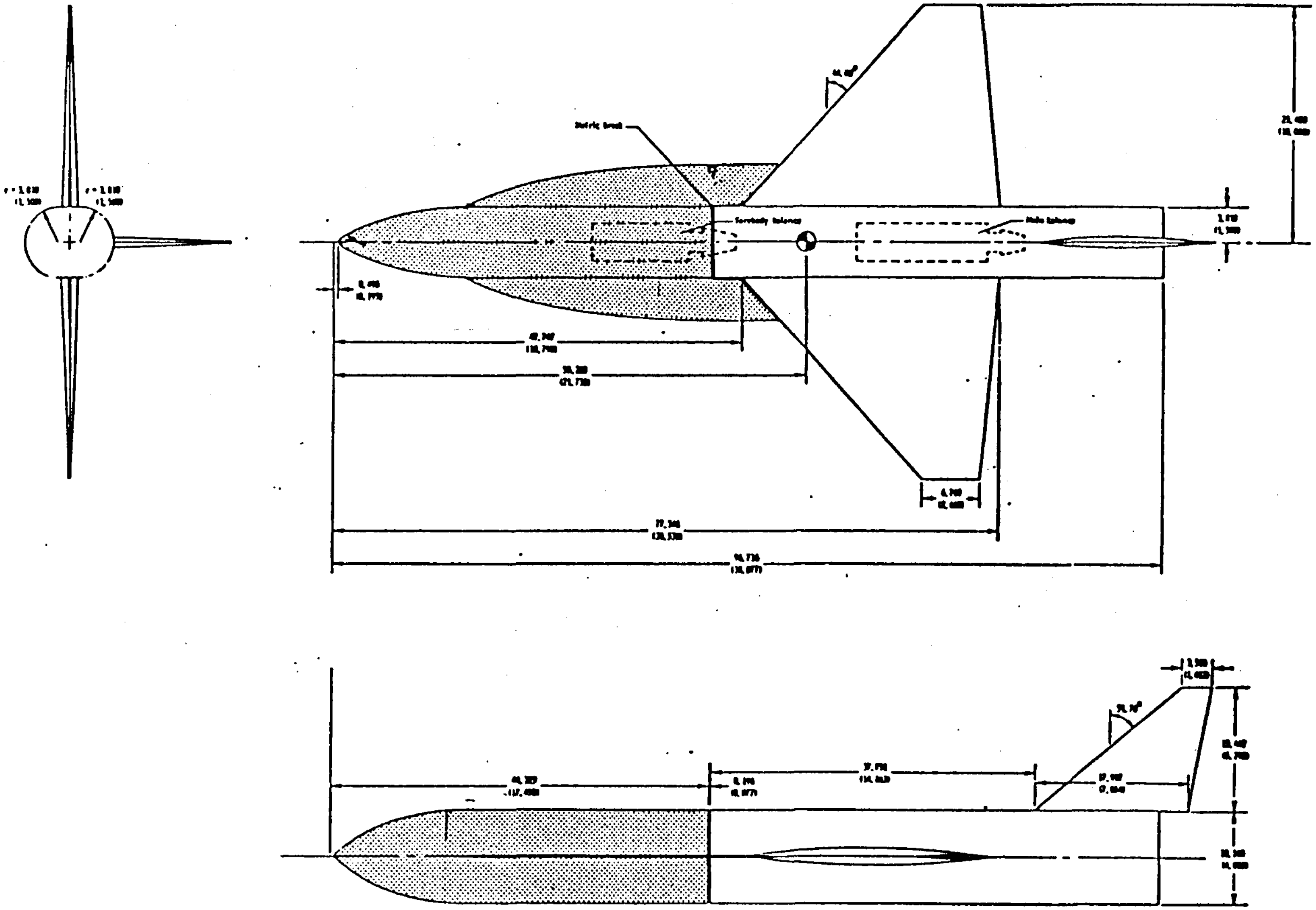

Figure 19 Three-view drawing of typical wind-tunnel model. Shaded area is associated with forebody balance; linear dimensions are in centimeters (inches).

Standard Bibliographic Page

1. Report No. NASA CR-178118	2. Government Accession No.	3. Recipient's Catalog No.
4. Title and Subtitle Wake Shape and Its Effects on Aerodynamic Characteristics		5. Report Date July 1986
		6. Performing Organization Code
7. Author(s) Homayoun Emdad and C. Edward Lan		8. Performing Organization Report No. CRINC-FRL-516-3
9. Performing Organization Name and Address Flight Research Laboratory The University of Kansas Center for Research, Inc. Lawrence, KS 66045		10. Work Unit No.
		11. Contract or Grant No. NAG1-134
12. Sponsoring Agency Name and Address National Aeronautics and Space Administration Washington, DC 20546		13. Type of Report and Period Covered Contractor Report
		14. Sponsoring Agency Code 505-43-13-01

15. Supplementary Notes

Langley Technical Monitor: Jay M. Brandon

16. Abstract

In this study, the wake shape under symmetrical flight conditions and its effects on aerodynamic characteristics are examined. In addition, the effect of wake shape in sideslip and discrete vortices such as strake or forebody vortex on lateral characteristics is presented. The present numerical method for airplane configurations, which is based on discretization of the vortex sheet into vortex segments, verified the symmetrical and asymmetrical roll-up process of the trailing vortices. Also the effect of wing wake on tail planes is calculated. It is concluded that at high lift the assumption of flap wake for longitudinal and lateral-directional characteristics should be reexamined.

17. Key Words (Suggested by Authors(s)) Vortex Flow Wake Deformation Lateral-Directional Stability Derivatives	18. Distribution Statement Unclassified - Unlimited Subject Category 02

19. Security Classif.(of this report) Unclassified	20. Security Classif.(of this page) Unclassified	21. No. of Pages 115	22. Price A06

For sale by the National Technical Information Service, Springfield, Virginia 22161

NASA Langley Form 63 (June 1985)

End of Document